Resonance-enhanced charge delocalization in carbazole-oligoyne-oxadiazole conjugates

Anna Zieleniewska,[a‡] Xiaotao Zhao,[b‡] Stefan Bauroth,[a] Changsheng Wang,[b] Andrei S. Batsanov,[b] Christina Krick Calderon,[a] Axel Kahnt,[c] Timothy Clark,[a] Martin R. Bryce,*[b] Dirk M. Guldi*[a]

a Department of Chemistry and Pharmacy & Interdisciplinary Center for Molecular Materials, Friedrich-Alexander-Universität Erlangen-Nürnberg, Egerlandstr. 3, 91058 Erlangen, Germany.

b Department of Chemistry, Durham University, Durham DH1 3LE, United Kingdom.

c Leibniz Institute of Surface Engineering (IOM), Permoserstr. 15, D-04303 Leipzig, Germany.

ABSTRACT: There are notably few literature reports of electron donor-acceptor oligoynes although they offer unique opportunities for studying charge transport through 'all-carbon' molecular bridges. In this context, the current study focuses on a series of carbazole–(C≡C)$_n$-2,5-diphenyl-1,3,4-oxadiazoles (n = 1-4) as conjugated π-systems, in general, and explores their photophysical properties, in particular. Contrary to the behavior of typical electron donor-acceptor systems, for these oligoynes the rates of charge recombination after photoexcitation increase with increasing electron donor-acceptor distance. To elucidate this unusual performance, detailed photophysical and time-dependent density functional theory investigations were conducted. Significant delocalization of the electron density along the bridge indicates that the bridging states come into resonance with either the electron donor or acceptor, thereby accelerating the charge transfer. Moreover, the calculated bond lengths reveal a reduction in bond length alternation upon photoexcitation, indicating significant cumulenic character of the bridge in the excited state. In short, strong vibronic coupling between the electron-donating *N*-arylcarbazoles and the electron-accepting 1,3,4-oxadiazoles accelerates the charge recombination as the oligoyne becomes longer.

Introduction

Light-induced charge generation and charge transport in molecular materials, in general, and in covalent electron donor-acceptor conjugates, in particular, is of broad interest. For example, they are relevant to the development of novel molecular systems for practical applications in either information storage or organic semiconductor devices, including photovoltaic cells, organic light emitting diodes, field-effect transistors, etc.[1–8] The impact of these studies is also of a fundamental nature; they help provide a more comprehensive understanding of the multifaceted processes associated with photochemical charge transfer, charge separation, charge shift, charge propagation, charge recombination, etc. occurring in photosynthetic reaction ensembles, redox proteins, and nucleic acids.[9–12] End-capping the bridges with various organic or organometallic donors (Ds) and acceptors (As) makes control over the extent of charge transfer through π-conjugated bridges across relatively large distances possible.[13–15] Intramolecular coupling decays exponentially with increasing distance between the Ds and As according to the electron-transfer rate constant k_{ET}.[16] Consequently, the rates of charge separation and recombination follow an exponential expression: $k_{\mathrm{ET}} = k_0 e^{-\beta R_{\mathrm{DA}}}$. Here, k_0 is a kinetic pre-factor, R_{DA} is the distance between the Ds and As, and β is the attenuation factor. The latter reflects the intrinsic electronic properties of the bridge in terms of charge transport. It is generally the case that efficient and rapid charge transfer (i.e., a low β value) requires a high degree of conjugation across the entire D–B–A system, with efficient electronic coupling of the bridge (B) to both the Ds and As.[17] Notably, with longer bridges a mechanistic change in the charge transport is seen from, for example, charge superexchange, which is operative at shorter distances, to charge hopping, which dominates at larger distances.

Many different molecular bridges have been used to link Ds and As. Typical bridges in D–B–A systems comprise oligo-phenylenevinylenes (oPVs),[18–22] oligo-phenyleneethynylenes (oPEs),[23–29] oligo-fluorenes (oFls),[30–33] oligo-vinylfluorenes,[34] ladder-OFls,[35] oligo-thiophenes,[36–38] oligo-vinylthiophenes,[39] oligo(ethynylene-10,20-porphyrindiyl-ethynylene)s,[40] oligo-phenylenes,[41–45] and others.[3,46] It is noteworthy that oligoynes [(C≡C–)$_n$] have only been partially studied as bridge units in this context.[47–50] The majority of published studies on electron donor-acceptor oligoynes treats of diynes and triynes.[51–53] In 1997, Biswas *et al.* reported one of the first studies of asymmetrically substituted acetynyl and butadinyl bridges.[54] Some of their initial observations are also reflected in the current work. A different example of push-pull oligoynes comes from the Diederich group.[55] Longer oligoyne bridges formed the focal point of their investigations but the main focus was on nonlinear optical properties.

A deeper understanding of charge transfer processes across oligoynes is crucial as they are of particular interest in molecular electronics.[56–60] Oligoynes represent linear chains of *sp*-hybridized carbon atoms that constitute the ultimate one-dimensional molecular wire.[61–67] In comparison to oligoenes, oligoynes possess limited electron delocalization along the carbon backbone, which exhibits appreciable bond-length alternation.[68,69] In some cases, significant backbone curvature is found in X-ray structural studies.[61] Theoretical studies have been reported both for hypothetical infinitely long polyyne carbon chains [$(C{\equiv}C–)_\infty$] and for finite length chains.[69,70] The synthesis of long oligoyne chains represents a considerable challenge due to the rapid decomposition of most $R–(C{\equiv}C–)_nH$ intermediates (R = alkyl, aryl, heteroaryl)[71,72] and the instability of the final $R–(C{\equiv}C–)_nR$ products (where n > 4) under ambient conditions. Small end-groups R are a particular concern in this regard. To overcome this lack of stability, the use of bulky end-groups R[73–75] and encapsulation of the oligoyne backbone within a rotaxane are known strategies to stabilize longer symmetrical $R–(C{\equiv}C–)_nR$ systems.[76–79]

In a previous preliminary study, it was established that triarylamine–$(C{\equiv}C–)_n$diaryloxadiazoles display intramolecular charge transfer.[50] In the current study, we combine tailored synthesis, solution electrochemistry (see SI), and spectroscopy to probe charge separation, transport, and recombination dynamics in a series of unsymmetrical $D–(C{\equiv}C–)_nA$ systems **1-4**. Importantly, the oligoyne length is systematically varied in **1-4**. On the one hand, *N*-arylcarbazoles[80] were chosen, because of their electron donation and their bulky non-planar structures, which are known to suppress oligoyne decomposition.[81] In addition, we attached *t*-butyl groups to the 3,6-positions of carbazole to enhance the solubility and to prevent unwanted side-reactions (e.g. dimerization).[82] On the other hand, we opted for 1,3,4-oxadiazoles, since they are synthetically versatile, reversible electron acceptors, and feature excellent chemical and photochemical stability, including high photoluminescence quantum yields (PLQY).[83,84] The electron-accepting oxadiazoles are directly π-conjugated with the bridge, in contrast to pyrrolidino-C_{60}, in which the conjugation is broken by the sp^3 carbon of the pyrrolidine fragment.[85]

Results and Discussion

Synthesis. **Caution:** Great care should be taken when handling oligoynes and their intermediates in bulk quantities, due to their potential explosive instability.[86]

The syntheses of **2** and **6** have been reported previously (Figure 1),[87] while those of **1**, **3**, and **4** are described in the Supporting Information. **3** (n = 3) and **4** (n = 4) were characterized by single-crystal X-ray diffraction of **3**·½EtOH, **4**·EtOH and **4**·2MeOH (Figures S1 and S2). The crystal structures are similar and the latter two are isomorphous. Each structure contains infinite channels around the twofold axes, [1/4 *y* 1/4] in **3**·½EtOH or [1/2 *y* 1/4] in the other two structures, filled by randomly disordered solvent molecules. In both **3** and **4** (Figure 2), the angles between the planar carbazole system *i*, phenylene rings *iii* and *v* and oxadiazole ring *iv* are small (Table 1), but out-of-plane orientation of the phenylene ring *ii* effectively precludes π-conjugation in the solid state. As usual,[61] the oligoyne rod shows a small but significant bend and distinct alternation of triple and single bonds.

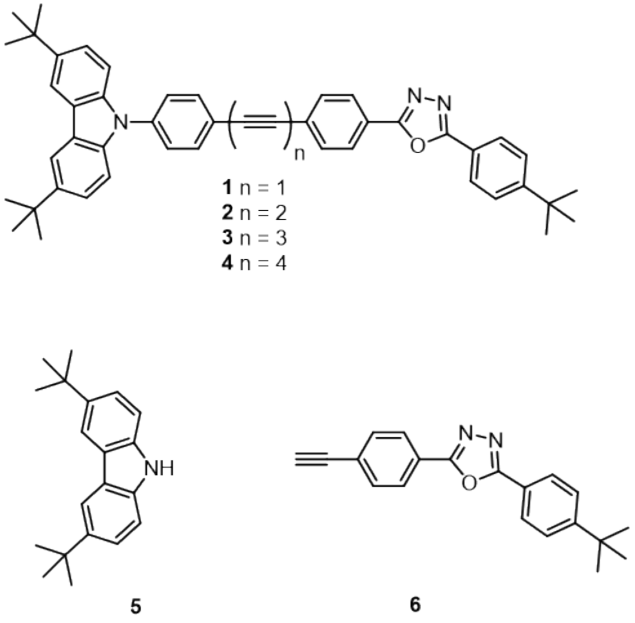

Figure 1. Molecular structures of **1-6** studied in this work.

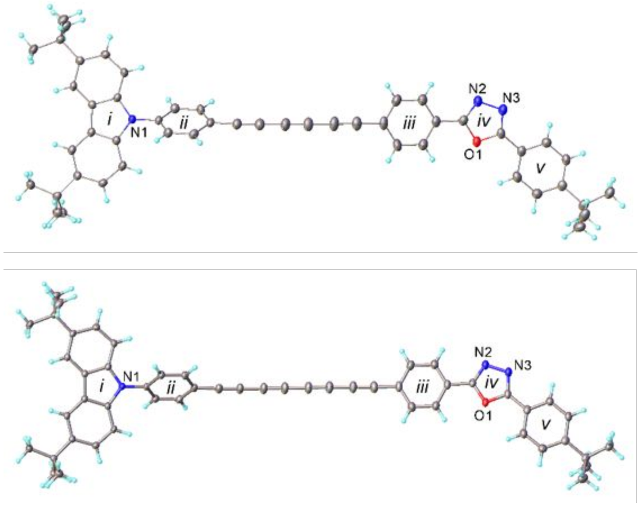

Figure 2. X-ray molecular structures of **3** and **4**.

Table 1. Intramolecular torsion angles (°) in **3** and **4**.

	3·½EtOH	**4**·EtOH	**4**·2MeOH
i/ii	58.6	55.1	53.3
ii/iii	70.0	66.2	65.6
i/iii	15.2	15.1	14.5
iii/iv	2.6	4.1	3.6
iv/v	9.0	7.7	7.6
Rod bend	10.8	12.0	11.6

Photophysics. Electronic interactions in the ground state were studied by a variety of photophysical methods. Please note the lack of spectroscopic evidence for any aggregation for the references/conjugates investigated in the concentration range of the photophysical experiments from 2.5×10^{-8} to 5×10^{-6} M (Figure S4). A comparison between the ground-state absorption spectra of the conjugates and the reference molecules **5** and **6** reveals sizable perturbations from just the simple superimpositions of the individual building blocks, suggesting electronic interactions between donor and acceptor moieties in the ground state (Figure 4). In particular, maximum absorptions of carbazole and oxadiazole develop in the region between 250 and 350 nm. The perturbation is particularly visible in the long-wavelength regions from 350 to 420 nm, where neither carbazole nor oxadiazole show any appreciable absorptions. It is important to note that the overall absorption characteristics give rise to a strong dependence on the length of the oligoyne bridges. At first glance, a bathochromic shift evolves as the number of alkynes is increased, which corroborates the π-conjugation of the oligoyne. The latter has also been observed by Wang *et al.* in their work on carbazole-oligoyne conjugates.[71] A closer look reveals, however, that coupling to the oxadiazoles leads to additional red shifts and the appearance of new absorptions, which are not relatable to any of the individual building blocks.

In complementary molecular modeling using the CAM-B3LYP range-separated density functional, the cc-pVDZ basis set, and including a polarizable continuum solvation model (PCM), we found only planar geometries for **1** and **2** in the ground state. In **3** and **4**, a larger degree of freedom enables the free rotation in the ground state (Figure 3). The activation barriers for rotation around the phenyl rings *ii* and *iii* range from 0.9 and 0.2 kcal mol^{-1} for **1** and **2** to less than 0.06 and 0.02 kcal mol^{-1} for **3** and **4**. Such small rotational barriers explain the differences seen in X-ray analyses, where the *ii*/*iii* torsion angle are in the range of 65°-70° (Table 1). As a result, a nearly planar alignment of the larger aromatic rings systems *i*/*iii* is achieved, which allows tighter crystal packing (Figures S1-S2). At room temperature and in solution, it is reasonable to assume a high flexibility around this torsional motion in **3** and **4**.

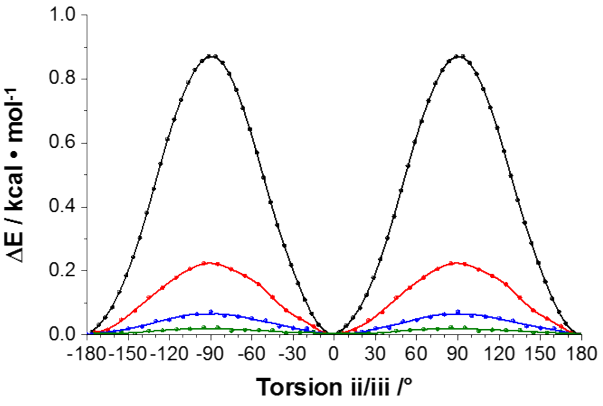

Figure 3. Relative change in ground state energy upon CAM-B3LYP/cc-pVDZ relaxed torsion scan varying dihedral angle *ii*/*iii*.

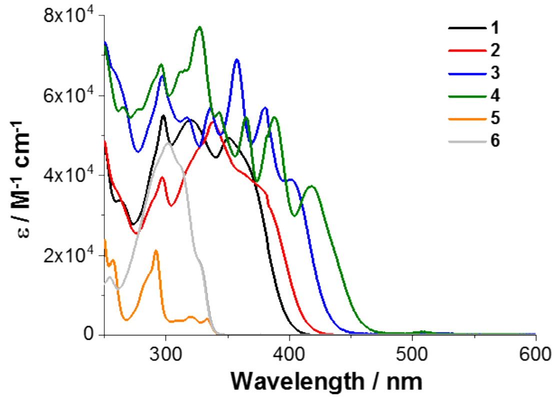

Figure 4. Room temperature absorption spectra of **1**-**6** in dichloromethane.

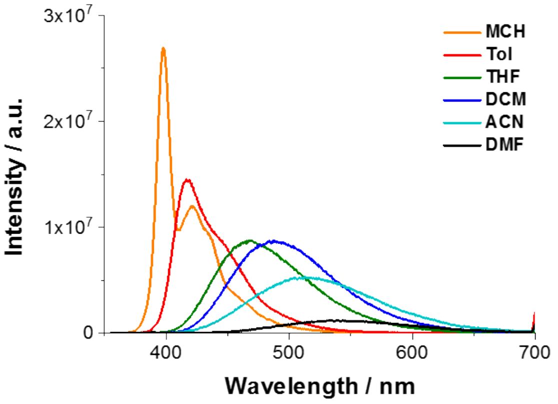

Figure 5. Fluorescence spectra of **2** in solvents of different polarity (MCH – methylcyclohexane, Tol – toluene, THF – tetrahydrofuran, DCM – dichloromethane, DMF – *N*,*N* – dimethylformamide) with matching the absorption of OD = 0.05 upon 350 nm excitation.

Influences of the torsional motion between the electron donors and acceptors on the absorption characteristics were confirmed independently in experiments. Decreasing the temperature from, for example, 293 to 85 K results in absorption spectra that feature vibrational fine structure and red-shifted maxima for **3** (Figure S5).

A distinct dependence on solvent polarity has been noted in **1**-**4** (Figure S6). As Figures S6b and 4 demonstrate, the finely structured absorption, which is discernable for **2** in non-polar solvents, is replaced by a featureless absorption spectrum in the more polar solvents. In addition, the rather sharp transitions in the 250 to 400 nm range found in methylcyclohexane, transform into less sharp transitions as the solvent polarity is changed. To shed light on the electronic interactions between the photo- and redox-active building blocks in their excited states, solvent polarity dependent emission measurements were carried out (Figures 5 and S7). In methylcyclohexane, the fluorescence spectra of all electron-donor-acceptor conjugates are dominated by a rather sharp 385 nm maximum along with some vibrational fine-structure. The high-energy 385 nm maximum disappears even upon a moderate increase in solvent polarity. At the same time, a broad and low energy fluorescence is detected. Its position and maximum red shift in more polar solvents; a finding from which we conclude its intramolecular charge transfer nature. In parallel, the excitation spectra of **1**-**4** in solvents of different polarity match the corresponding absorption spectra. The fine structure is observed only in methylcyclohexane. While in more polar solvents like THF and DMF, a significant broadening of absorption is noted in the 390-500 nm region (Figure S8). Insights into the role of the solvent came from plotting the Kirkwood parameter *versus* the fluorescence maximum. For all conjugates, a clear trend appears – Figure S9 – from which we conclude a better excited-state stabilization in solvents of higher polarity. Please note that the fluorescence maxima remain constant upon varying the excitation wavelength. As the length of the oligoyne increases a dramatic drop of fluorescence quantum yields from 0.71 for **1** to 0.005 for **4** is noted in, for example, toluene. Finally, going from non-polar to polar solvent an overall decrease in quantum yields is observable (Table 2). This is in contrast to the results presented by Biswas *et al.*, who reported a lack of quenching in an acetylene and butadiyne series (n = 1 and 2), when the solvent polarity was varied.[54]

Table 2. Fluorescence quantum yields (Φ_{Fl}) and lifetimes (τ_{TCSPC}).

	Φ_{Fl}^a		τ_{TCSPC} / ns			
	Toluene	DMF	MCH	THF	DMF	PhCN
1	0.71	0.38	1.07	2.56	4.12	
2	0.46	0.09	0.53	2.41	1.61	3.39
3	0.013	0.033	0.05 (97%), 2.40 (3%)	0.23 (79%), 1.47 (21%)	0.32 (89%), 1.82 (11%)	0.72 (42%), 1.52 (58%)
4	0.005	0.002	0.12 (94%), 3.05 (6%)	0.06 (89%), 2.77 (11%)	0.17 (77%), 3.06 (23%)	0.10 (89%), 2.27 (11%)
5	0.41	0.36	6.92	-	-	-
6	0.36	0.32	1.1	-	-	-

[a] Reasonable valuation of Φ_{Fl} in the other solvents was precluded due to the lack of matching references.

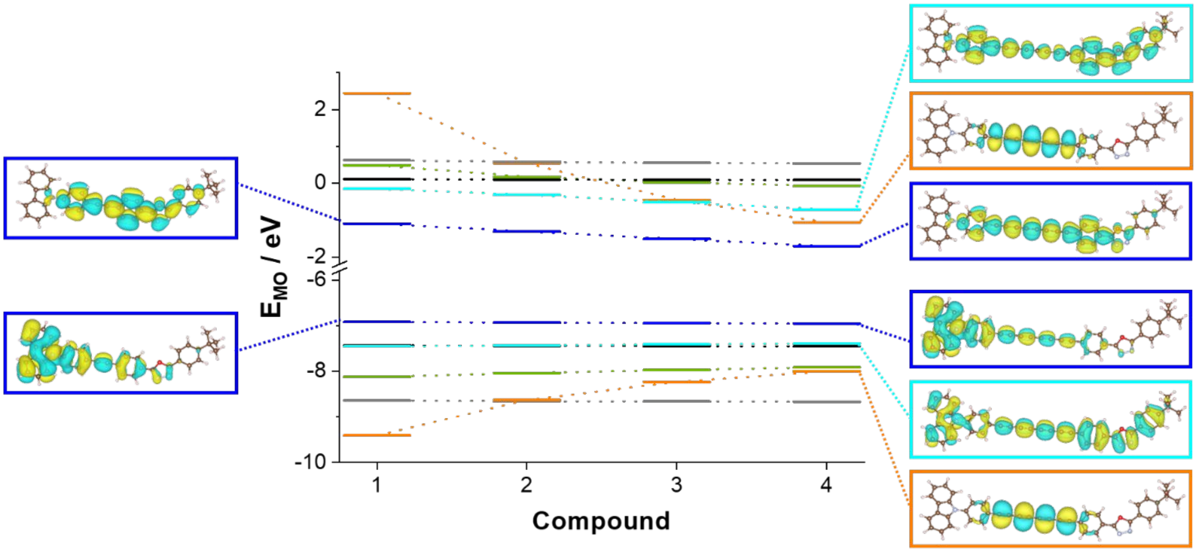

Figure 6. Molecular orbitals and their energies, predicted with TD CAM-B3LYP/cc-pVDZ single point calculation, based on the relaxed ground state geometries for **1**-**4**. MOs local to either electron donor or acceptor are shown in black and grey, those located on the oligoyne molecular wire in orange and delocalized MOs ranging from green towards cyan and blue.

For a better understanding of the electronic structure, absorption and fluorescence data, the molecular orbitals (MOs) and excited states were analyzed. As shown in Figure 6, the highest occupied and lowest unoccupied molecular orbitals, HOMO and LUMO, respectively, are widely spread over the molecular entities with significant overlap. In line with the electrochemical trends, the HOMO is mainly located on the carbazole electron donor, while the LUMO is located on the electron-accepting oxadiazole. A strong contribution from the oligoynes to occupied and unoccupied MOs shows the bridging states coming into resonance with either the electron donor or acceptor and, in turn, implies significant charge-transfer character.

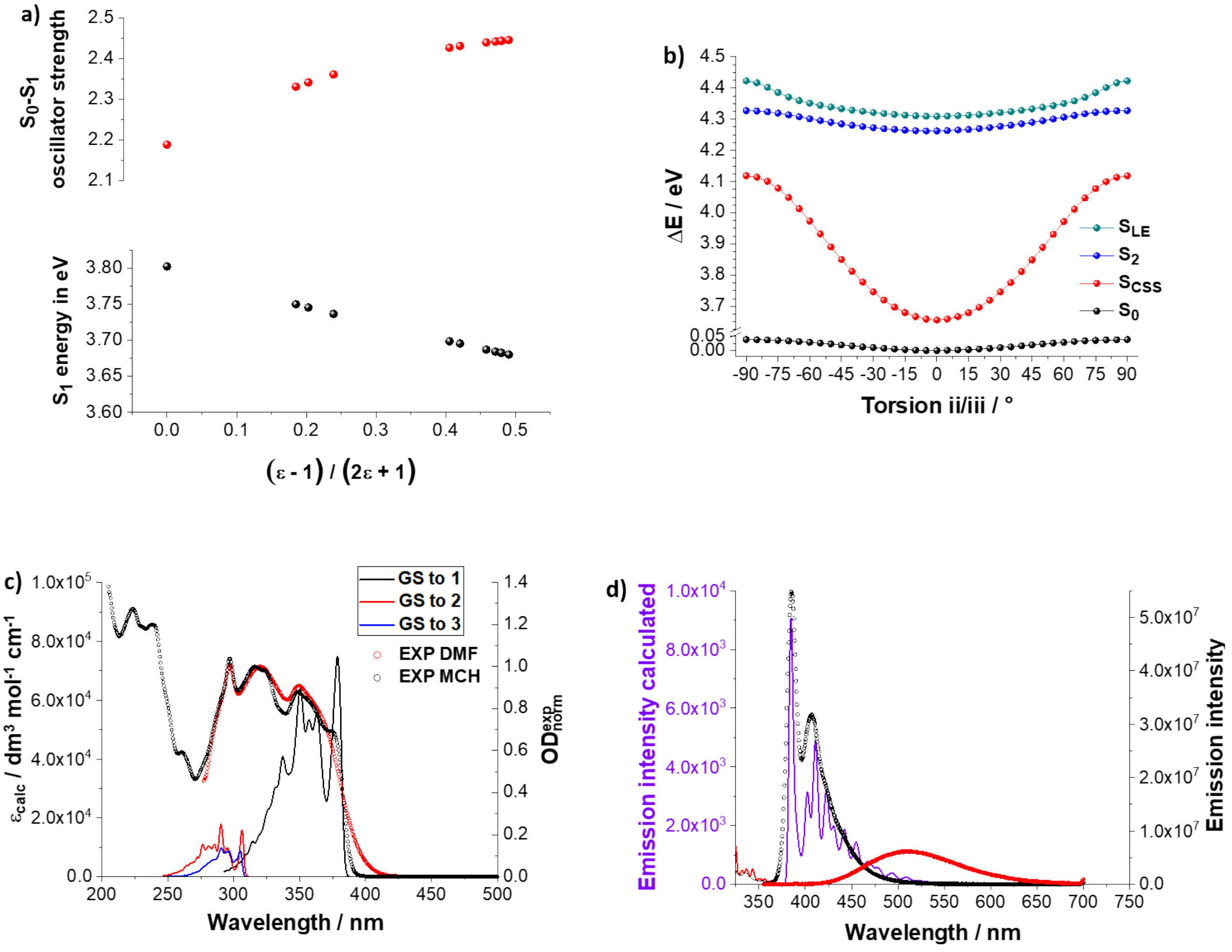

Figure 7. a) S_1 excited state energy (black) and oscillator strengths for the S_0-S_1 transition of **1** in solvents of different polarity. b) Ground and excited state energies of **1** upon variation of the torsion angle between rings *ii*/*iii*. c) Predicted vibrational resolved absorption spectra of **1** at 0 Kelvin for the S_0-S_1 transition (black), S_2 (red) and S_3 (blue), derived with the Frank Condon Herzberg Teller approach. Discrete energy values were summed with a Gaussian distribution of 135 cm^{-1} FWHM and compared to experimental absorbance spectra in MCH (black) and DMF (red). d) Predicted emission spectra of **1** at 0 Kelvin, utilizing the same approach (purple) and experimental results in MCH (black) and DMF (red).

Increasing the length of the bridge in **1** to **4** has several effects. First, the HOMO-LUMO gap is reduced, implying a red shift in absorption and fluorescence. Second, all molecular orbitals that feature contributions from the oligoynes are affected by the elongation of the spacer and reduce the HOMO-LUMO gap. This effect is most pronounced for the local MOs of the bridge (orange), but is also discernable for the delocalized MOs (green, cyan, and blue) and implies increasing electron acceptor strength of the oligoyne wire.[88] Notable is, however, that the local MOs on either electron donor or acceptor (grey and black) are unaffected by the length of the oligoyne.

Closer insights into the excited states were derived from time-dependent DFT calculations (TD-DFT) with CAM-B3LYP functional,[89] cc-pVDZ basis set,[90–93] and PCM solvation.[94] Please note that reference calculations were also carried out with the augmented triple ζ basis set aug-cc-pVTZ with the same functional and with the wB97XD,[95] LC- wHPBE,[96] M06-2X,[97] M06-HF,[98] and B3LYP functionals with the cc-pVDZ basis.[99] The larger basis set has minor effects on the vertical energies (Figure S24). The results with wB97XD and LC-wHPBE are in line with CAM-B3LYP. In contrast to those methods, B3LYP does not include any range separation corrections, and gives lower vertical excitation energies and a more pronounced CT character (Figure S25). As shown in Figure 7, the vertical excitation energies for **1** decrease with increasing solvent polarity, yielding an overall stabilization of 0.15 eV. At the same time, the oscillator strength increases for the S_0-S_1 transition. Qualitatively, this is in line with the absorption and fluorescence measurements, although CAM-B3LYP tends to underestimate the solvent stabilization. Of great relevance is the fact that the excited-state energy strongly depends on the torsion angle between ring systems *ii*/*iii*

(Figures 7 and S26-S27). For example, the S_1 excited state is stabilized by 0.4 eV during planarization (90° vs. 0°), which is more than one order of magnitude larger than the corresponding S_0 stabilization. Therefore, we postulate the replacement of random ground state conformation with a planar arrangement upon excitation and excited-state relaxation (Figure S28). Optimizations of all excited states below the carbazole centered local excited singlet state were performed to follow the geometrical changes along the excited state relaxation. Additional frequency calculations and scans varying either dihedral angle *ii*/*iii* (Figure S26-S27) or the single – triple bond lengths (Figure 11) along the wire assure reaching a stationary minimum on the excited state potential energy surface. Based on the frequency calculations a mixed approach of Frank Condon Herzberg Teller (FCHT) was utilized to predict vibrational resolved ground-to-excited-state absorption and excited-to-ground-state fluorescence. [100–104] Predicted and experimental spectra are in good agreement as shown in Figure 7.

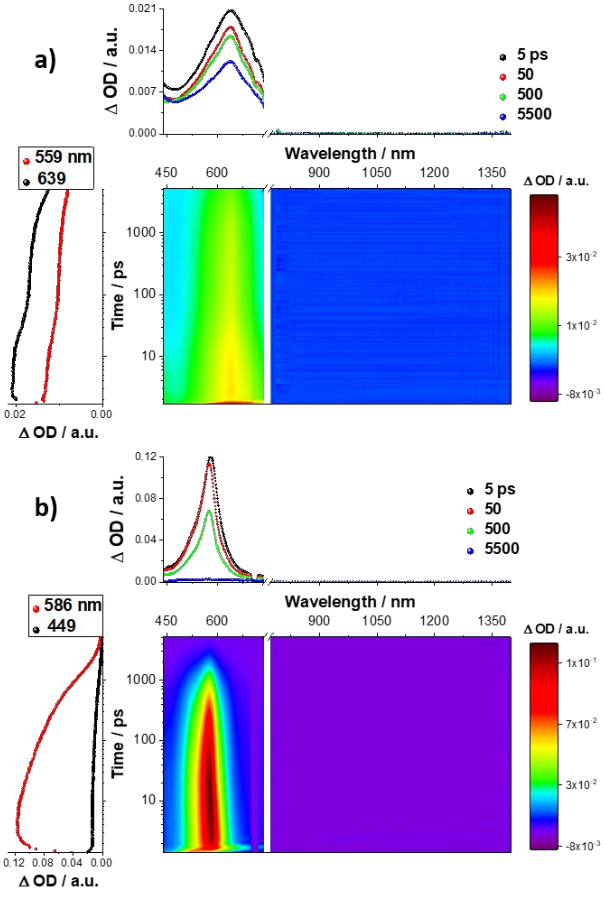

Figure 8. Differential absorption spectra (visible and near-infrared) obtained upon femtosecond flash photolysis (387 nm) of a) **5** and b) **6** in argon-saturated THF with several time delays between 0 and 5500 ps at room temperature. a) Lower left: Time absorption profiles of the spectra at 559 and 639 nm. Upper Right: Differential absorption spectra with the depicted time delays. b) Lower left: Time absorption profiles of the spectra at 449 and 586 nm. Upper Right: Differential absorption spectra with the depicted time delays.

To shed more light on the excited-state deactivation pathways, transient absorption spectroscopy measurements were performed. The experiments were conducted in MCH, THF, PhCN, and DMF by following 387 nm excitation for **1**-**4**, and 258 nm excitation for **5** and **6** on either the fs-to-ns (fs-TAS) or ns-to-μs (ns-TAS) timescales. Time-depended excited-state features and kinetics were inspected by means of multiwavelength and global/target analyses using the R-package TIMP[105] and the graphical user interface GloTarAn.[106] Figure 8 shows the differential absorption spectrum of **5** and **6** in THF upon 258 nm excitation. In both cases, immediately after excitation, transient maxima arise at 639 and 579 nm for **5** and **6**, respectively. For **5**, the excited-state decay exceeds our experimental resolution and based on the literature[107] the singlet-excited state transforms into the corresponding triplet features within 6.2 ns. As such, intersystem crossing (ISC) is the predominant deactivation for **5**. For **6**, the excited state deactivates within 1.0 ns. In both cases, the decays correlate well with the fluorescence lifetimes. Additionally, a short time component of 24 and 56 ps for **5** and **6**, respectively, evolved. We assign it to vibrational cooling.

Comparing the differential absorption spectra of **2** to those of **5** and **6**, clear changes are already discernable in methylcyclohexane: Transient absorption features evolve with maxima at 612, 805, and 1186 nm together with ground-state bleaching at 445 nm (Figure S10). All of these features decay within 568 ps to the energetically lower lying oxygen-sensitive triplet excited state via ISC. As the position and the shape of the long-lived features differ significantly from those found in **5**, delocalization of the triplet excited state within the molecule is implied. Moreover, new transients appear in the NIR region directly after photoexcitation, which are not seen in the references. The 612 nm maximum resembles the singlet excited-state transient seen for **5**. Owing, however, to the presence of the NIR feature and the red shifts in **1**-**4**, we postulate that the transients feature, at least, partial charge transfer character. Importantly, their deactivation lifetimes coincide with the fluorescence lifetimes. This is also reflected in **3**, for which the stimulated emission evolves within 1 ps and decays simultaneously with the other 568 ps transients. Notably, the stimulated emission in **1**, **2**, and **4** in methylcyclohexane is masked by the positive transients.

The situation clearly changes in polar solvents, including DMF – Figure 9. Immediately upon excitation of **2**, two maxima at 567 and 1252 nm are discernable in the differential absorption spectra. These are attributed to the charge-transfer excited state. Such a scenario is in line with the steady-state fluorescence measurements, which indicate charge-transfer states in more polar media. As time progresses, these transients are replaced within 1 ps by new blue-shifted maxima at 551 and 1211 nm, as a result of internal vibrational relaxation/solvent relaxation. The blue shift continues for the next 3.6 ps, generating a radical-ion pair state with maxima at 544, 805, and 1186 nm. The pronounced blue shift is rationalized on grounds of vibrational cooling and relaxation of the singlet-excited state. With the help of FCHT we modeled the vibrationally resolved transient absorption of the relaxed excited S_1 state towards S_2 and S_3 (Figure S29). It nicely matches the hypsochromic shifting NIR transient assigned for the contact radical ion pair – vide infra. As such, the experimentally observed transient absorbance features, which resemble the modeled absorbance of the populated S_1 state including higher lying (mainly) singlet excited states S_x, shift towards higher energies, as the S_1 state is more strongly stabilized than the higher lying S_2 and S_x states. Notably, charge recombination is biexponential with lifetimes for **2** of 720 and 1489 ps; the second component matches the fluorescence lifetime. Spectroscopic proof for the formation of the charge-separated state was gathered in pulse-radiolysis and spectroelectrochemical measurements – Figure S11. Interestingly, biexponential decays of the charge-separated state were noted in all conjugates. In **3** and **4**, the fluorescence decays are likewise biexponential and are in reasonable agreement with the charge-recombination dynamics. The detection of biexponential fluorescence decays in **1** and **2** is most likely to be unresolvable. On longer timescales, the fingerprints of oxygen-sensitive triplet excited state features are noted. The presence of a charge-separated state is even more pronounced in solvents of lower polarity like THF, as the charge recombination goes hand-in-hand with the formation of the triplet-excited state (Figures S12-S15). The charge-separated state deactivation occurs within a time frame from 1027 ps for **1** to 114 ps for **4** in DMF (Figures 9 and S16-S18). Table 3 lists all the lifetimes obtained. It is also interesting to note that the fluorescence lifetimes are in sound agreement with the charge-recombination dynamics.

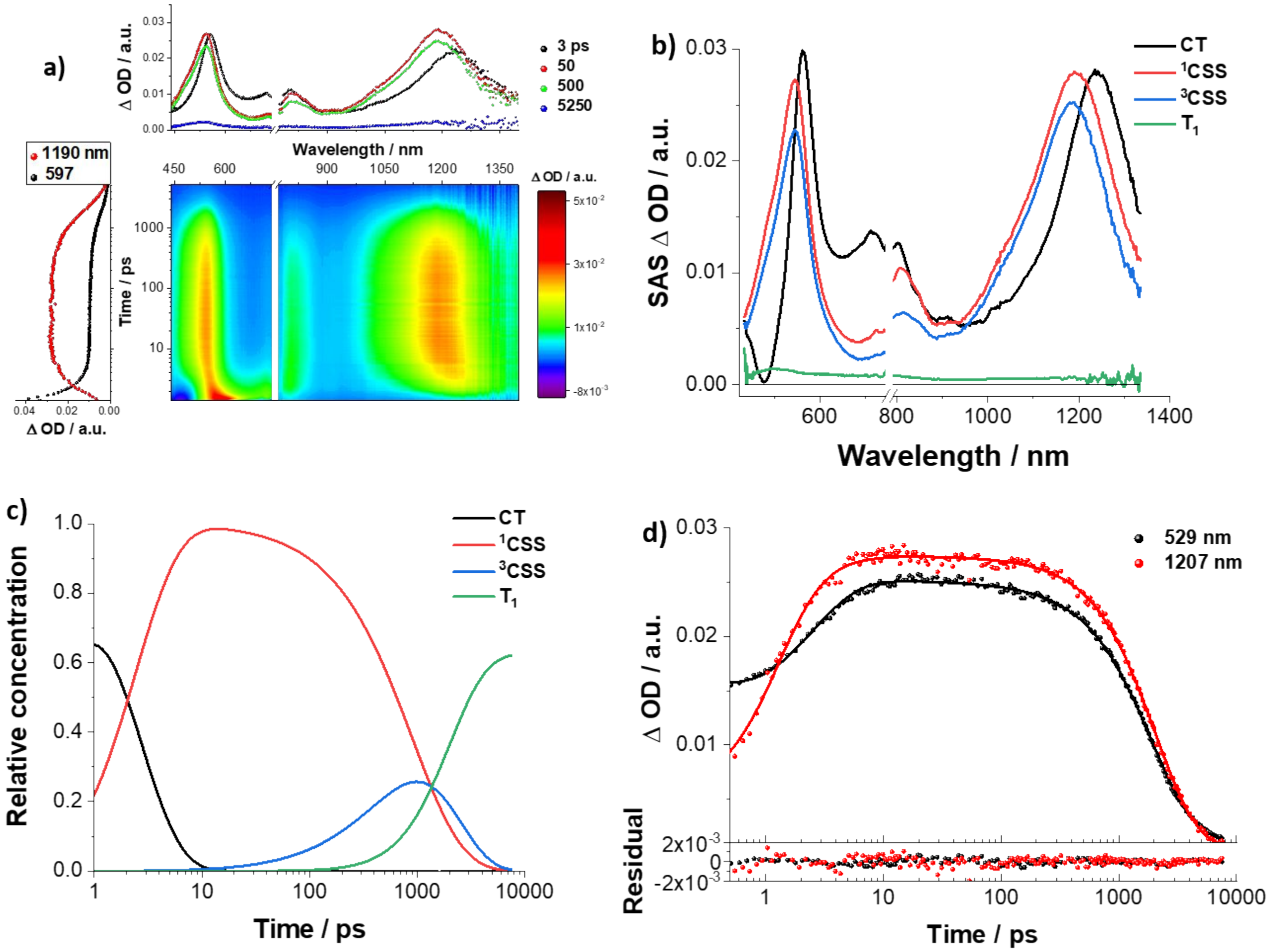

Figure 9. a) Differential absorption spectra (visible and near-infrared) obtained upon femtosecond flash photolysis (387 nm) of **2** in argon-saturated DMF with several time delays between 0 and 5500 ps at room temperature. Lower left: Time absorption profiles of the spectra at 597 and 1190 nm. Upper Right: Differential absorption spectra with the depicted time delays. b) Deconvoluted species associated spectra (SAS) of CT (black), ^{1}CSS (red), ^{3}CSS (blue), and T_1 (green) in DMF as obtained by global target analysis of time-resolved spectra on the sub-ps-to-ns timescale. c) Evolution of the population of the involved states in **2** in DMF. d) Time absorption profiles at 529 and 1207 nm as well as the corresponding fits and residuals.

This leads to several conclusions. First, the singlet charge-separated state is emissive, which is rather unusual for distance-separated electron-hole systems. Taking the HOMO and LUMO molecular orbitals into account, the partial character of the charge transfer, as well as the difference in electrostatic potential between S_0 and S_1 (Figure 10) we conclude a close contact between radical cation and radical anion. Consequently, we refer to the charge-separated state as a contact radical ion pair, which is known to emit.[108,109] Second, the match of the first emission lifetime with the transient absorption kinetics suggests that this state deactivates within less than 450 ps at least partially into the S_0 ground state. The population of a second species (Figure 9, blue), baring the same radical ion features in the transient absorption (Figure S32), proofs the parallel mechanism of this singlet radical ion pair state deactivation. Furthermore, the good spectral match between both states points towards a similar excited state energy, geometry and charge allocation. Hints towards the nature of this second charge separated species came from theory, as besides the singlet charge separated state (^{1}CSS/S_1) a triplet state is predicted that fulfills all three mentioned requirements (^{3}CSS). With <0.1 eV and <0.02 eV for **1** and **4**, respectively, the energies are in close proximity those of the ^{1}CSS (Figure S31). The electrostatic potential difference in Figure 10 features a similar contact radical ion character, although the oligoyne spacer is being reduced to a bigger extend. Finally, the geometrical changes, especially torsion angle *ii*/*iii* and single/triple bond lengths are comparable – showing an increased cumulenic character for both, ^{1}CSS and ^{3}CSS compared to S_0 (Figure 11 and Figure S31).

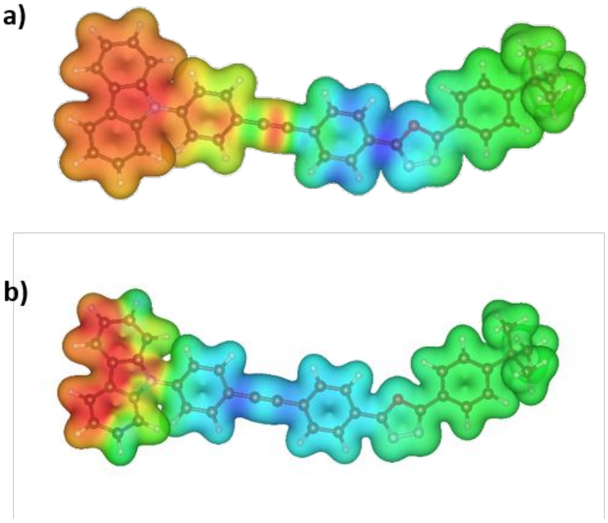

Figure 10. Electrostatic potential difference map (-0.015 — 0.015 a.u. from blue to red) of a) ^{1}CSS of **1** and b) ^{3}CSS of **1** color mapped on the electron density (isovalue = 0.015 a.u.).

To elucidate the potential-energy surfaces of these states, we performed a scan, in which the average single and triple bond lengths along the bridge of **4** are varied (Figure 11). Importantly, the potential surfaces of the triplet charge separated state (^{3}CSS, blue) and singlet charge separated state (^{1}CSS, red) cross and yield minima within less than 0.05 eV. Based on the similar energy, geometry, and charge delocalization, we assume an equilibrium between singlet and triplet charge-separated states. While the ^{1}CSS deactivates in the sub nanosecond time regime the ^{3}CSS charge recombination takes places within 3.6 to 1.5 ns for **1** and **4** in DMF, respectively. Interestingly, the decay kinetic of the ^{3}CSS species matches both: the population of the local triplet state (T_1) and the second emission lifetime obtained for compounds **3** and **4**. Considering the fast deactivation of the ^{3}CSS, the energetic and geometrical similarity with the ^{1}CSS and the time independent shape of the emission spectra we favor delayed fluorescence (Figure 14) over spin forbidden phosphorescence to be the cause of emission.

The analysis of the charge-transfer dynamics for **1**-**4** resulted in a number of interesting observations. Plotting, for example, the charge-recombination rate constants as a function of electron donor-acceptor distances revealed a rate constant increase as the oligoynes are elongated (Figure 13). At first, the charge-transfer processes between the electron donor/acceptor and the bridge were considered. This assumption is, however, not reflected in the transient absorption spectra, as the observed features clearly indicate the presence of the carbazole radical cation and the oxadiazole radical anion. As such, the potential change in the charge-transfer mechanism from superexchange to hopping was also considered. To this end, temperature-dependent femtosecond transient absorption experiments were carried out – Figure S23.[110] Importantly, the observations noted in room temperature PhCN are in sound agreement with results obtained in DMF (Figures S19-S22). The experiments revealed, however, no appreciable changes in the charge-recombination mechanism. We therefore also dismissed this hypothesis. Acceleration of the charge-recombination dynamics with increasing electron donor-acceptor distance has previously been reported due to a change from the superexchange to hopping mechanisms.[111,112] Such a mechanistic exchange is, however, reflected by a clear turnover in the dynamics as the bridge length increases.

In our work, however, we observed the continuing acceleration of the charge-recombination dynamics within the **1**-**4** series. Such unusual distance dependences of electron-transfer rates were previously reported by Kuss-Petermann and Wenger in rigid rod-like donor-photosensitizer-acceptor conjugates featuring *p*-xylene bridges. In their system, increase of electron-transfer rates with increasing donor-acceptor distances resulted from the interplay of a strong distance dependence of reorganization energy and a weak distance dependence of electronic coupling.[113–115] We included such a scenario in our analysis but the electronic couplings changed significantly within the **1**-**4** series (Table S3). One possible explanation is a better electronic coupling once the planarization takes place in the excited state. Another notable impact are differences in the single and triple bond lengths between the ground and excited state as the oligoyne length is increased. The latter is reflected in the ratio of the average lengths of C-C and C≡C bonds: d(C-C)/d(C≡C), which approaches one in both ^{1}CSS and ^{3}CSS (Figure 12).

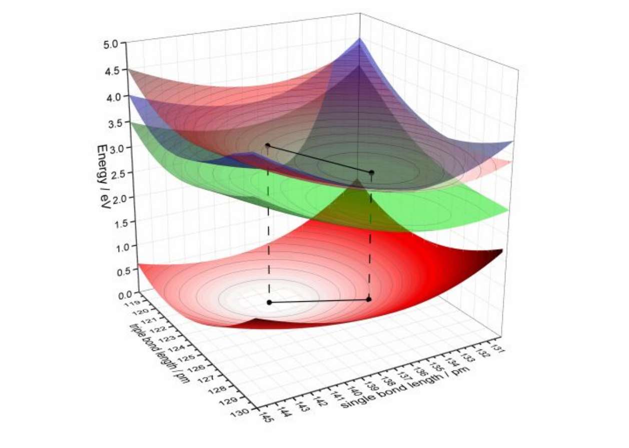

Figure 11. S_0 (red) relaxed potential energy surface, varying the average single and triple bond length in **4**. Vertical excited state energies for ^{1}CSS (light red), ^{3}CSS (blue) and T_1 (green), calculated with TD-CAM-B3LYP/cc-pVDZ.

Table 3. Lifetimes obtained from the multiwavelength and the global/target analyses.

Compound	Solvent	τ_1 / ps	τ_2 / ps	τ_3 / ps	τ_4 / ps	τ_5 / µs
1	MCH	< 1	1322	-	-	-
	THF	< 1	2.3	456	2719	1.9
	PhCN	3.5	16	1049	7249	
	DMF	< 1	3.5	1027	3647	2.1
2	MCH	< 1	568	-	-	2.6
	THF	1.2	3.4	424	1990	0.6
	PhCN	4.3	13	936	3423	19
	DMF	1.0	3.6	720	1489	5.38
3	MCH	1.5	25	-	-	4.0
	THF	< 1	6	214	2046	0.54
	PhCN	< 1	11	610	1270	37
	DMF	1.1	6	383	1376	1.88
4	MCH	8.62	103	-	-	2.8
	THF	1	5	77	2465	0.45
	PhCN	< 1	9	157	1772	43
	DMF	2.1	7.6	114	1553	7.64

As the length of the oligoynes increases, significant cumulenic character is noted for the bridge in the excited state. A cumulenic rather than a oligoynic structure is expected to accelerate any electron transfer in general, and charge recombination in particular.[35,116] The fast intersystem crossing between ^{1}CCS and ^{3}CCS on timescales in the range from 100 to 1000 ps, however, seems unusual. Similarly, ^{1}CT ⟶ ^{3}(π-π*) transitions occur with 100 ps and 1 ns in solutions and thin films, respectively. A fast reverse intersystem crossing was explained based on the mixing of the states involved.[117] In the current study, ^{1}CSS and ^{3}CSS are not only nearly identical energetically, but also in terms of their geometries and bond lengths. In addition, T_1 is still of cumulenic character and, therefore similar to ^{1}CSS and ^{3}CSS, as demonstrated in the form of d(C-C)/d(C≡C) in Figure 12. This points to strong vibronic coupling between the electron-donating *N*-arylcarbazoles and the electron-accepting 1,3,4-oxadiazoles in ^{1}CSS, ^{3}CSS, and also T_1, which, in turn, fosters significant second-order coupling effects to accelerate the intersystem crossing between ^{1}CSS and ^{3}CSS in forward and backward directions.[118–121]

Notably, the Duschinsky transformation, which expresses excited-state vibrational modes in terms of ground-state vibrational modes, clearly indicates strong changes, especially in the region of C-C and C≡C stretching vibrations. The off-diagonal elements in the Duschinsky Matrix (J) and the shift vector (K) corroborate such a transformation (Figure S30). Vibrations stimulated during a transition between ground and charge-separated singlet state and vice versa accompany the electron-transfer process. This points towards vibrational couplings and therefore acceleration of the charge-recombination, as the dipole strength, correlated with transitions involving the bridge centered stretch vibrations, increased within the **1**-**4** series.

From multiwavelength analyses of fs-TAS and ns-TAS, we concluded a fairly complex deactivation pattern with at least five different lifetimes. The shortest lifetime of ~1 ps is assigned to relaxation processes and was detected only through multiwavelength analysis. As such, on the basis of the abovementioned observations and theoretical investigation, we postulated the four-species kinetic model shown in Figure 14.

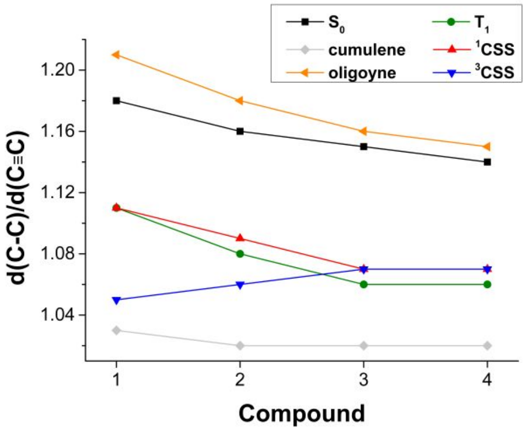

Figure 12. Ratio of the averaged C-C to C≡C bonds, that is, d(C-C)/d(C≡C) for S_0 (black), lowest T_1 (green), ^{1}CSS (red) and ^{3}CSS (blue) in comparison to reference cumulenes (grey) and oligoynes (orange). Details can be found in Figure S31.

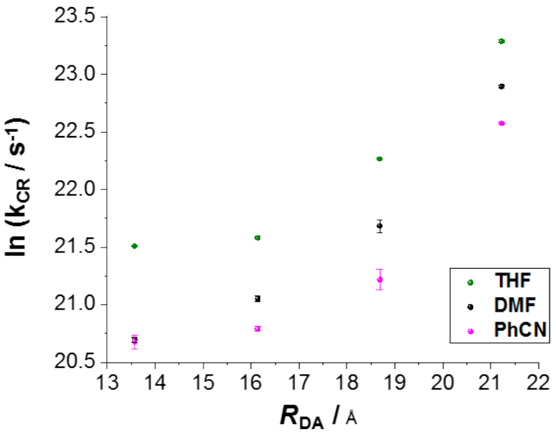

Figure 13. Logarithmic plot of charge recombination rate constant (k_{CR}) vs electron donor-acceptor distance (R_{DA}) in THF, PhCN, and DMF.

We tested its accuracy by means of Global and Target Analyses (Glotaran)/TIMP. The resulting species-associated spectra (SAS) and fits corroborate the multiwavelength analysis. In **2**, the first species is short-lived with a lifetime of 3.6 ps in DMF and is assigned to the CT state. As the CT decays, formation of the charge-separated state, the radical cation and radical anion with features at 544, 805, and 1186 nm, is noted. Interestingly, the fluorescence decay of **2** in DMF is in good agreement with the transient absorption kinetics.

In other words, the singlet charge-separated state (^{1}CSS) with a 720 ps lifetime is postulated, on the one hand, to recombine to the ground state and, on the other hand, to form the triplet charge-separated state (^{3}CSS) as the third species. The latter has a 1489 ps lifetime. Importantly, ^{3}CSS bears the radical-ion-pair features. Experiments involving magnetic field dependencies are precluded by the relatively short lifetimes of ^{3}CSS. In short, taking the resolvable biexponential decay of the fluorescence in **3** and **4** and the theoretical considerations into consideration, the following conclusions were drawn: ^{3}CSS partially inverts to ^{1}CSS, but at the same time its recombination yields the neutral triplet-excited state, which is the fourth species.

In conclusion, we report here a series of electron donor-bridge-acceptor conjugates, in which the electron transfer rates increase by a factor of 9 when the electron donor-acceptor distance is extended from 13.5 to 21.2 Å. Significant delocalization of the electron density along the bridge indicates that the bridging states come into resonance with either the electron donor or acceptor and, in turn, accelerate the charge transfer. Moreover, the calculated bond lengths reveal a reduction in bond-length alternation upon photoexcitation, indicating significant cumulenic character of the bridge in the excited state. Altogether, as the oligoyne becomes longer, significant vibronic coupling between the electron donating *N*-arylcarbazoles and the electron accepting 1,3,4-oxadiazoles accelerates the charge recombination.

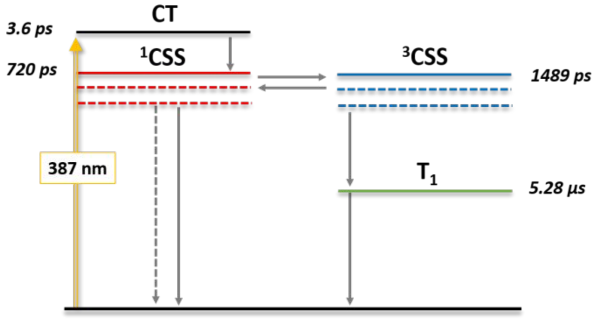

Figure 14. Mechanistic model used to deconvolute the excited state surfaces of **2** in THF, DMF, and PhCN via GloTaRan and the obtained lifetimes in DMF. The shortest component was omitted in the figure for the clarity of presentation.

ASSOCIATED CONTENT

Synthetic details and characterization, electrochemical and photophysical data, and theoretical details. This material is available free of charge via the Internet at http://pubs.acs.org.

AUTHOR INFORMATION

Corresponding Author

* **Prof. Dr. Dirk M. Guldi,** - Department of Chemistry and Pharmacy & Interdisciplinary Center for Molecular Materials (ICMM), Friedrich-Alexander-Universität Erlangen-Nürnberg, Egerlandstr. 3, 91058 Erlangen, Germany, phone: +49 9131 8527341, fax: +49 9131 85-28307, email: dirk.guldi@fau.de

* **Prof. Dr. Martin R. Bryce**, - Department of Chemistry, Durham University, Durham DH1 3LE, United Kingdom.
Phone: +41 (0)191 334 2018, fax: +41 (0)191 384 4737,
email: m.r.bryce@durham.ac.uk;

Author Contributions

□A.Z. and X.Z. contributed equally to this work.

ORCID

Andrei S. Batsanov: 0000-0002-4912-0981

Martin R. Bryce: 0000-0003-2097-7823

Timothy Clark: 0000-0001-7931-4659

Dirk M. Guldi: 0000-0002-3960-1765

Axel Kahnt: 0000-0002-8142-0511

Anna Zieleniewska: 0000-0001-9987-7520

ACKNOWLEDGMENT

This work was supported by EC FP7 ITN “MOLESCO” Project No. 606728 and by the Solar Technologies go Hybrid (SolTech) initiative of the Bavarian State Government.

REFERENCES

(1) Kippelen, B.; Bredas, J.-L. Organic Photovoltaics. *Energy Environ. Sci.* **2009**, *2*, 251–261.

(2) Kurreck, H.; Huber, M. Model Reactions for Photosynthesis—Photoinduced Charge and Energy Transfer between Covalently Linked Porphyrin and Quinone Units. *Angew. Chemie Int. Ed. English* **1995**, *34* (8), 849–866.

(3) Weiss, E.; Wasielewski, M. R.; Ratner, M. A. Molecules as Wires: Molecule-Assisted Movement of Charge and Energy. *Top. Curr. Chem.* **2005**, *257* (July), 103–133.

(4) Thompson, B. C.; Fréchet, J. M. J. Polymer-Fullerene Composite Solar Cells. *Angew. Chemie - Int. Ed.* **2008**, *47* (1), 58–77.

(5) Günes, S.; Neugebauer, H.; Sariciftci, N. S. Conjugated Polymer-Based Organic Solar Cells. *Chem. Rev.* **2007**, *107*, 1324–1338.

(6) Delgado, J. L.; Bouit, P. A.; Filippone, S.; Herranz, M. Á.; Martín, N. Organic Photovoltaics: A Chemical Approach. *Chem. Commun.* **2010**, *46* (27), 4853–4865.

(7) Dennler, G.; Scharber, M. C.; Brabec, C. J. Polymer-Fullerene Bulk Heterojunction Solar Cells. *Adv. Mater.* **2009**, *21*, 1323–1338.

(8) ChemPhysChem. Special Issue: Organic Electronics. *Spec. Issue Org. Electron.* **2015**, *16*, 1097.

(9) Wasielewski, M. R. Energy, Charge, and Spin Transport in Molecules and Self-Assembled Nanostructures Inspired by Photosynthesis. *J. Org. Chem.* **2006**, *71*, 5051–5066.

(10) Zinth, W.; Wachtveitl, J. The First Picoseconds in Bacterial Photosynthesis - Ultrafast Electron Transfer for the Efficient Conversion of Light Energy. *ChemPhysChem* **2005**, *6* (5), 871–880.

(11) Oevering, H.; Paddon-Row, M. N.; Heppener, M.; Oliver, A. M.; Cotsaris, E.; Verhoeven, J. W.; Hush, N. S. Long-Range Photoinduced Through-Bond Electron Transfer and Radiative Recombination via Rigid Nonconjugated Bridges: Distance and Solvent Dependence. *J. Am. Chem. Soc.* **1987**, *109* (11), 3258–3269.

(12) Kirner, S.; Sekita, M.; Guldi, D. M. 25Th Anniversary Article: 25 Years of Fullerene Research in Electron Transfer Chemistry. *Adv. Mater.* **2014**, *26* (10), 1482–1493.

(13) Albinsson, B.; Eng, M. P.; Pettersson, K.; Winters, M. U. Electron and Energy Transfer in Donor-Acceptor Systems with Conjugated Molecular Bridges. *Phys. Chem. Chem. Phys.* **2007**, *9* (44), 5847–5864.

(14) Benniston, A. C.; Harriman, A. Controlling Electron Exchange in Molecular Assemblies. *Coord. Chem. Rev.* **2008**, *252*, 2528–2539.

(15) Schubert, C.; Margraf, J. T.; Clark, T.; Guldi, D. M. Molecular Wires - Impact of Pi-Conjugation and Implementation of Molecular Bottlenecks. *Chem. Soc. Rev.* **2015**, *44*, 988–998.

(16) de Cola, L. Molecular Wires: From Design to Properties; de Cola, L., Ed.; Springer Berlin Heidelberg, 2005; pp 63–103.

(17) Eng, M. P.; Albinsson, B. Non-Exponential Distance Dependence of Bridge-Mediated Electronic Coupling. *Angew. Chemie - Int. Ed.* **2006**, *45* (34), 5626–5629.

(18) Santos, J.; Illescas, B. M.; Wielopolski, M.; Silva, A. M. G.; Tomé, A. C.; Guldi, D. M.; Martin, N. Efficient Electron Transfer in β-Substituted Porphyrin-C60 Dyads Connected through a p-Phenylenevinylene Dimer. *Tetrahedron* **2008**, *64*, 11404–11408.

(19) Van Hal, P. A.; Meskers, S. C. J.; Janssen, R. A. J. Photoinduced Energy and Electron Transfer in Oligo(p-Phenylene Vinylene)-Fullerene Dyads. *Appl. Phys. A Mater. Sci. Process.* **2004**, *79* (1), 41–46.

(20) Toivonen, T. L. J.; Hukka, T. I. A Density Functional Theory (DFT) and Time-Dependent Density Functional Theory (TDDFT) Study on Optical Transitions in Oligo(p-Phenylenevinylene)- Fullerene Dyads and the Applicability to Resonant Energy Transfer. *J. Phys. Chem. A* **2007**, *111* (22), 4821–4828.

(21) de la Torre, G.; Giacalone, F.; Segura, J. L.; Martín, N.; Guldi, D. M. Electronic Communication through Pi-Conjugated Wires in Covalently Linked Porphyrin/C60 Ensembles. *Chem. - A Eur. J.* **2005**, *11* (4), 1267–1280.

(22) Figueira-Duarte, T. M.; Gégout, A.; Nierengarten, J. F. Molecular and Supramolecular C60-Oligophenylenevinylene Conjugates. *Chem. Commun.* **2007**, No. 2, 109–119.

(23) Nierengarten, J. F.; Gu, T.; Aernouts, T.; Geens, W.; Poortmans, J.; Hadziioannou, G.; Tsamouras, D. Fullerene-Oligophenyleneethynylene Conjugates: Relationships between Charge-Carrier Mobility, Photovoltaic Characteristics and Chemical Structure. *Appl. Phys. A Mater. Sci. Process.* **2004**, *79* (1), 47–49.

(24) Koynov, K.; Bahtiar, A.; Bubeck, C.; Mühling, B.; Meier, H. Effect of Donor-Acceptor Substitution on the Nonlinear Optical Properties of Oligo(1,4-Phenyleneethynylene)s Studied by Third Harmonic Generation Spectroscopy. *J. Phys. Chem. B* **2005**, *109* (20), 10184–10188.

(25) Zhao, Y.; Shirai, Y.; Slepkov, A. D.; Cheng, L.; Alemany, L. B.; Sasaki, T.; Hegmann, F. A.; Tour, J. M. Synthesis, Spectroscopic and Nonlinear Optical Properties of Multiple [60]Fullerene-Oligo(p-Phenylene Ethynylene) Hybrids. *Chem. - A Eur. J.* **2005**, *11* (12), 3643–3658.

(26) Fortage, J.; Göransson, E.; Blart, E.; Becker, H. C.; Hammarström, L.; Odobel, F. Strongly Coupled Zinc Phthalocyanine-Tin Porphyrin Dyad Performing Ultra-Fast Single Step Charge Separation over a 34 Å Distance. *Chem. Commun.* **2007**, No. 44, 4629–4631.

(27) Pu, K. Y.; Qi, X. Y.; Yang, Y. L.; Lu, X. M.; Li, T. C.; Fan, Q. L.; Wang, C.; Liu, B.; Chan, H. S. O.; Huang, W. Supramolecule-Regulated Photophysics of Oligo(p-Phenyleneethynylene)-Based Rod-Coil Block Copolymers: Effect of Molecular Architecture. *Chem. - A Eur. J.* **2008**, *14* (4), 1205–1215.

(28) Lembo, A.; Tagliatesta, P.; Guldi, D. M.; Wielopolski, M.; Nuccetelli, M. Porphyrin - -Oligo-Ethynylenephenylene - [60] Fullerene Triads : Synthesis and Electrochemical and Photophysical Characterization of the New Porphyrin - Oligo-PPE - [60] Fullerene Systems. *J. Phys. Chem.* **2009**, *113*, 1779–1793.

(29) Linton, K. E.; Fox, M. A.; Pålsson, L. O.; Bryce, M. R. Oligo(p-Phenyleneethynylene) (OPE) Molecular Wires: Synthesis and Length Dependence of Photoinduced Charge Transfer in OPEs with Triarylamine and Diaryloxadiazole End Groups. *Chem. - A Eur. J.* **2015**, *21* (10), 3997–4007.

(30) Atienza-Castellanos, C.; Wielopolski, M.; Guldi, D. M.; van der Pol, C.; Bryce, M. R.; Filippone, S.; Martín, N. Determination of the Attenuation Factor in Fluorene-Based Molecular Wires. *Chem. Commun. (Camb).* **2007**, No. 48, 5164–5166.

(31) Wielopolski, M.; de Miguel Rojas, G.; van der Pol, C.; Brinkhaus, L.; Katsukis, G.; Bryce, M. R.; Clark, T.; Guldi, D. M. Control over Charge Transfer through Chemical Structure Modifications. *ACS Nano* **2010**, *4* (11), 6449–6462.

(32) Walther, M. E.; Grilj, J.; Hanss, D.; Vauthey, E.; Wenger, O. S. Photoinduced Processes in Fluorene-Bridged Rhenium-Phenothiazine Dyads - Comparison of Electron Transfer across Fluorene, Phenylene, and Xylene Bridges. *Eur. J. Inorg. Chem.* **2010**, No. 30, 4843–4850.

(33) Schubert, C.; Wielopolski, M.; Mewes, L. H.; de Miguel Rojas, G.; van der Pol, C.; Moss, K. C.; Bryce, M. R.; Moser, J. E.; Clark, T.; Guldi, D. M. Precise Control of Intramolecular Charge-Transport: The Interplay of Distance and Conformational Effects. *Chem. - A Eur. J.* **2013**, *19* (23), 7575–7586.

(34) Wielopolski, M.; Santos, J.; Illescas, B. M.; Ortiz, A.; Insuasty, B.; Bauer, T.; Clark, T.; Guldi, D. M.; Martín, N. Vinyl Spacers - Tuning Electron Transfer through Fluorene-Based Molecular Wires. *Energy Environ. Sci.* **2011**, *4* (3), 765–771.

(35) Sukegawa, J.; Schubert, C.; Zhu, X.; Tsuji, H.; Guldi, D. M.; Nakamura, E. Electron Transfer through Rigid Organic Molecular Wires Enhanced by Electronic and Electron-Vibration Coupling. *Nat. Chem.* **2014**, *6* (10), 899–905.

(36) Narutaki, M.; Takimiya, K.; Otsubo, T.; Harima, Y.; Zhang, H.; Araki, Y.; Ito, O. Synthesis and Photophysical Properties of Two Dual Oligothiophene-Fullerene Linkage Molecules as Photoinduced Long-Distance Charge Separation Systems. *J. Org. Chem.* **2006**, *71* (5), 1761–1768.

(37) Huang, C. H.; McClenaghan, N. D.; Kuhn, A.; Hofstraat, J. W.; Bassani, D. M. Enhanced Photovoltaic Response in Hydrogen-Bonded All-Organic Devices. *Org. Lett.* **2005**, *7* (16), 3409–3412.

(38) Petrella, A.; Cremer, J.; De Cola, L.; Bäuerle, P.; Williams, R. M. Charge Transfer Processes in Conjugated Triarylamine-Oligothiophene-Perylenemonoimide Dendrimers. *J. Phys. Chem. A* **2005**, *109* (51), 11687–11695.

(39) Oswald, F.; Islam, D. M. S.; Araki, Y.; Troiani, V.; Caballero, R.; de la Cruz, P.; Ito, O.; Langa, F. High Effectiveness of Oligothienylenevinylene as Molecular Wires in Zn-Porphyrin and C60 Connected Systems. *Chem. Commun.* **2007**, No. 43, 4498–4500.

(40) Winters, M. U.; Dahlstedt, E.; Blades, H. E.; Wilson, C. J.; Frampton, M. J.; Anderson, H. L.; Albinsson, B. Probing the Efficiency of Electron Transfer through Porphyrin-Based Molecular Wires. *J. Am. Chem. Soc.* **2007**, *129* (14), 4291–4297.

(41) Barigelletti, F.; Flamigni, L.; Guardigli, M.; Juris, A.; Beley, M.; Chodorowski-Kimmes, S.; Collin, J.-P.; Sauvage, J.-P. Energy Transfer in Rigid Ru (II)/ Os (II) Dinuclear Complexes with Biscyclometalating Bridging Ligands Containing a Variable Number of Phenylene Units. *Inorg. Chem.* **1996**, *35* (II), 136–142.

(42) Berresheim, A. J.; Müller, M.; Müllen, K. Polyphenylene Nanostructures. *Chem. Rev.* **1999**, *99* (7), 1747–1786.

(43) Schlicke, B.; Belser, P.; De Cola, L.; Sabbioni, E.; Balzani, V. Photonic Wires of Nanometric Dimensions. Electronic Energy Transfer in Rigid Rodlike Ru(Bpy)32+-(Ph)(n)-Os(Bpy)32+ Compounds (Ph = 1,4- Phenylene; n = 3, 5, 7). *J. Am. Chem. Soc.* **1999**, *121* (17), 4207–4214.

(44) Helms, A.; Heiler, D.; McLendon, G. Electron Transfer in Bis-Porphyrin Donor-Acceptor Compounds with Polyphenylene Spacers Shows a Weak Distance Dependence. *J. Am. Chem. Soc.* **1992**, *114* (15), 6227–6238.

(45) Cohen, R.; Stokbro, K.; Martin, J. M. L.; Ratner, M. A. Charge Transport in Conjugated Aromatic Molecular Junctions: Molecular Conjugation and Molecule-Electrode Coupling. *J. Phys. Chem. C* **2007**, *111* (40), 14893–14902.

(46) Guldi, D. M.; Illescas, B. M.; Atienza, C. M.; Wielopolski, M.; Martín, N. Fullerene for Organic Electronics. *Chem. Soc. Rev.* **2009**, *38* (6), 1587–1597.

(47) Vail, S. A.; Krawczuk, P. J.; Guldi, D. M.; Palkar, A.; Echegoyen, L.; Tomé, J. P. C.; Fazio, M. A.; Schuster, D. I. Energy and Electron Transfer in Polyacetylene-Linked Zinc-Porphyrin-[60]Fullerene Molecular Wires. *Chem. - A Eur. J.* **2005**, *11* (11), 3375–3388.

(48) Vail, S. A.; Schuster, D. I.; Guldi, D. M.; Isosomppi, M.; Tkachenko, N.; Lemmetyinen, H.; Palkar, A.; Echegoyen, L.; Chen, X.; Zhang, J. Z. H. Energy and Electron Transfer in Beta-Alkynyl-Linked Porphyrin-[60]Fullerene Dyads. *J. Phys. Chem. B* **2006**, *110*, 14155–14166.

(49) Wang, C.; Batsanov, A. S.; Bryce, M. R.; Martín, S.; Nichols, R. J.; Higgins, S. J.; García-Suárez, V. M.; Lambert, C. J. Oligoyne Single Molecule Wires. *J. Am. Chem. Soc.* **2009**, *131* (43), 15647–15654.

(50) Pålsson, L.-O.; Wang, C.; Batsanov, A. S.; King, S. M.; Beeby, A.; Monkman, A. P.; Bryce, M. R. Efficient Intramolecular Charge Transfer in Oligoyne-Linked Donor-Pi-Acceptor Molecules. *Chem. - A Eur. J.* **2010**, *16* (5), 1470–1479.

(51) Luu, T.; Morisaki, Y.; Cunningham, N.; Tykwinski, R. R. One-Pot Formation and Derivatization of Di- and Triynes Based on the Fritsch-Buttenberg-Wiechell Rearrangement. *J. Org. Chem.* **2007**, *72* (25), 9622–9629.

(52) Luu, T.; Morisaki, Y.; Tykwinski, R. R. One-Pot Synthesis and Functionalization of Polyynes via Alkylidene Carbenoids. *Synthesis (Stuttg).* **2008**, No. 7, 1158–1162.

(53) Eisler, S.; Chahal, N.; McDonald, R.; Tykwinski, R. R. Alkyne Migration in Alkylidene Carbenoid Species: A New Method of Polyyne Synthesis. *Chem. - A Eur. J.* **2003**, *9* (11), 2542–2550.

(54) Biswas, M.; Nguyen, P.; Marder, T. B.; Khundkar, L. R. Unusual Size Dependence of Nonradiative Charge Recombination Rates in Acetylene-Bridged Compounds. *J. Phys. Chem. A* **1997**, *101* (9), 1689–1695.

(55) Štefko, M.; Tzirakis, M. D.; Breiten, B.; Ebert, M.-O.; Dumele, O.; Schweizer, W. B.; Gisselbrecht, J.-P.; Boudon, C.; Beels, M. T.; Biaggio, I.; et al. Donor-Acceptor (D-A)-Substituted Polyyne Chromophores: Modulation of Their Optoelectronic Properties by Varying the Length of the Acetylene Spacer. *Chem. - A Eur. J.* **2013**, *19* (38), 12693–12704.

(56) Moreno-García, P.; Gulcur, M.; Manrique, D. Z.; Pope, T.; Hong, W.; Kaliginedi, V.; Huang, C.; Batsanov, A. S.; Bryce, M. R.; Lambert, C.; et al. Single-Molecule Conductance of Functionalized Oligoynes: Length Dependence and Junction Evolution. *J. Am. Chem. Soc.* **2013**, *135* (33), 12228–12240.

(57) Ballmann, S.; Hieringer, W.; Härtle, R.; Coto, P. B.; Bryce, M. R.; Görling, A.; Thoss, M.; Weber, H. B. The Role of Vibrations in Single-Molecule Charge Transport: A Case Study of Oligoynes with Pyridine Anchor Groups. *Phys. Status Solidi Basic Res.* **2013**, *250* (11), 2452–2457.

(58) Milan, D. C.; Al-Owaedi, O. A.; Oerthel, M. C.; Marqués-González, S.; Brooke, R. J.; Bryce, M. R.; Cea, P.; Ferrer, J.; Higgins, S. J.; Lambert, C. J.; et al. Solvent Dependence of the Single Molecule Conductance of Oligoyne-Based Molecular Wires. *J. Phys. Chem. C* **2016**, *120* (29), 15666–15674.

(59) Milan, D. C.; Krempe, M.; Ismael, A. K.; Movsisyan, L. D.; Franz, M.; Grace, I.; Brooke, R. J.; Schwarzacher, W.; Higgins, S. J.; Anderson, H. L.; et al. The Single-Molecule Electrical Conductance of a Rotaxane-Hexayne Supramolecular Assembly. *Nanoscale* **2017**, *9* (1), 355–361.

(60) Moneo, A.; González-Orive, A.; Bock, S.; Fenero, M.; Herrer, I. L.; Milan, D. C.; Lorenzoni, M.; Nichols, R. J.; Cea, P.; Perez-Murano, F.; et al. Towards Molecular Electronic Devices Based on 'all-Carbon'' Wires.' *Nanoscale* **2018**, *10* (29), 14128–14138.

(61) Szafert, S.; Gladysz, J. A. Carbon in One Dimension: Structural Analysis of the Higher Conjugated Polyynes. *Chem. Rev.* **2006**, *106* (11), PR1-PR33.

(62) Gibtner, T.; Hampel, F.; Gisselbrecht, J.-P.; Hirsch, A. End-Cap Stabilized Oligoynes : Model Compounds for the Linear Sp Carbon Allotrope Carbyne. *Chem. - A Eur. J.* **2002**, No. 2, 408–432.

(63) Morisaki, Y.; Luu, T.; Tykwinski, R. R. A One-Pot Synthesis and Functionalization of Polyynes. *Org. Lett.* **2006**, *8* (4), 689–692.

(64) Hirsch, A. The Era of Carbon Allotropes. *Nat. Mater.* **2010**, *9* (11), 868–871.

(65) Casari, C. S.; Tommasini, M.; Tykwinski, R. R.; Milani, A. Carbon-Atom Wires: 1-D Systems with Tunable Properties. *Nanoscale* **2016**, *8* (8), 4414–4435.

(66) Haley, M.; Tykwinski, R. R. *Carbon-Rich Compounds: From*

Molecules to Materials; Wiley-VCH: Weinheim, 2006.

(67) Diederich, F.; Stang, P. J.; Tykwinski, R. R. *Acetylene Chemistry: Chemistry, Biology and Material Science*; Wiley-VCH: Weinheim, 2005.

(68) Itzhaki, L.; Rozental, E.; Altus, E.; Basch, H.; Hoz, S. Conjugation in Polyyne Rods: To What Extent Is Charge Delocalization Coupled to Geometrical Changes? *J. Phys. Chem. A* **2008**, *112* (50), 12812–12815.

(69) Al-Backri, A.; Zólyomi, V.; Lambert, C. J. Electronic Properties of Linear Carbon Chains: Resolving the Controversy. *J. Chem. Phys.* **2014**, *140* (10), 104306.

(70) Crljen, Ž.; Baranović, G. Unusual Conductance of Polyyne-Based Molecular Wires. *Phys. Rev. Lett.* **2007**, *98* (11), 116801.

(71) Wang, C.; Batsanov, A. S.; West, K.; Bryce, M. R. Synthesis and Crystal Structures of Isolable Terminal Aryl Hexatriyne and Octatetrayne Derivatives. *Org. Lett.* **2008**, *10* (14), 3069–3072.

(72) West, K.; Wang, C.; Batsanov, A. S.; Bryce, M. R. Are Terminal Aryl Butadiynes Stable? Synthesis and X-Ray Crystal Structures of a Series of Aryl- and Heteroaryl-Butadiynes (Ar-C≡C-C≡C-H). *J. Org. Chem.* **2006**, *71* (22), 8541–8544.

(73) Chalifoux, W. A.; Tykwinski, R. R. Synthesis of Polyynes to Model the Sp-Carbon Allotrope Carbyne. *Nat. Chem.* **2010**, *2* (11), 967–971.

(74) Johnson, T. R.; Walton, D. R. M. Silylation as a Protective Method in Acetylene Synthesis. *Tetrahedron* **1972**, *28*, 5221–5236.

(75) Jevric, M.; Nielsen, M. B. Synthetic Strategies for Oligoynes. *Asian J. Org. Chem.* **2015**, *4* (4), 286–295.

(76) Sugiyama, J.; Tomita, I. Novel Approach to Stabilize Unstable Molecular Wires by Simultaneous Rotaxane Formation - Synthesis of Inclusion Complexes of Oligocarbynes with Cyclic Host Molecules. *European J. Org. Chem.* **2007**, No. 28, 4651–4653.

(77) Movsisyan, L. D.; Kondratuk, D. V.; Franz, M.; Thompson, A. L.; Tykwinski, R. R.; Anderson, H. L. Synthesis of Polyyne Rotaxanes. *Org. Lett.* **2012**, *14* (13), 3424–3426.

(78) Weisbach, N.; Baranová, Z.; Gauthier, S.; Reibenspies, J. H.; Gladysz, J. A. A New Type of Insulated Molecular Wire: A Rotaxane Derived from a Metal-Capped Conjugated Tetrayne. *Chem. Commun.* **2012**, *48* (61), 7562–7564.

(79) Schrettl, S.; Contal, E.; Hoheisel, T. N.; Fritzsche, M.; Balog, S.; Szilluweit, R.; Frauenrath, H. Facile Synthesis of Oligoyne Amphiphiles and Their Rotaxanes. *Chem. Sci.* **2015**, *6* (1), 564–574.

(80) Li, J.; Grimsdale, A. C. Carbazole-Based Polymersfor Organic Photovoltaic Devices. *Chem. Soc. Rev.* **2010**, *39* (7), 2399–2410.

(81) Klinger, C.; Vostrowsky, O.; Hirsch, A. Synthesis of Alkylene-Bridged Diphenyl-Oligoynes. *European J. Org. Chem.* **2006**, No. 6, 1508–1524.

(82) These side-reactions can occur with unsubstituted carbazole, especially at the cation radical stage.

(83) Hughes, G.; Bryce, M. R. Electron-Transporting Materials for Organic Electroluminescent and Electrophosphorescent Devices. *J. Mater. Chem.* **2005**, *15*, 94–107.

(84) Schulz, B.; Bruma, M.; Brehmer, L. Aromatic Poly (1,3,4-Oxadiazole)s as Advanced Materials. *Adv. Mater.* **1997**, *9* (8), 601–613.

(85) Prato, M.; Maggini, M. Fulleropyrrolidines: A Family of Full-Fledged Fullerene Derivatives. *Acc. Chem. Res.* **1998**, *31* (9), 519–526.

(86) There are reports of an explosion during the synthesis of analogous carbon-rich compounds. Armitage, J. B.; Entwistle, N.; Jones, E. R. H.; Whiting, M. C. J. Chem. Soc. 1954, 147-154. See also: Chem. Eng. News 2010, 88(3), 2: http://cen.acs.org/articles/88/i3/Chemical-Safety-Trimethylsilylacetylene-Explosion.html

(87) Wu, X.; Wang, L.; Hua, Y.; Wang, C.; Batsanov, A. S.; Bryce, M. R. A Carbazole - Oxadiazole Diad Molecule for Single-Emitting- Component White Organic Light-Emitting Devices (WOLEDs). *Tetrahedron* **2014**, *70* (11), 2015–2019.

(88) Milani, A.; Barbieri, V.; Facibeni, A.; Russo, V.; Li Bassi, A.; Lucotti, A.; Tommasini, M.; Tzirakis, M. D.; Diederich, F.; Casari, C. S. Structure Modulated Charge Transfer in Carbon Atomic Wires. *Sci. Rep.* **2019**, *9* (1), 1–10.

(89) Yanai, T.; Tew, D. P.; Handy, N. C. A New Hybrid Exchange-Correlation Functional Using the Coulomb-Attenuating Method (CAM-B3LYP). *Chem. Phys. Lett.* **2004**, *393* (1–3), 51–57.

(90) Peterson, K. A.; Woon, D. E.; Dunning, T. H. Benchmark Calculations with Correlated Molecular Wave Functions. IV. The Classical Barrier Height of the H+H2→H2+H Reaction. *J. Chem. Phys.* **1994**, *100* (10), 7410–7415.

(91) Woon, D. E.; Dunning, T. H. Gaussian Basis Sets for Use in Correlated Molecular Calculations. III. The Atoms Aluminum through Argon. *J. Chem. Phys.* **1993**, *98* (2), 1358–1371.

(92) Kendall, R. A.; Dunning, T. H.; Harrison, R. J. Electron Affinities of the First-Row Atoms Revisited. Systematic Basis Sets and Wave Functions. *J. Chem. Phys.* **1992**, *96* (9), 6796–6806.

(93) Dunning, T. H. Gaussian Basis Sets for Use in Correlated Molecular Calculations. I. The Atoms Boron through Neon and Hydrogen. *J. Chem. Phys.* **1989**, *90* (2), 1007–1023.

(94) Tomasi, J.; Mennucci, B.; Cammi, R. Quantum Mechanical Continuum Solvation Models. *Chem. Rev.* **2005**, *105* (8), 2999–3094.

(95) Chai, J. Da; Head-Gordon, M. Long-Range Corrected Hybrid Density Functionals with Damped Atom-Atom Dispersion Corrections. *Phys. Chem. Chem. Phys.* **2008**, *10* (44), 6615–6620.

(96) Henderson, T. M.; Izmaylov, A. F.; Scalmani, G.; Scuseria, G. E. Can Short-Range Hybrids Describe Long-Range-Dependent Properties? *J. Chem. Phys.* **2009**, *131* (4), 044108.

(97) Zhao, Y.; Truhlar, D. G. The M06 Suite of Density Functionals for Main Group Thermochemistry, Thermochemical Kinetics, Noncovalent Interactions, Excited States, and Transition Elements: Two New Functionals and Systematic Testing of Four M06-Class Functionals and 12 Other Function. *Theor. Chem. Acc.* **2008**, *120* (1–3), 215–241.

(98) Zhao, Y.; Truhlar, D. G. Density Functional for Spectroscopy: No Long-Range Self-Interaction Error, Good Performance for Rydberg and Charge-Transfer States, and Better Performance on Average than B3LYP for Ground States. *J. Phys. Chem. A* **2006**, *110* (49), 13126–13130.

(99) Becke, A. D. Density-Functional Thermochemistry. III. The Role of Exact Exchange. *J. Chem. Phys.* **1993**, *98* (7), 5648–5652.

(100) Bloino, J.; Baiardi, A.; Biczysko, M. Aiming at an Accurate Prediction of Vibrational and Electronic Spectra for Medium-to-Large Molecules: An Overview. *Int. J. Quantum Chem.* **2016**, *116* (21), 1543–1574.

(101) Santoro, F.; Lami, A.; Improta, R.; Bloino, J.; Barone, V. Effective Method for the Computation of Optical Spectra of Large Molecules at Finite Temperature Including the Duschinsky and Herzberg-Teller Effect: The Qx Band of Porphyrin as a Case Study. *J. Chem. Phys.* **2008**, *128* (22), 224311.

(102) Barone, V.; Bloino, J.; Biczysko, M.; Santoro, F. Fully Integrated Approach to Compute Vibrationally Resolved Optical Spectra : From Small Molecules To. *J. Chem. Theory Comput.* **2009**, *5*, 540–554.

(103) Bloino, J.; Biczysko, M.; Santoro, F.; Barone, V. General Approach to Compute Vibrationally Resolved One-Photon Electronic Spectra. *J. Chem. Theory Comput.* **2010**, *6* (4), 1256–1274.

(104) Baiardi, A.; Bloino, J.; Barone, V. General Time Dependent Approach to Vibronic Spectroscopy Including Franck-Condon, Herzberg-Teller, and Duschinsky Effects. *J. Chem. Theory Comput.* **2013**, *9* (9), 4097–4115.

(105) Mullen, K. M.; van Stokkum, I. H. M. TIMP: An R Package for Modeling Multi-Way Spectroscopic Measurements. *J. Stat. Softw.* **2007**, *18* (3), 1–46.

(106) Seger, R.; Mullen, K. M. Glotaran : A Java -Based Graphical User Interface for the R Package TIMP. *J. Stat. Softw.* **2012**, *49* (3), 1–22.

(107) Benten, H.; Jiamo, G.; Ohkita, H.; Ito, S.; Yamamoto, M.;

Sakumoto, N.; Hori, K.; Tohda, Y.; Tani, K. Intramolecular Singlet and Triplet Excimers of Triply Bridged [3.3.n](3,6,9)Carbazolophanes. *J. Phys. Chem. B* **2007**, *111* (37), 10905–10914.

(108) Turro, N. J.; Ramamurthy, V.; Scaiano, J. C. *Modern Molecular Photochemistry of Organic Molecules*; University Science Books: Sausalito, California, 2010.

(109) Mentel, K. K.; Nunes, R. M. D.; Serpa, C.; Arnaut, L. G. Dynamics of Radical Ion Pairs Following Photoinduced Electron Transfer in Solvents with Low and Intermediate Polarities. *J. Phys. Chem. B* **2015**, *119* (24), 7571–7578.

(110) The measurements were performed in benzonitrile in-stead of DMF, due to the instability of the molecules in the latter at higher temperatures.

(111) Weiss, E. A.; Ahrens, M. J.; Sinks, L. E.; Gusev, A. V; Ratner, M. A.; Wasielewski, M. R. Making a Molecular Wire: Charge and Spin Transport Through. *J. Am. Chem. Soc.* **2004**, No. 12, 5577–5584.

(112) Goldsmith, R. H.; Sinks, L. E.; Kelley, R. F.; Betzen, L. J.; Liu, W.; Weiss, E. A.; Ratner, M. A.; Wasielewski, M. R. Wire-like Charge Transport at near Constant Bridge Energy through Fluorene Oligomers. *Proc. Natl. Acad. Sci.* **2005**, *102* (10), 3540–3545.

(113) Kuss-Petermann, M.; Wenger, O. S. Unusual Distance Dependences of Electron Transfer Rates. *Phys. Chem. Chem. Phys.* **2016**, *18* (28), 18657–18664.

(114) Kuss-Petermann, M.; Wenger, O. S. Electron Transfer Rate Maxima at Large Donor-Acceptor Distances. *J. Am. Chem. Soc.* **2016**, *138* (4), 1349–1358.

(115) Kuss-Petermann, M.; Wenger, O. S. Increasing Electron-Transfer Rates with Increasing Donor-Acceptor Distance. *Angew. Chemie - Int. Ed.* **2016**, *55* (2), 815–819.

(116) Leturcq, R.; Stampfer, C.; Inderbitzin, K.; Durrer, L.; Hierold, C.; Mariani, E.; Schultz, M. G.; von Oppen, F.; Ensslin, K. Franck–Condon Blockade in Suspended Carbon Nanotube Quantum Dots. *Nat. Phys.* **2009**, *5* (5), 327–331.

(117) Freeman, D. M. E.; Musser, A. J.; Frost, J. M.; Stern, H. L.; Forster, A. K.; Fallon, K. J.; Rapidis, A. G.; Cacialli, F.; McCulloch, I.; Clarke, T. M.; et al. Synthesis and Exciton Dynamics of Donor-Orthogonal Acceptor Conjugated Polymers: Reducing the Singlet-Triplet Energy Gap. *J. Am. Chem. Soc.* **2017**, *139* (32), 11073–11080.

(118) Etherington, M. K.; Gibson, J.; Higginbotham, H. F.; Penfold, T. J.; Monkman, A. P. Revealing the Spin-Vibronic Coupling Mechanism of Thermally Activated Delayed Fluorescence. *Nat. Commun.* **2016**, *7*, 1–7.

(119) Gibson, J.; Monkman, A. P.; Penfold, T. J. The Importance of Vibronic Coupling for Efficient Reverse Intersystem Crossing in Thermally Activated Delayed Fluorescence Molecules. *ChemPhysChem* **2016**, *17* (1), 2956–2961.

(120) Samanta, P. K.; Kim, D.; Coropceanu, V.; Brédas, J. L. Up-Conversion Intersystem Crossing Rates in Organic Emitters for Thermally Activated Delayed Fluorescence: Impact of the Nature of Singlet vs Triplet Excited States. *J. Am. Chem. Soc.* **2017**, *139* (11), 4042–4051.

(121) Noda, H.; Chen, X. K.; Nakanotani, H.; Hosokai, T.; Miyajima, M.; Notsuka, N.; Kashima, Y.; Brédas, J. L.; Adachi, C. Critical Role of Intermediate Electronic States for Spin-Flip Processes in Charge-Transfer-Type Organic Molecules with Multiple Donors and Acceptors. *Nat. Mater.* **2019**, *18* (10), 1084–1090.

Supporting Information

Molecular synthesis. All reactions were conducted under a blanket of argon which was dried by passage through a column of phosphorus pentoxide unless otherwise stated. All commercial chemicals were used without further purification. Anhydrous solvents were dried through an HPLC column on an Innovative Technology Inc. solvent purification system. Column chromatography was carried out using 40-60 µm mesh silica (Fluorochem). NMR spectra were recorded on Bruker Avance-400, Varian Inova 500, Varian VNMRS-600 and 700 spectrometers. Chemical shifts are reported in ppm relative to tetramethylsilane (0.00 ppm) or the residual solvent signal. Melting points were determined in open-ended capillaries using a Stuart Scientific SMP40 melting point apparatus at a ramping rate of 2 °C/min. Mass spectra were measured on a Waters Xevo OTofMS with an ASAP probe.

Caution: Great care should be taken when handling oligoynes and their intermediates in bulk quantities, due to their potential explosive instability. Melting/decomposition temperatures for **1-4** and **7** were >150 ^{o}C: they were not heated above this temperature.

Intermediate compounds **A**,[1] **B**,[2] **C**,[1] **D**[3] and **E**[4] were synthesized by literature procedures.

Synthesis of 1.

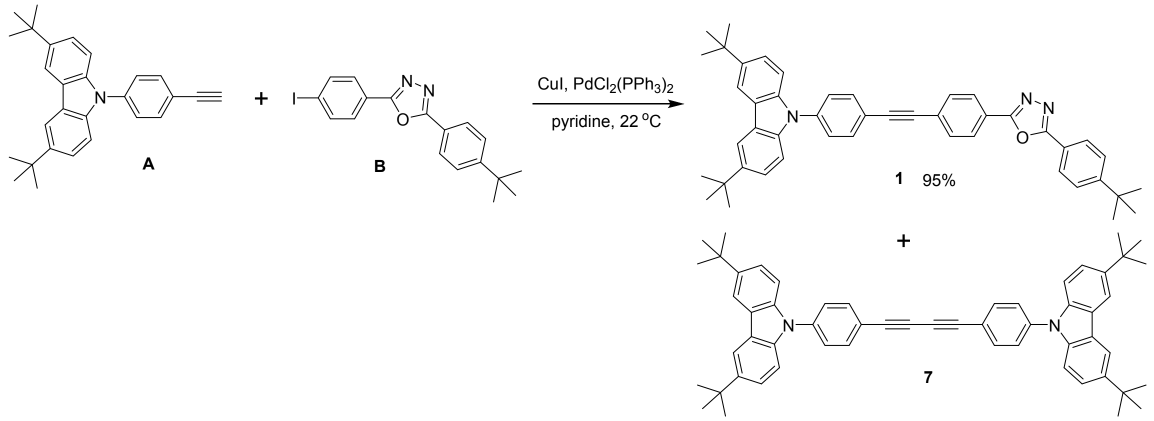

A solution of compound **A** (0.202 g, 0.5 mmol) and compound **B** (0.280 g, 0.738 mmol) in pyridine (20 ml) was degassed by bubbling argon for 30 min. $PdCl_2(PPh_3)_2$ (17.5 mg) and CuI (6.0 mg) were added to the solution as solids. The mixture was stirred at 22 °C for 16 h under Ar to yield a pale-yellow suspension. The solvent was removed by vacuum evaporation. The residual yellow solid was chromatographed eluting initially with hexane-DCM (3:1 v/v) to give the oxidative dimer of **A**, compound **7** as an off-white solid (84 mg). The column was then eluted with DCM-diethyl ether (9:1 v/v) to give compound **1** (0.31 g, 95%) as off-white crystals after a subsequent recrystallization from chloroform-ethanol.

Compound **7**: ^{1}H NMR (400 MHz, Chloroform-*d*) δ 8.15 (dd, *J* = 2.0, 0.6 Hz, 4H), 7.82 – 7.72 (m, 4H), 7.59 (d, *J* = 8.7 Hz, 4H), 7.49 (dd, *J* = 8.7, 1.9 Hz, 4H), 7.41 (dd, *J* = 8.6, 0.6 Hz, 4H), 1.48 (s, 36H). ^{13}C NMR (101 MHz, $CDCl_3$) δ 143.44, 139.16, 138.72, 134.00, 126.34, 123.79, 123.74, 119.87, 116.35, 109.22, 81.45, 74.62, 34.76, 31.99. HR-MS (ASAP+) *m/z* calcd for $C_{56}H_{56}N_2$ $[M]^+$ 756.4443, found *m/z*: $[M]^+$ 756.4447. Anal. Calcd. for $C_{56}H_{56}N_2$: C 88.84; H 7.46; N 3.70%. Found: C 88.77; H 7.52; N 3.57%.

Compound **1**: ^{1}H NMR (400 MHz, Chloroform-*d*) δ 8.20 – 8.15 (m, 4H), 8.12 – 8.07 (m, 2H), 7.78 (d, *J* = 8.5 Hz, 2H), 7.76 – 7.72 (m, 2H), 7.64 – 7.55 (m, 4H), 7.49 (dd, *J* = 8.7, 1.9 Hz, 2H), 7.42 (dd, *J* = 8.5, 0.6 Hz, 2H), 1.48 (s, 18H), 1.39 (s, 9H). ^{13}C NMR (101 MHz, $CDCl_3$) δ 163.94, 155.52, 143.32, 138.83, 138.65, 133.18, 132.22, 126.85, 126.84, 126.54, 126.41, 126.10, 123.76, 123.68, 123.57, 121.02, 120.99, 116.33, 109.21, 91.77, 89.34, 35.13, 34.77, 32.01, 31.14. HR-MS (ASAP+) *m/z* calcd for $C_{46}H_{45}N_3O$ $[M]^+$ 655.3563, found *m/z*: $[M]^+$ 655.3562. Anal. Calcd. for $C_{46}H_{45}N_3O$: C 84.24; H 6.92; N 6.41%. Found C 84.24; H 6.89; N 6.31%.

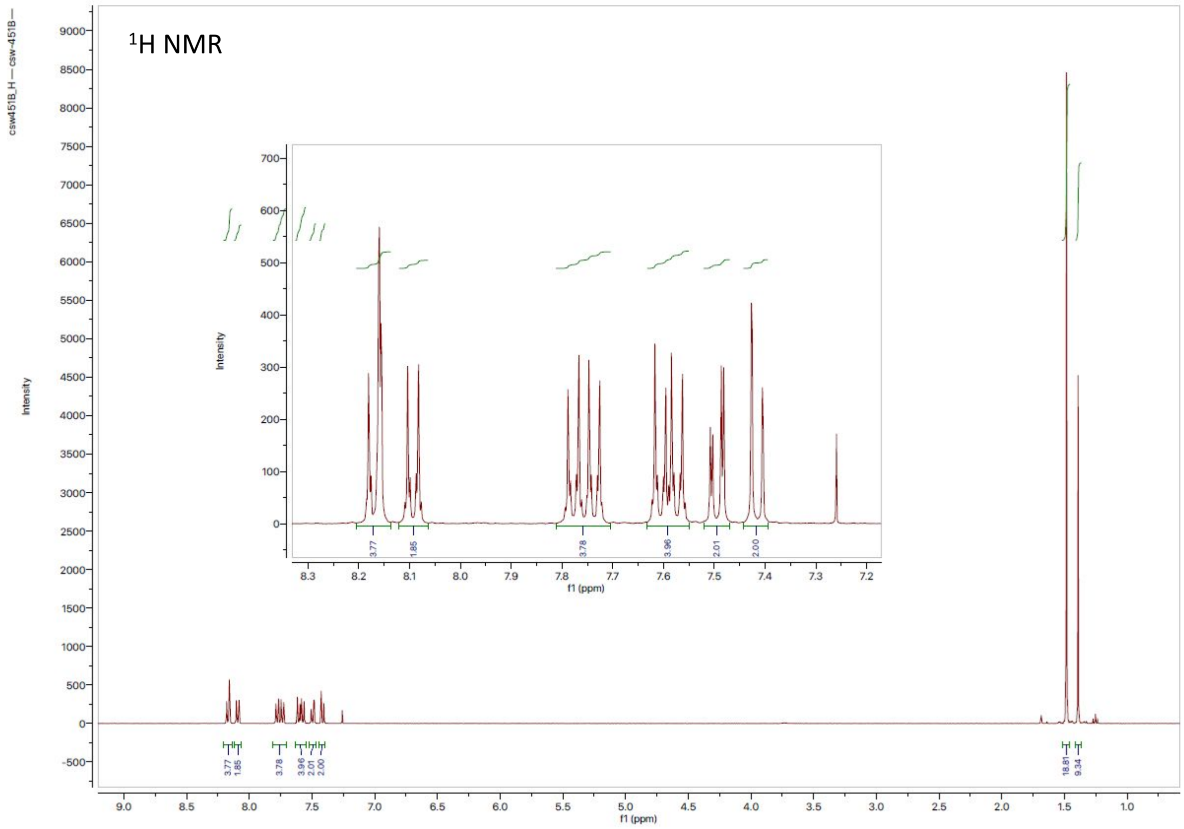

^{1}H NMR
csw451B_H — csw-451B —
Intensity
9000
8500
8000
7500
7000
6500
6000
5500
5000
4500
4000
3500
3000
2500
2000
1500
1000
500
0
-500
3.77
1.85
3.78
3.96
2.01
2.00
18.81
9.34
9.0
8.5
8.0
7.5
7.0
6.5
6.0
5.5
5.0
4.5
4.0
3.5
3.0
2.5
2.0
1.5
1.0
f1 (ppm)
Intensity
700
600
500
400
300
200
100
0
3.77
1.85
3.78
3.96
2.01
2.00
8.3
8.2
8.1
8.0
7.9
7.8
7.7
7.6
7.5
7.4
7.3
7.2
f1 (ppm)

Synthesis of 3.

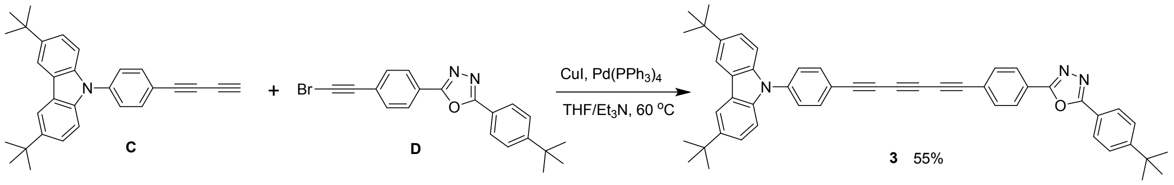

To a solution of **C** (100 mg, 0.248 mmol) and **D** (113 mg, 1.2 eq) in THF/Et$_3$N (5 ml / 5 ml), Pd(PPh$_3$)$_4$ (14 mg) and CuI (3 mg) were added. The mixture was stirred at 60 °C under argon for 19 h. The solvent was removed by vacuum evaporation and the product was purified by column chromatography using DCM-hexane (9:1 v/v) as eluent to give **3** as a yellow solid (96 mg, 55% yield). Crystals were grown by slow evaporation of a solution of **3** in DCM-ethanol. ^{1}H NMR (500 MHz, Chloroform-*d*) δ 8.15 (m, 4H), 8.09 (d, *J* = 8.4 Hz, 2H), 7.77 (d, *J* = 8.4 Hz, 2H), 7.72 (d, *J* = 8.4 Hz, 2H), 7.59 (m, 4H), 7.50 (dd, *J* = 8.7, 1.9 Hz, 2H), 7.42 (d, *J* = 8.6 Hz, 2H), 1.49 (s, 18H), 1.41 (s, 9H). ^{13}C NMR (126 MHz, Chloroform-*d*) δ 165.25, 163.86, 155.88, 143.79, 139.93, 138.76, 134.80, 133.81, 127.11, 127.06, 126.47, 126.38, 124.89, 124.51, 124.08, 124.03, 121.06, 118.92, 116.63, 109.45, 79.17, 77.95, 77.34, 75.20, 68.18, 66.74, 35.40, 35.02, 32.23, 31.38. HR-MS (ASAP+) *m/z* calcd for $C_{50}H_{45}N_3O$ [M]$^+$ 703.3563, found *m/z* : [M]$^+$ 703.3574. Anal. Calcd. for $C_{50}H_{45}N_3O\cdot0.5EtOH$: C, 84.26; H, 6.66; N, 5.78%. Found: C, 84.61; H, 6.36; N, 5.44%

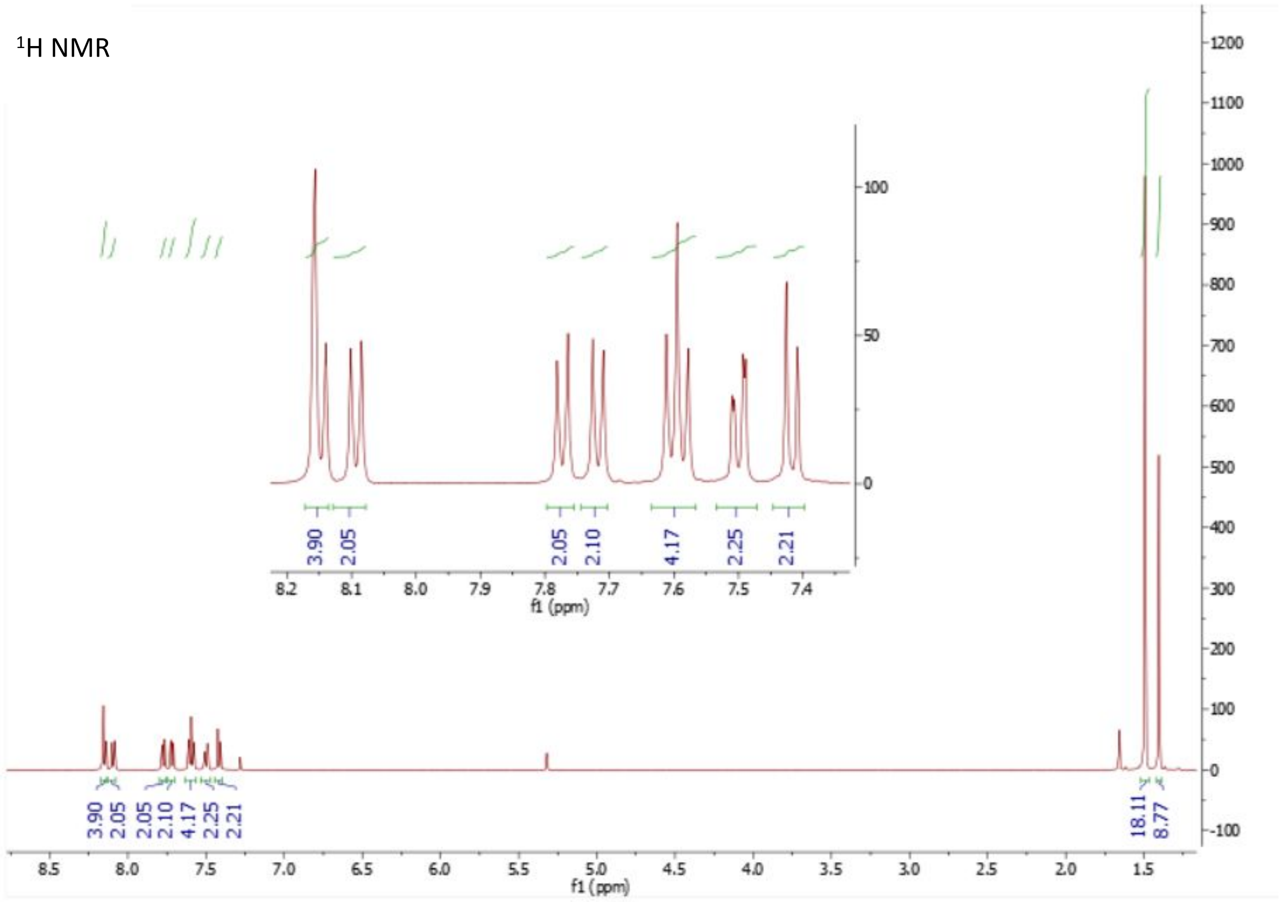

Synthesis of 4.

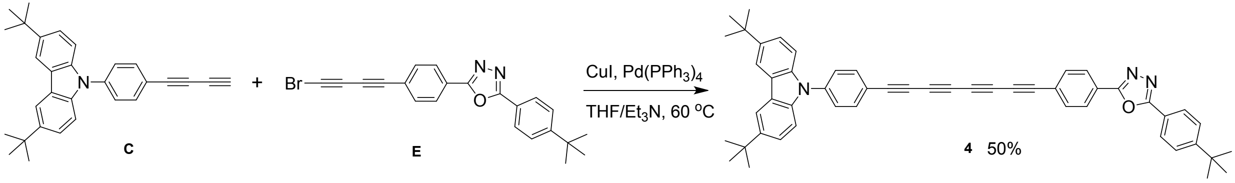

To a solution of the **C** (100 mg, 0.248 mmol) and **E** (121 mg, 1.2 eq) in THF/Et_3N (5 ml/5 ml), $Pd(PPh_3)_4$ (14 mg) and CuI (3 mg) were added. The mixture was stirred at 60 °C under argon for 22 h. The solvent was removed by vacuum evaporation and the product was purified by column chromatography using DCM-hexane (4:1 v/v) to give **4** as a yellow solid (90 mg, 50% yield). Crystals were grown by slow evaporation of a solution of **4** in DCM-methanol. ^1H NMR (500 MHz, CD_2Cl_2) δ 8.18 (m, 4H), 8.10 (d, J = 8.4 Hz, 2H), 7.83 (d, J = 8.4 Hz, 2H), 7.77 (d, J = 8.4 Hz, 2H), 7.64 (dd, J = 11.2, 8.4 Hz, 4H), 7.53 (dd, J = 8.7, 1.9 Hz, 2H), 7.45 (d, J = 8.7 Hz, 2H), 1.49 (s, 18H), 1.42 (s, 9H). ^{13}C NMR (176 MHz, CD_2Cl_2) δ 165.01, 163.52, 155.69, 143.64, 140.00, 138.44, 134.79, 133.80, 126.73, 126.65, 126.20, 126.15, 125.14, 123.83, 123.72, 123.46, 120.86, 117.91, 116.37, 109.16, 77.83, 76.80, 76.36, 74.43, 68.09, 67.00, 64.24, 63.30, 34.99, 34.61, 31.63, 30.79. HR-MS (ASAP+) *m/z* calcd for $C_{52}H_{45}N_3O$ $[M]^+$ 727.3563, found *m/z* : $[M]^+$ 727.3546. Anal. Calcd. for $C_{52}H_{45}N_3O{\cdot}0.5MeOH$: C, 84.76; H, 6.37; N, 5.65. Found: C, 85.12; H, 6.15; N, 5.32.

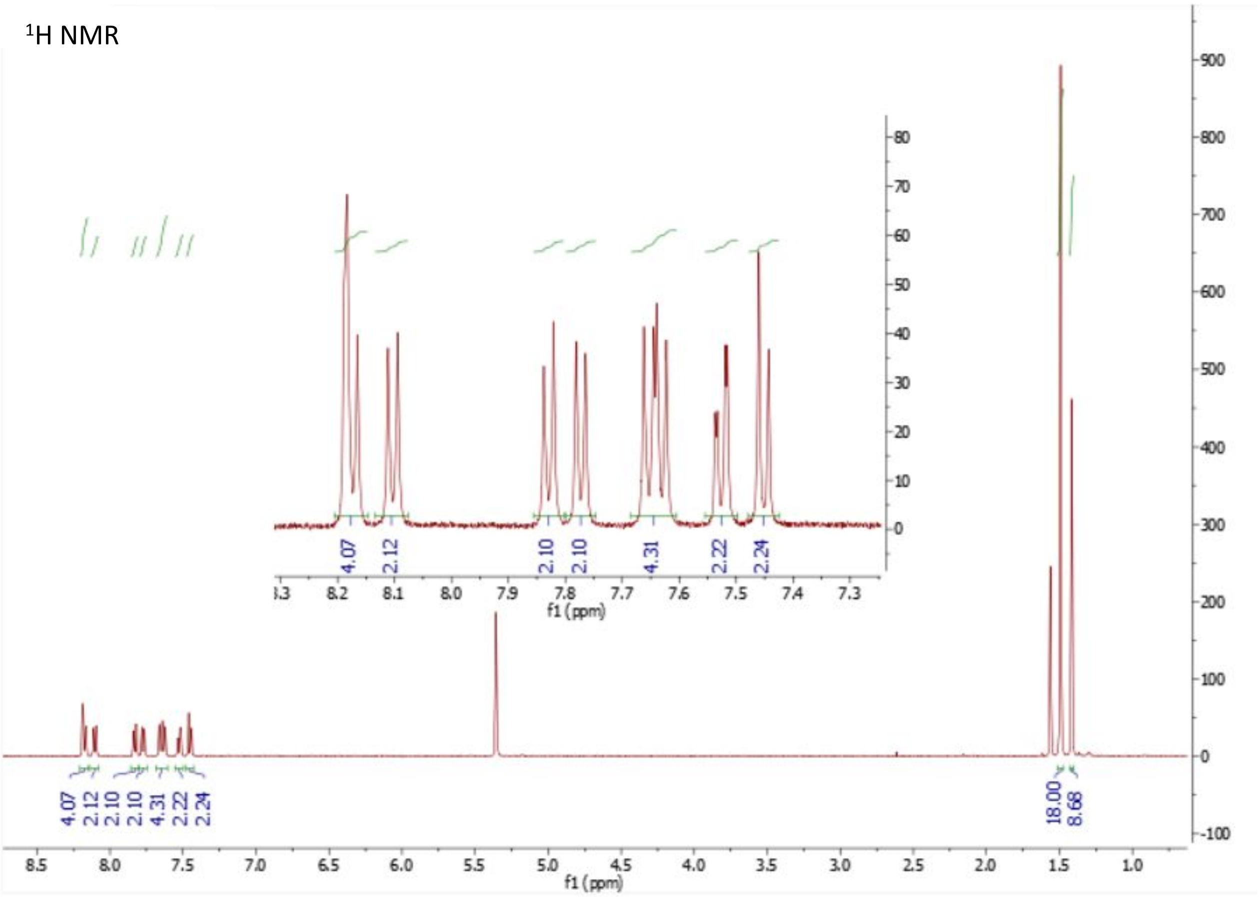

X-Ray Crystallography

Diffraction experiments were carried out for **3**·½EtOH and **4**·EtOH on a Bruker 3-circle diffractometer with a SMART 6000 CCD area detector, using graphite-monochromated Mo-K_α radiation from a sealed tube. For **4**·2MeOH on a Bruker D8 Venture 3-circle diffractometer with a PHOTON 100 CMOS area detector using Cu-K_α radiation from IµS microsource with focusing mirrors. The crystals were cooled using a Cryostream (Oxford Cryosystems) open-flow N_2 cryostat. The structures were solved by direct methods using SHELXS software[5] and refined by full-matrix least squares against F^2 of all reflections, using SHELXL program (version 2014/7)[6] on OLEX2 platform[7]. The chaotically disordered solvent of crystallization could not be modeled; the final refinement was carried out against the data corrected using solvent-masking procedure (OLEX2 SMTBX program) based on the Bypass algorithm.[8,9]

Table S1. Crystal data.

	3·½EtOH	**4**·EtOH	**4**·2MeOH
CCDC deposition no.	945614	945615	1823328
Formula	$C_{50}H_{45}N_3O·½C_2H_6O$	$C_{52}H_{45}N_3O·C_2H_6O$	$C_{52}H_{45}N_3O·2CH_4O$
F.w.	726.92	773.97	791.99
T, K	120	120	131
λ, Å	0.71073	0.71073	1.54184
µ, mm^{-1}	0.07	0.07	0.58
Symmetry	monoclinic	monoclinic	monoclinic
Space group	C2/c (no. 15)	P2/c (no. 13)	P2/c (no. 13)
a, Å	56.9412(17)	29.649(3)	29.7266(8)
b, Å	5.7064(1)	5.6349(5)	5.6315(2)
c, Å	26.1782(7)	26.194(2)	26.3407(7)
β, °	100.7546(9)	99.449(3)	99.628(1)
V, Å^3	8356.6(11)	4316.9(7)	4347.5(2)
Z	8	4	4
Density, g cm^{-3}	1.156	1.191	1.210
$2\theta_{max}$, °	55	50	151
Measured reflections	26293	27289	52340
Unique reflections	9606	7609	8774
Reflections with I>2σ(I)	4857	1837	7381
R_{int}	14.9%	31.2%	3.6%

Refined parameters	505	514	524
Solvent-accessible volume per unit cell, Å^3	873.9 (10.5%)	500.5 (11.6%)	523.4 (12.0%)
Masked electron count/unit cell	116.9	92.6	155.1
R_1 [$I > 2\sigma(I)$], wR_2 (all data)	5.2%, 11.5%	7.8%, 15.8%	4.1%, 9.9%

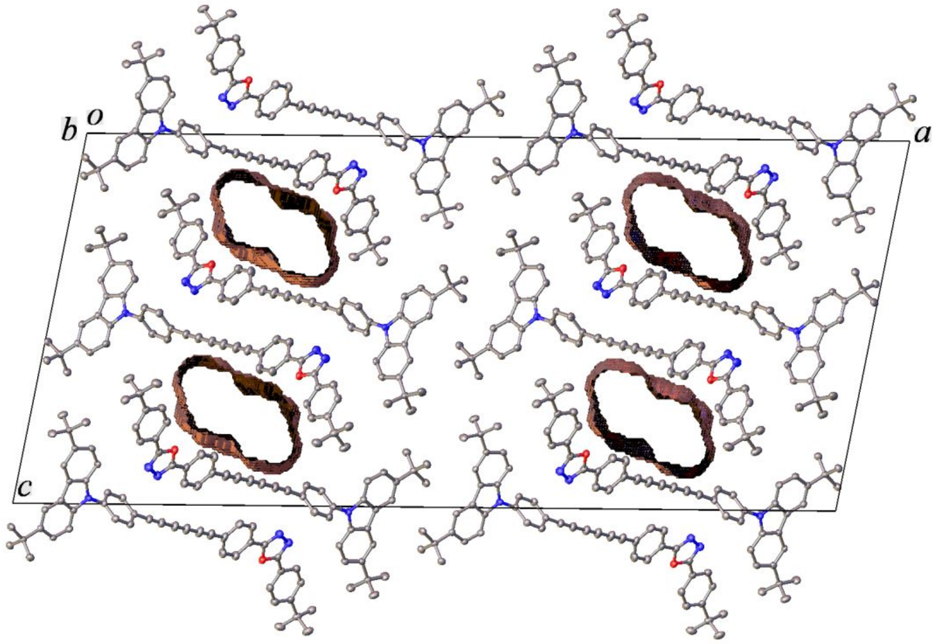

(**3**·½EtOH)

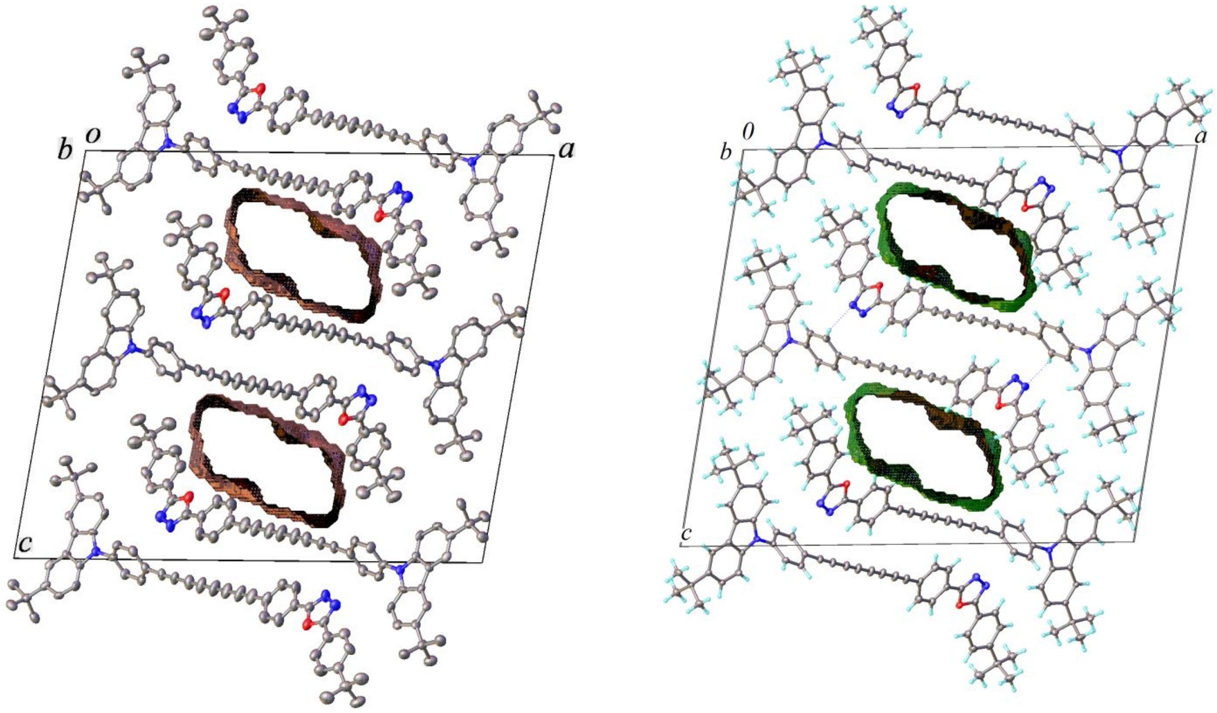

(**4**·EtOH) (**4**·2MeOH)

Figure S1. Crystal packing of **3**·½EtOH, **4**·EtOH and **4**·2MeOH, showing the boundaries of the channels containing disordered solvent (drawn using OLEX2 software).

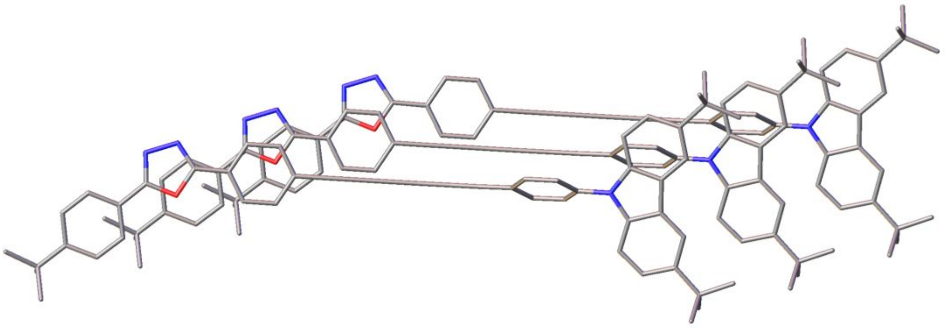

(a)

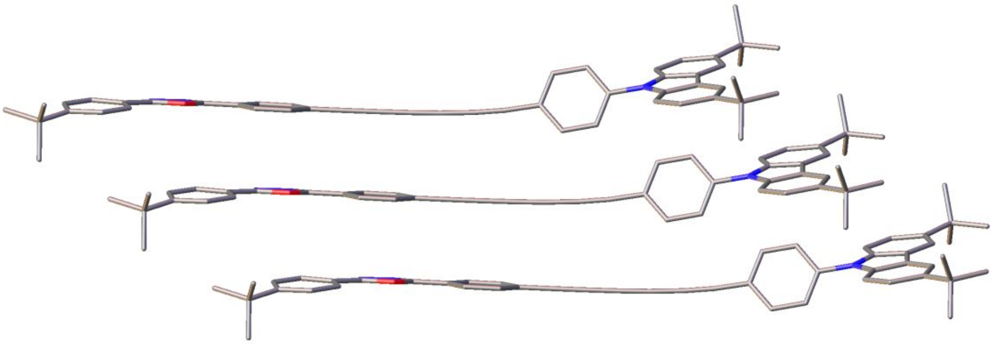

(b)

Figure S2. Stacking of **3** viewed perpendicular (a) and parallel (b) to the oxadiazole plane.

Photophysical investigation.

All solvents used were of spectroscopic grade (99.5%) and were purchased from Sigma Aldrich.

Electrochemistry

Cyclic voltammetry and square-wave voltammetry were performed at room temperature, under argon atmosphere, and the applied potential was controlled with a µAutolab III/FRA2 potentiostat from METROHM. Current vs the applied potential was recorded by means of the software NOVA 1.10. Measurements were carried out in a homemade cell containing 0.1 M tetrabutylammonium hexafluorophosphate ($TBAPF_6$) as the supporting electrolyte. A three-electrode configuration was used with a glassy carbon working electrode (3 mm diameter), Pt wire acting as the counter electrode, and Ag/AgCl as the reference electrode. The Fc/Fc^+ redox couple was used as an internal standard.

Spectroelectrochemical measurements were performed in a homemade three neck cell with a Pt gauze and a Pt wire (working and counter electrodes respectively), using Ag wire as a pseudo-reference electrode. All the experiments were carried out in dichloromethane under argon atmosphere with 0.2 M tetrabutylammonium hexafluorophosphate ($TBAPF_6$) as the supporting electrolyte.

Absorption and emission spectroscopy

UV/Vis spectra were recorded at room temperature using a Perkin Elmer Lambda 2 spectrometer. The data were collected with the software UV WinLab using a slit width of 2 nm and a scan rate of 480 nm/min. Steady-state fluorescence studies were carried out with a FlouroMax®-3 (Horiba Scientific). The quantum yields (QYs) were determined using the comparative method, which involved the use of well characterized standard references: POPOP, Coumarin 47, and Coumarin 102.

Time-resolved fluorescence studies

Fluorescence lifetimes were determined through the time-correlated single photon counting (TCSPC) technique using a Fluorolog 3 (Horiba Jobin Yvon). The sample was excited with a NanoLED-405 from Horiba with excitation wavelength 387 nm, and the signal was detected by a Hamamatsu MCP photomultiplier (type R3809U-50). All measurements were conducted in cuvettes under argon atmosphere. The time profiles were recorded for **1-4** at 380, 400, 450, and 550 nm, depending on the solvent. The fluorescence lifetimes were best fitted by a single or a bi-exponential decay. In case of the latter, the longer component constituted a minor influence.

Transient absorption spectroscopy

Femtosecond transient absorption studies were performed using 387 nm laser pulses (1 kHz, 150 fs pulse width, energy between 200 and 300 nJ) from an amplified Ti:Sapphire fs laser system (Model CPA 2101 and 2110 Clark MXR), using transient absorption pump/probe detection systems (Helios and EOS, Ultrafast Systems). In Helios visible white light (~400−770 nm) was generated by focusing a fraction of the fundamental 775 nm output onto a 2 mm sapphire disk; for the (near) IR (780−1500 nm), a 1 cm sapphire was used. Ultrafast Systems EOS Sub-Nanosecond Transient Absorption Spectrometer was employed to measure transient absorption spectra with time delays of ∼ 1 ns to 400 μs with 1 ns time resolution. White light (∼370 to >1600 nm) was generated by a built-in photonic crystal fiber supercontinuum laser source with a fundamental of 1064 nm at 2 kHz output frequency and pulse width of approximately 1 ns. All measurements were conducted in 2 mm quartz cuvettes under argon atmosphere. Obtained data were treated with the multi-wavelength, global, and target analyses. In case of the multiwavelength analysis the kinetics were fitted either mono- or multi-exponential. Temperature-dependent measurements were performed using a copper cuvette holder with an integrated Peltier element to vary the temperature between 280 and 350 K.

Pulse radiolysis

The radiolytic reduction of **2** was conducted by electron pulse radiolysis in a N_2 saturated mixtures of 80% toluene, 10% acetone and 10 % isopropanol. The sample was irradiated with high energy electron pulses (1MeV, 15 ns FWHM) by a pulse transformer type electron accelerator (Elit – Institute of Nuclear Physics, Novosibirsk, Russia). The dose per pulse was measured by electron dosimetry[10] and a dose of 100 Gy per pulse was selected. These conditions lead to the formation of $(CH_3)_2{}^{\bullet}COH$,[11-13] which is known as a strong reducing free radical capable for the one-electron reduction of **2**.[14]

The optical detection of the transients was carried out with a detection system consisting of a pulsed (pulser MSP 05 – Müller Elektronik Optik) xenon lamp (XBO 450, Osram), a SpectraPro 500 monochromator (Acton Research Corporation), a R 9220 photomultiplier (Hamamatsu Photonics), and a 500 MHz digitizing oscilloscope (TDS 640, Tektronix).

Solution Electrochemical Studies. The redox properties of the D−B−As and their references were studied by cyclic voltammetry (CV) and square-wave voltammetry (SWV) (Figure S3). The relevant CV data are summarized in Table S2. The measurements were performed in dichloromethane with 0.1 M tetrabutylammonium hexafluorophosphate ($TBAPF_6$) as supporting electrolyte. All redox potentials are reported versus Ag/AgCl. The oxidation at 1.22 V for **1** remains nearly constant in **2**-**4** and is assigned to the one-electron oxidation of the carbazole.[84] The irreversible reductions were recorded between -1.4 and -1.85 V for all oxadiazole featuring conjugates. It should be noted that the reductions associated with the oxadiazoles in **2**-**4** were observed at less negative potentials than in **1**. As the difference between the first oxidation and the first reduction reflects the energy gap, a noteworthy trend of its substantial decrease in **1-4** series was observed.

Table S2. Electrochemical data.[a]

Compound	$E^3_{1/2,red}$	$E^2_{1/2,red}$	$E^1_{1/2,red}$	$E^1_{1/2,ox}$
1	-	-	-1.83	1.22
2	-	-	-1.75	1.22
3	-	-1.61	-1.53	1.24
4	-1.61	-1.50	-1.39	1.23

[a] Potentials in V (half-wave potentials: $E_{1/2}$); scan rate 50 mVs^{-1}. Measurements were performed in dichloromethane containing 0.1 M $TBAPF_6$ as supporting electrolyte with a glassy carbon as the working electrode, a platinum counter electrode, and Ag/AgCl as the reference electrode.

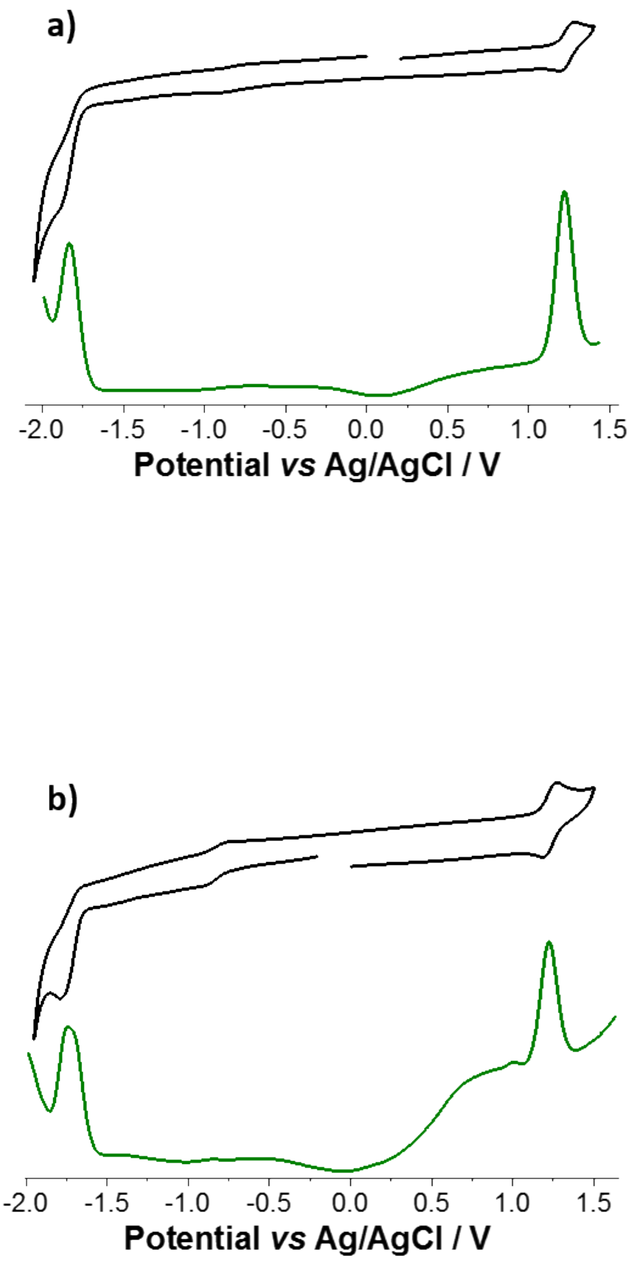
a)
-2.0
-1.5
-1.0
-0.5
0.0
0.5
1.0
1.5
Potential *vs* Ag/AgCl / V
b)
-2.0
-1.5
-1.0
-0.5
0.0
0.5
1.0
1.5
Potential *vs* Ag/AgCl / V

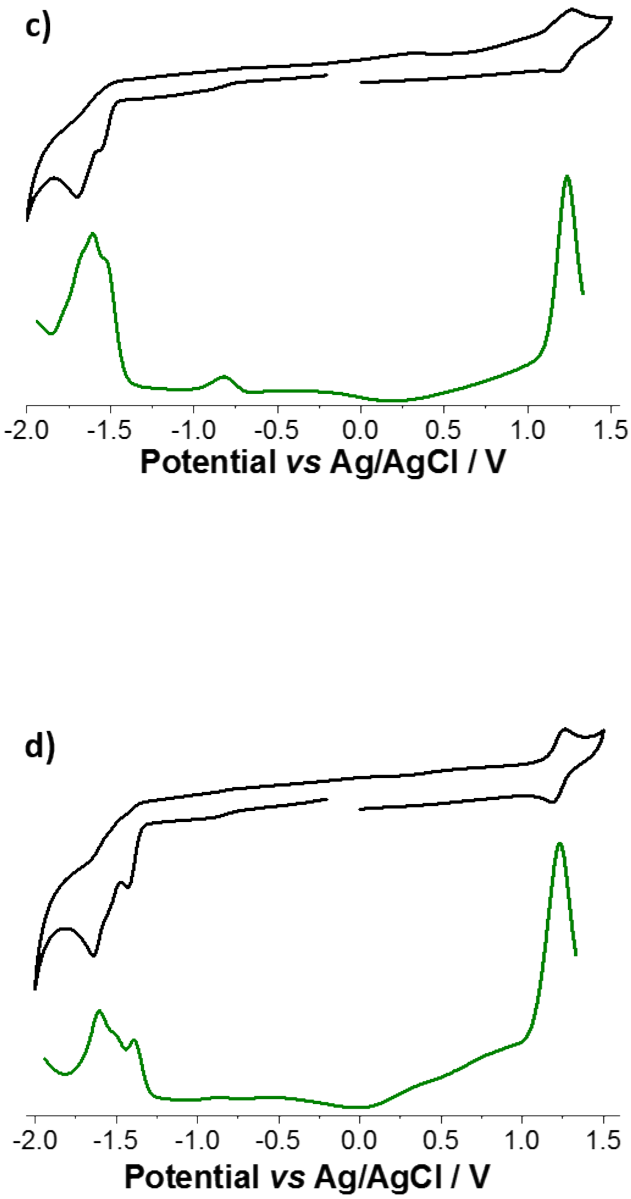

Figure S3. Cyclic (black) and square-wave (green) voltammograms of a) **1**, b) **2**, c) **3**, and d) **4**.

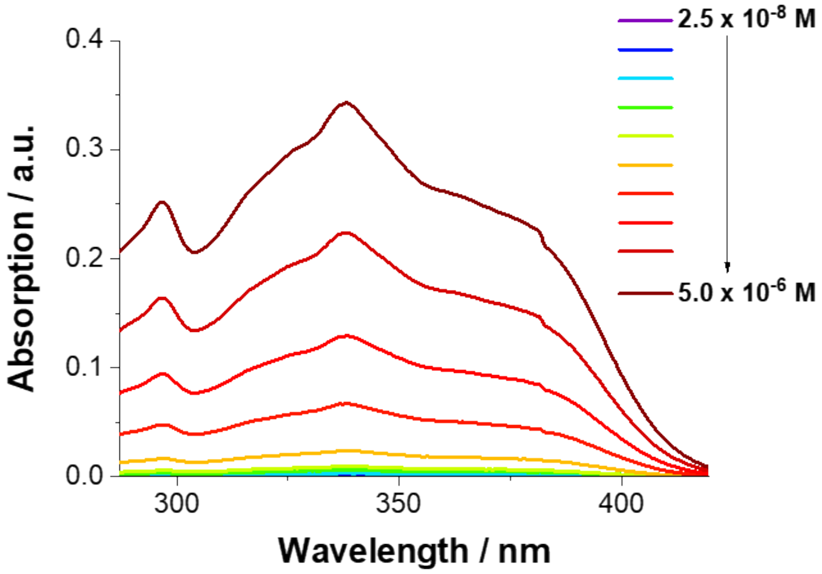

Figure S4. Concentration-dependent UV-Vis absorption spectra of **2** in DCM.

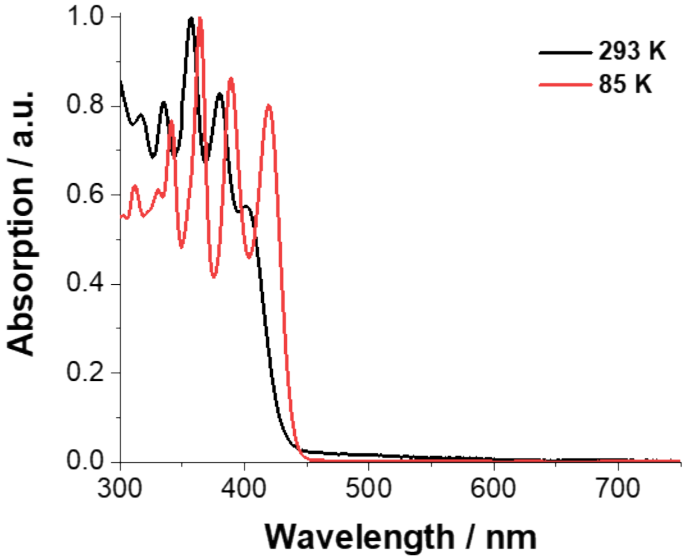

Figure S5. UV-Vis absorption spectra of **3** in 2-methyltetrahydrofuran at 85 and 293 K.

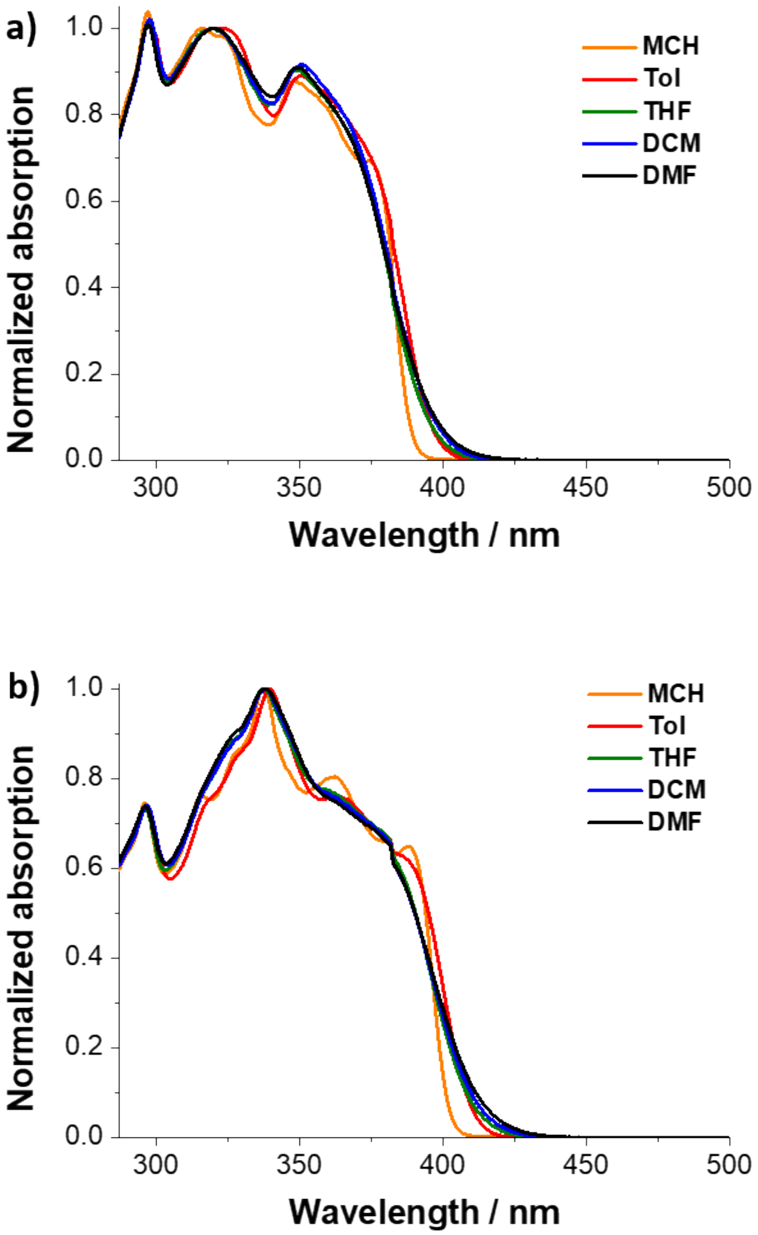
a)
Normalized absorption
0.0
0.2
0.4
0.6
0.8
1.0
Wavelength / nm
300
350
400
450
500
MCH
Tol
THF
DCM
DMF
b)
Normalized absorption
0.0
0.2
0.4
0.6
0.8
1.0
Wavelength / nm
300
350
400
450
500
MCH
Tol
THF
DCM
DMF

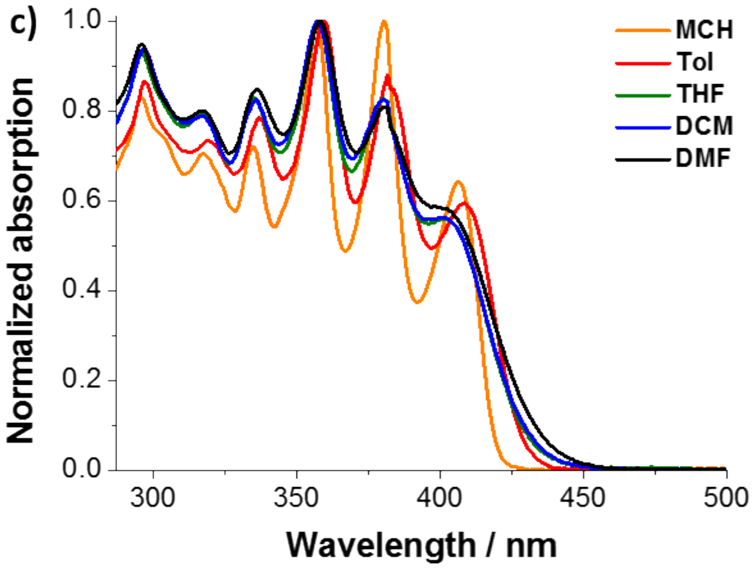

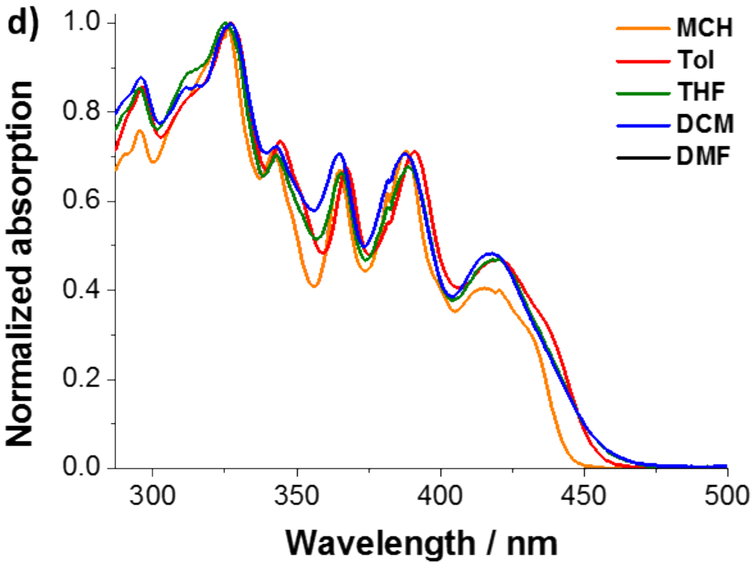

Figure S6. Normalized absorption spectra of a) **1**, b) **2**, c) **3**, and d) **4** in solvents of different polarity (MCH – methylcyclohexane, Tol – toluene, THF – tetrahydrofuran, DCM – dichloromethane, DMF – *N*,*N*–dimethylformamide).

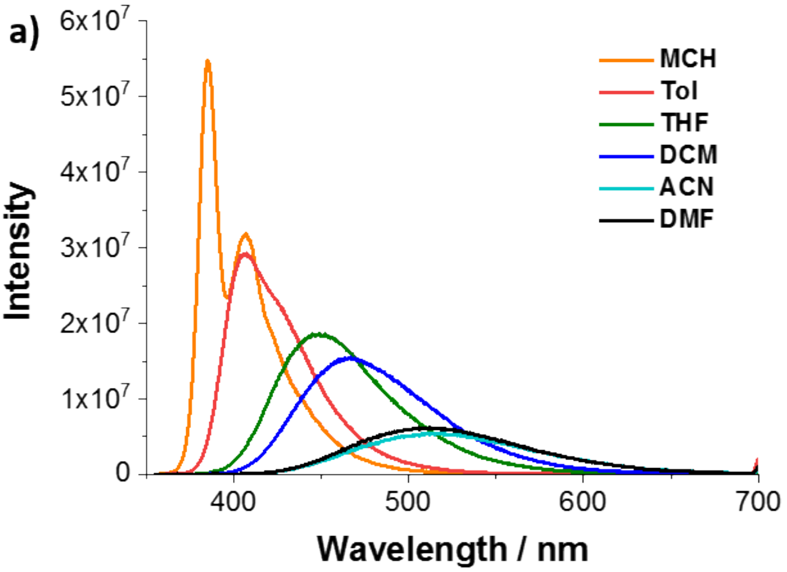
a)
6x10^7
5x10^7
4x10^7
3x10^7
2x10^7
1x10^7
0
Intensity
400
500
600
700
Wavelength / nm
MCH
Tol
THF
DCM
ACN
DMF

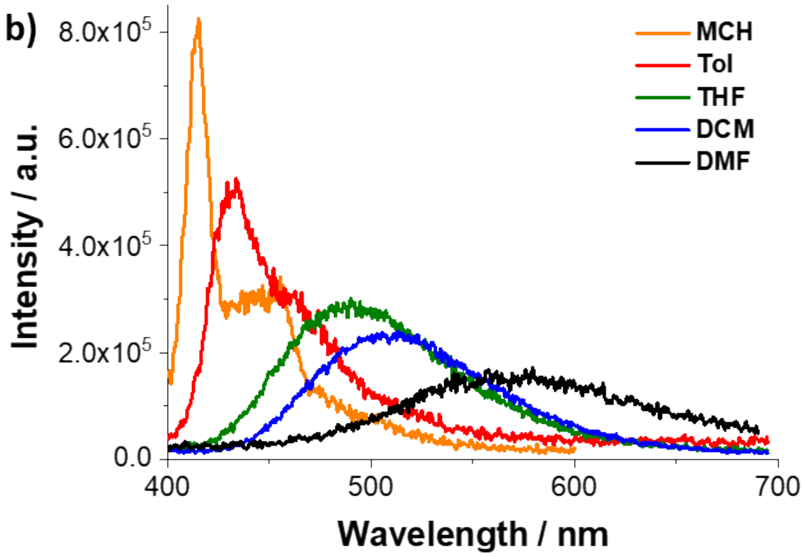
b)
8.0x10^5
6.0x10^5
4.0x10^5
2.0x10^5
0.0
Intensity / a.u.
400
500
600
700
Wavelength / nm
MCH
Tol
THF
DCM
DMF

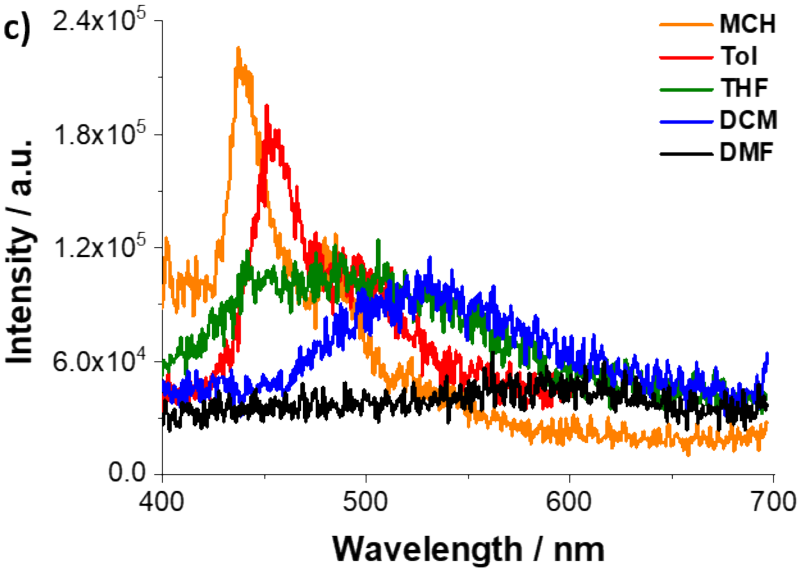

Figure S7. Room temperature fluorescence spectra of a) **1**, b) **3**, and c) **4** in solvents of different polarity (MCH – methylcyclohexane, Tol – toluene, THF – tetrahydrofuran, DCM – dichloromethane, DMF – *N*,*N* – dimethylformamide) with matching the absorption of OD = 0.05 upon 350 nm excitation.

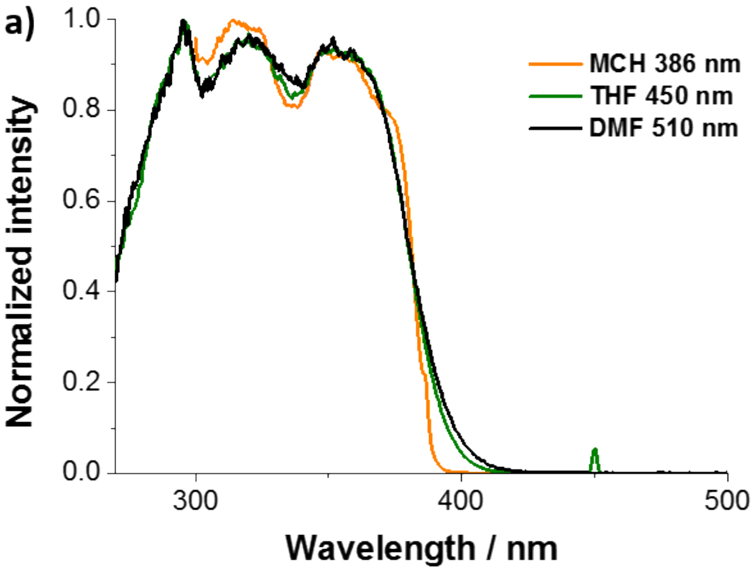
a)
Normalized intensity
Wavelength / nm
0.0
0.2
0.4
0.6
0.8
1.0
300
400
500
MCH 386 nm
THF 450 nm
DMF 510 nm

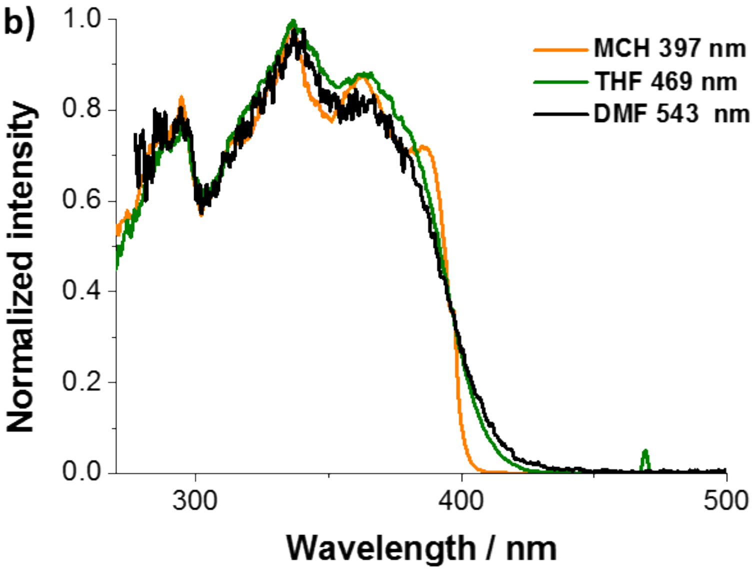
b)
Normalized intensity
Wavelength / nm
0.0
0.2
0.4
0.6
0.8
1.0
300
400
500
MCH 397 nm
THF 469 nm
DMF 543 nm

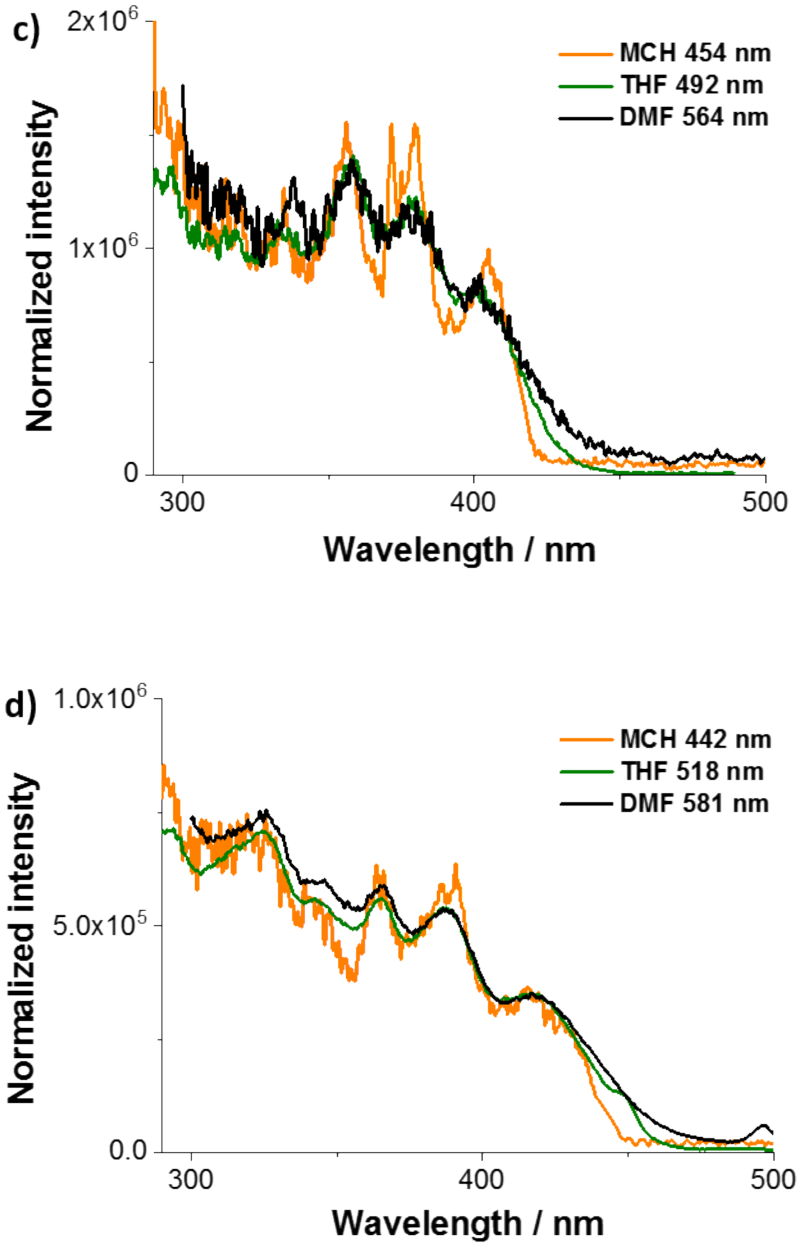

Figure S8. Room temperature excitation spectra of a) **1**, b) **2**, c) **3**, and d) **4** with the detection at the indicated wavelengths in MCH, THF, and DMF.

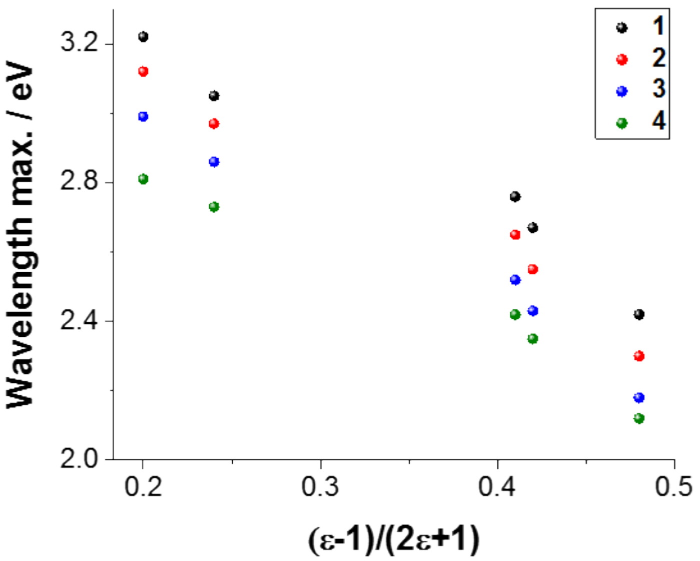

Figure S9. The emission maxima plotted as a function of Kirkwood parameter.

a)

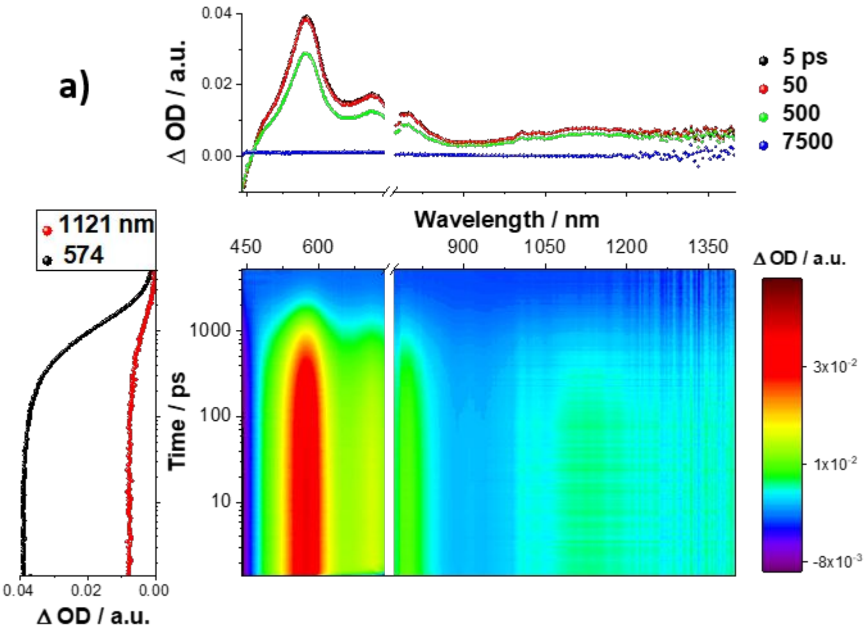
Δ OD / a.u.
0.04
0.02
0.00
5 ps
50
500
7500
Wavelength / nm
450
600
900
1050
1200
1350
1121 nm
574
Time / ps
1000
100
10
0.04
0.02
0.00
Δ OD / a.u.
Δ OD / a.u.
3x10-2
1x10-2
-8x10-3

b)

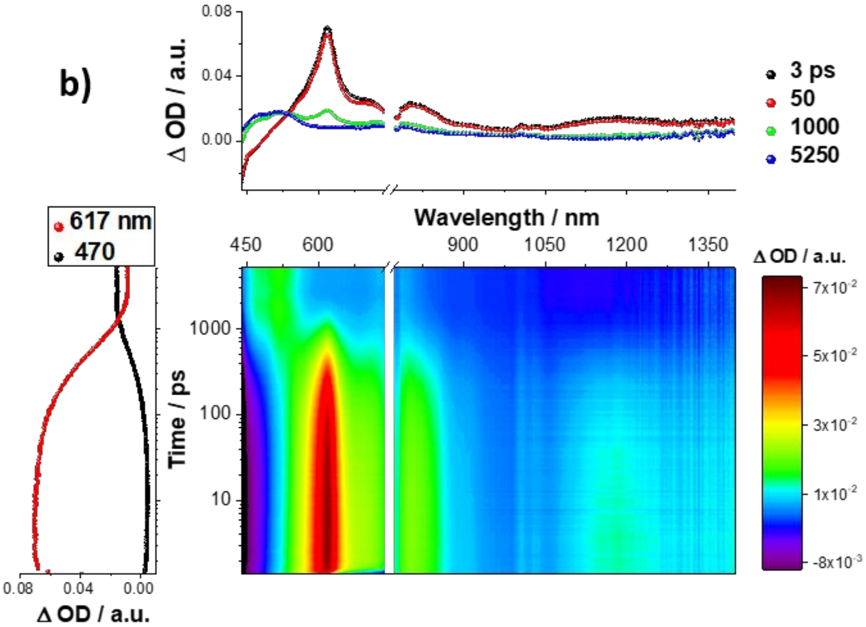
Δ OD / a.u.
0.08
0.04
0.00
3 ps
50
1000
5250
Wavelength / nm
450
600
900
1050
1200
1350
617 nm
470
Time / ps
1000
100
10
0.08
0.04
0.00
Δ OD / a.u.
Δ OD / a.u.
7x10-2
5x10-2
3x10-2
1x10-2
-8x10-3

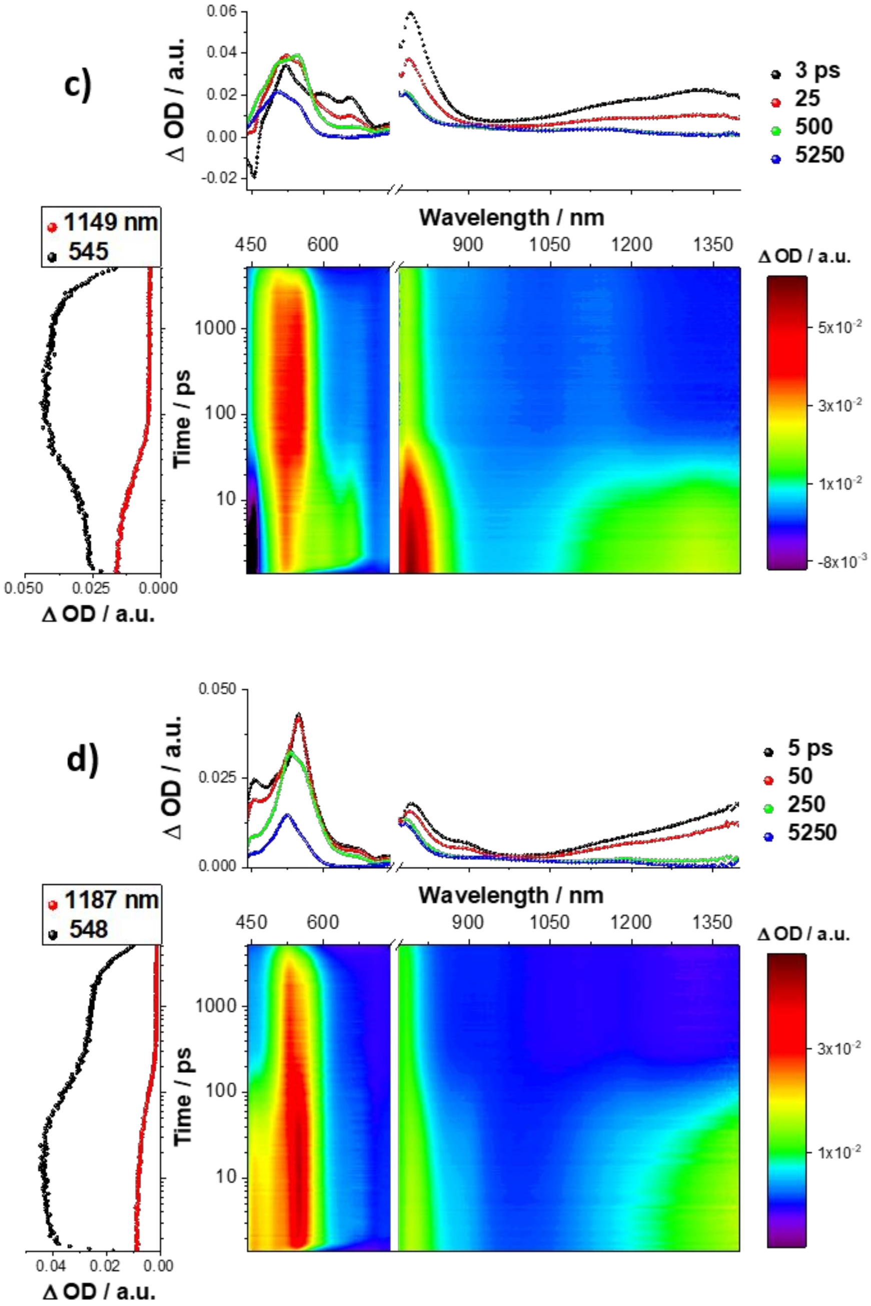

Figure S10. Differential absorption spectra (visible and near-infrared) obtained upon femtosecond flash photolysis (387 nm) of a) **1**, b) **2**, c) **3**, and d) **4** in argon-saturated MCH with several time delays between 0 and 5500 ps at room temperature. The lower left graphs depict time absorption profiles of the spectra. The upper right spectra show differential absorption spectra with the depicted time delays.

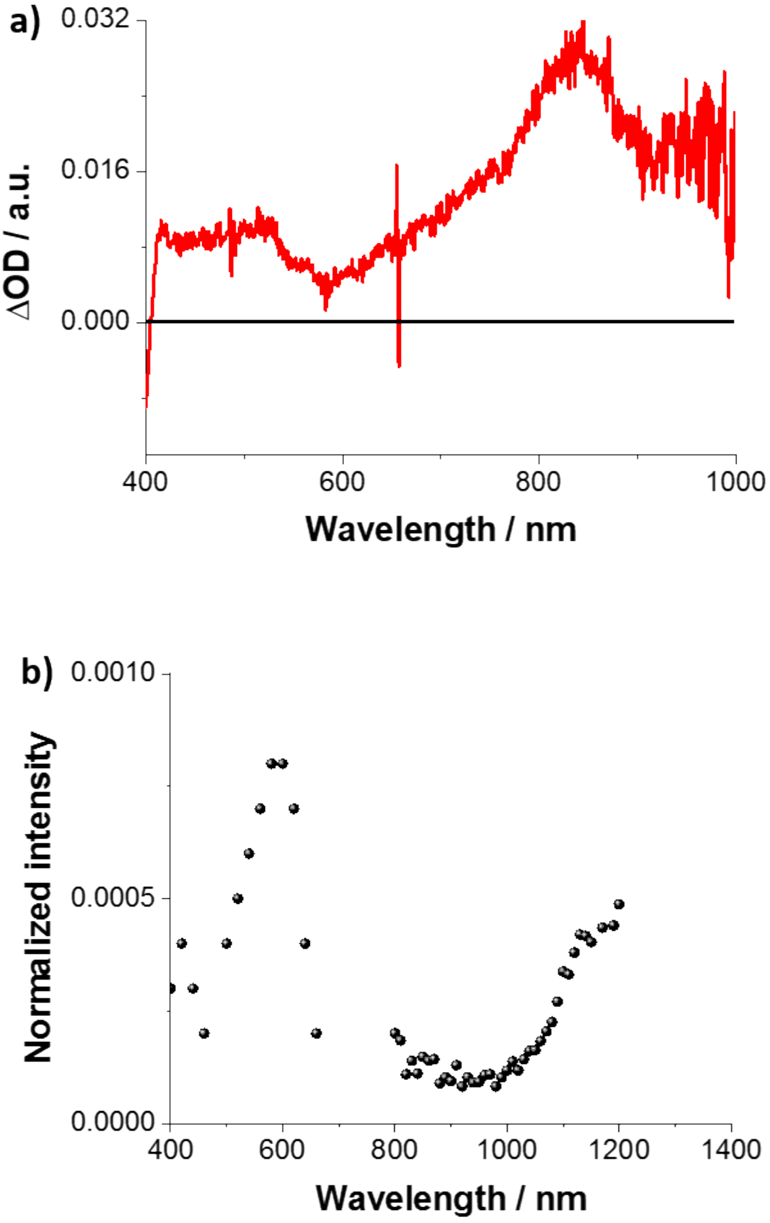

Figure S11. a) The spectroelectrochemical spectrum of **2** in DCM upon application of +1.3 V versus Ag/Ag$^+$, with TBAPF$_6$ used as the electrolyte. b) Differential absorption spectrum obtained upon electron pulse radiolysis of **2** with the time delay of 5 µs after the electron pulse.

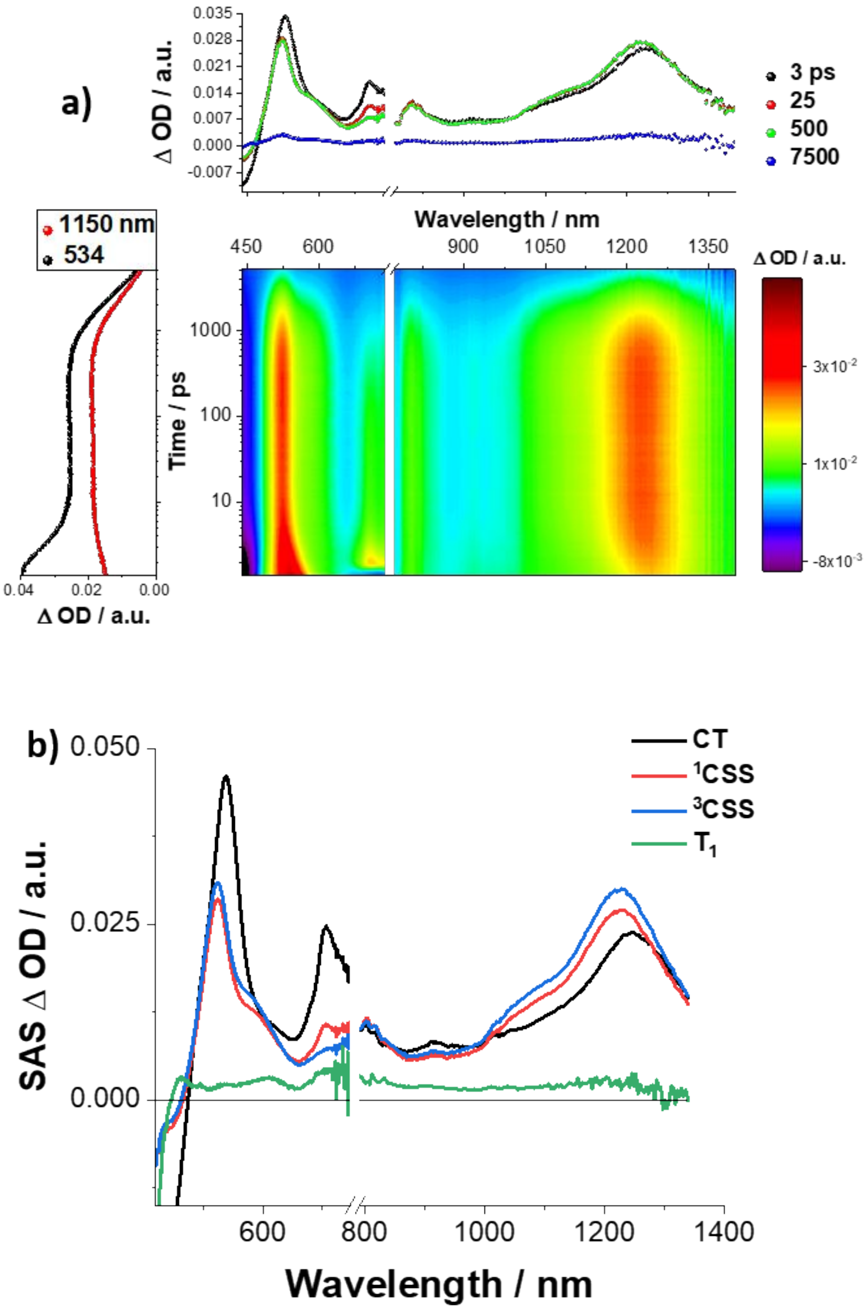
a)
Δ OD / a.u.
0.035
0.028
0.021
0.014
0.007
0.000
-0.007
3 ps
25
500
7500
Wavelength / nm
450
600
900
1050
1200
1350
1150 nm
534
Time / ps
1000
100
10
Δ OD / a.u.
0.04
0.02
0.00
Δ OD / a.u.
3x10-2
1x10-2
-8x10-3
b)
SAS Δ OD / a.u.
0.050
0.025
0.000
CT
1CSS
3CSS
T1
600
800
1000
1200
1400
Wavelength / nm

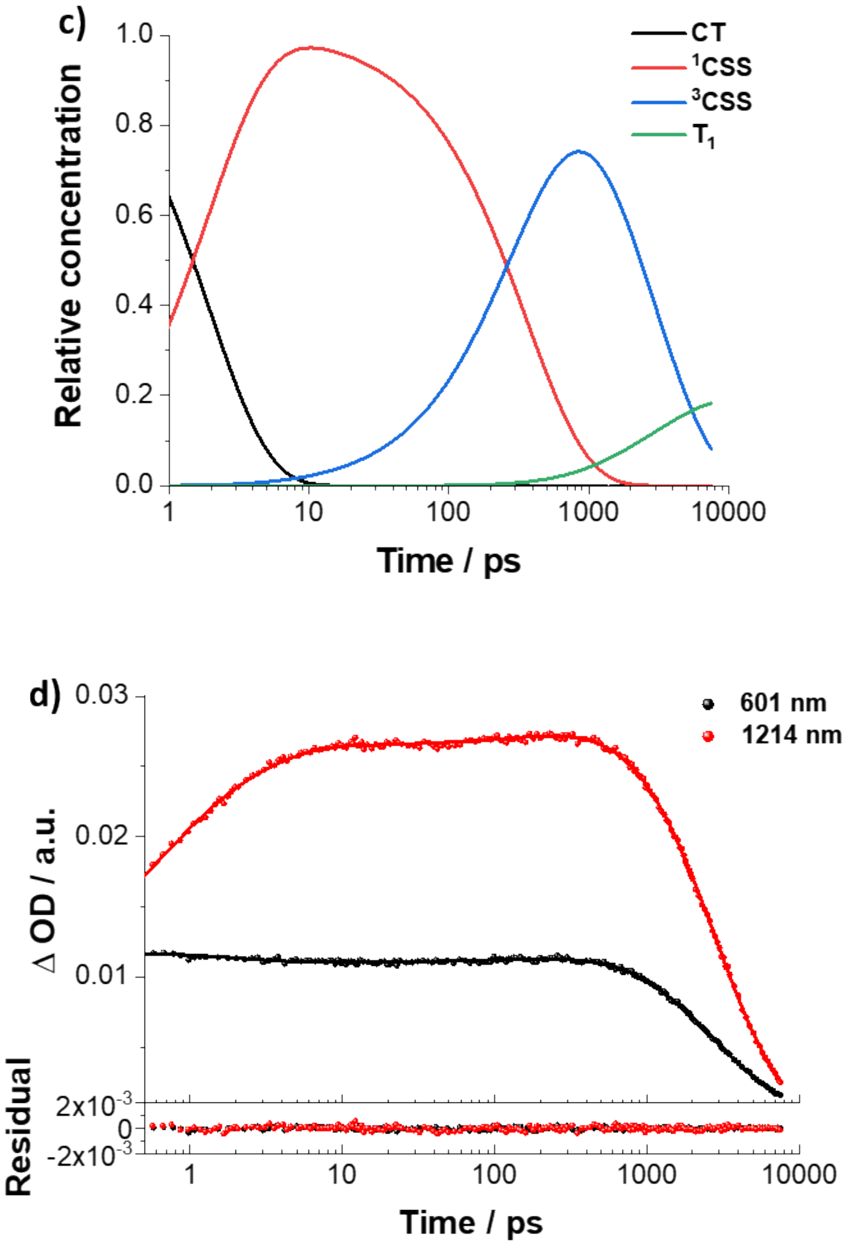

Figure S12. a) Differential absorption spectra (visible and near-infrared) obtained upon femtosecond flash photolysis (387 nm) of **1** in argon-saturated THF with several time delays between 0 and 7500 ps at room temperature. Lower left: Time absorption profiles of the spectra at 534 and 1150 nm. Upper Right: Differential absorption spectra with the depicted time delays. b) Deconvoluted species associated spectra (SAS) of CT (black), ^{1}CSS (red), ^{3}CSS (blue), and T_1 (green) in THF as obtained by global target analysis of time-resolved spectra on the sub-ps to ns timescale. c) Evolution of the population of the involved states in **1** in THF. d) Time absorption profiles at 601 and 1214 nm as well as the corresponding fits and residuals.

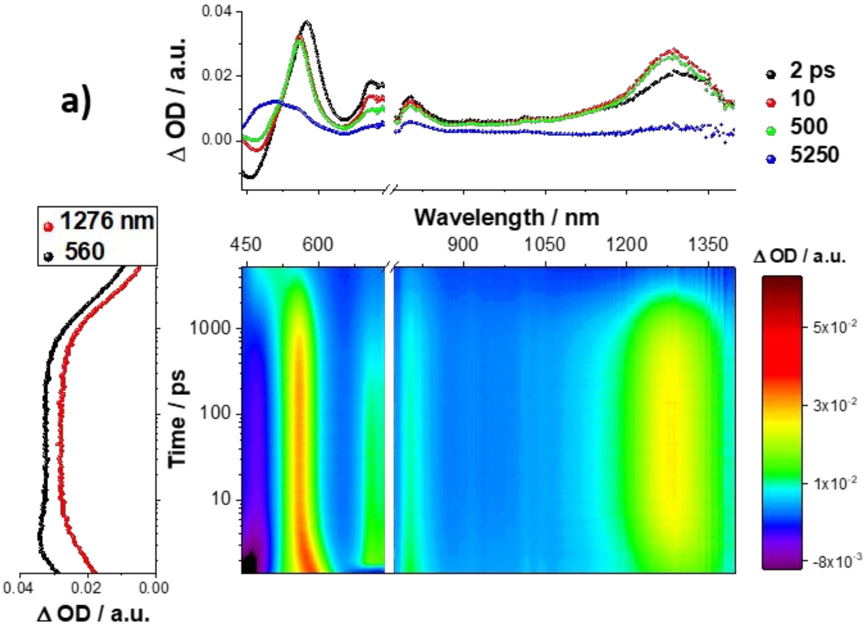
a)
Δ OD / a.u.
0.04
0.02
0.00
2 ps
10
500
5250
Wavelength / nm
450
600
900
1050
1200
1350
Δ OD / a.u.
5x10-2
3x10-2
1x10-2
-8x10-3
Time / ps
1000
100
10
1276 nm
560
0.04
0.02
0.00
Δ OD / a.u.

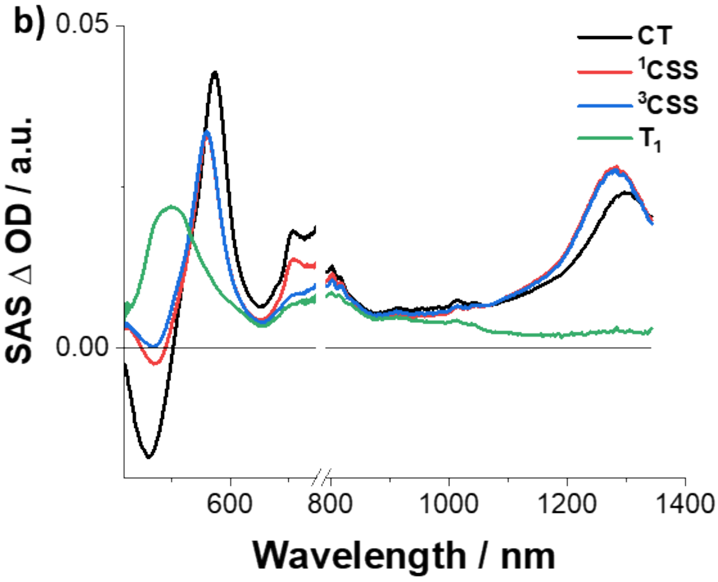
b)
0.05
0.00
SAS Δ OD / a.u.
CT
1CSS
3CSS
T1
600
800
1000
1200
1400
Wavelength / nm

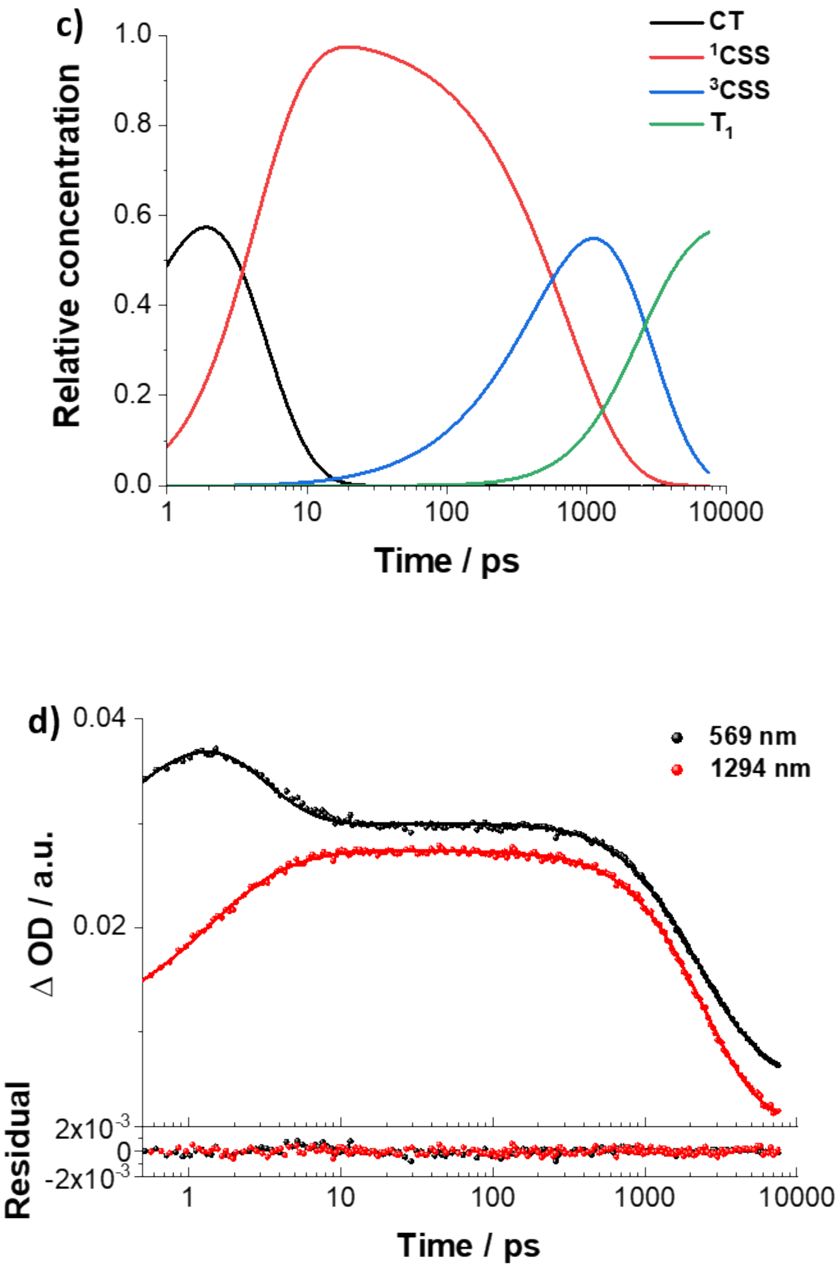

Figure S13. a) Differential absorption spectra (visible and near-infrared) obtained upon femtosecond flash photolysis (387 nm) of **2** in argon-saturated THF with several time delays between 0 and 7500 ps at room temperature. Lower left: Time absorption profiles of the spectra at 560 and 1276 nm. Upper Right: Differential absorption spectra with the depicted time delays. b) Deconvoluted species associated spectra (SAS) of CT (black), ^{1}CSS (red), ^{3}CSS (blue), and T_1 (green) in THF as obtained by global target analysis of time-resolved spectra on the sub-ps to ns timescale. c) Evolution of the population of the involved states in **2** in THF. d) Time absorption profiles at 569 and 1294 nm as well as the corresponding fits and residuals.

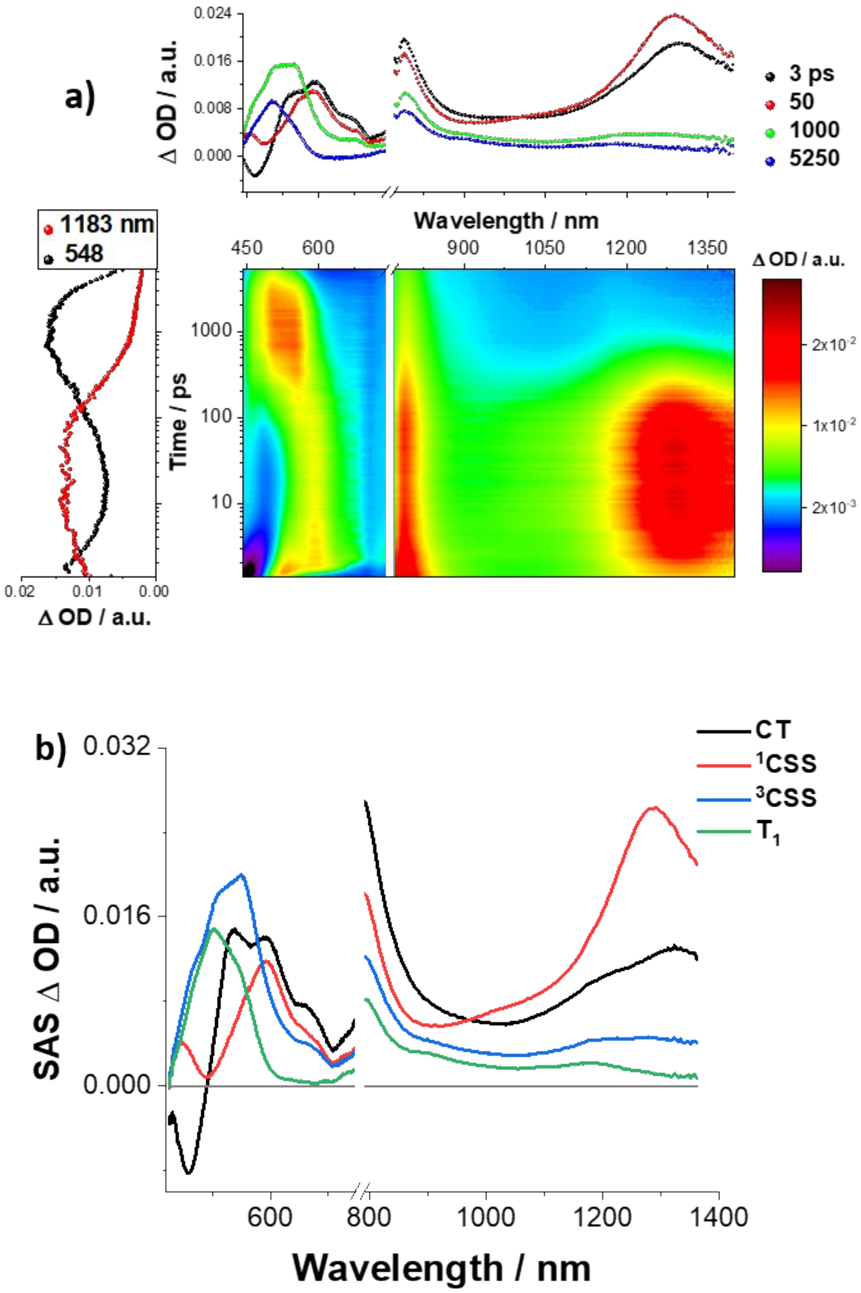
a)
Δ OD / a.u.
0.024
0.016
0.008
0.000
3 ps
50
1000
5250
Wavelength / nm
1183 nm
548
450
600
900
1050
1200
1350
Δ OD / a.u.
1000
100
10
Time / ps
2x10-2
1x10-2
2x10-3
0.02
0.01
0.00
Δ OD / a.u.
b)
0.032
0.016
0.000
SAS Δ OD / a.u.
CT
1CSS
3CSS
T1
600
800
1000
1200
1400
Wavelength / nm

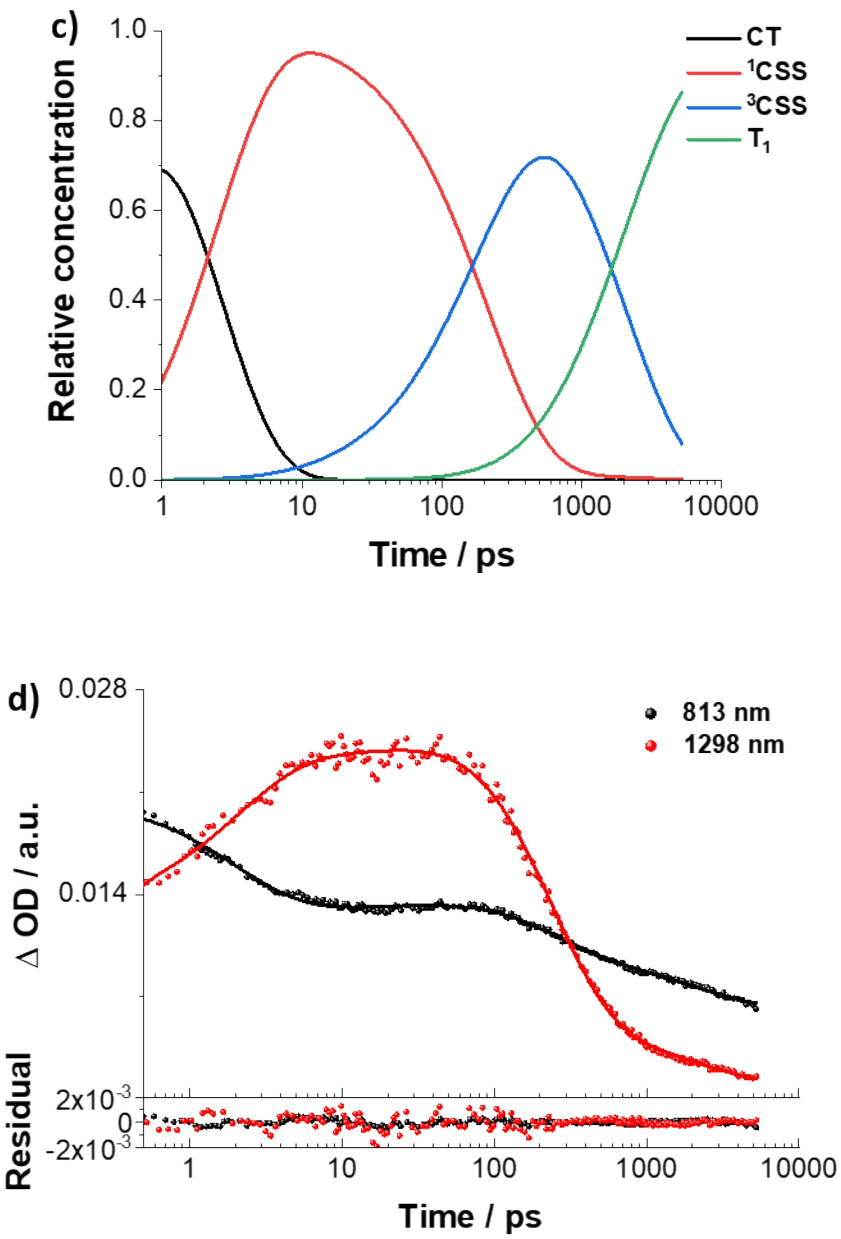

Figure S14. a) Differential absorption spectra (visible and near-infrared) obtained upon femtosecond flash photolysis (387 nm) of **3** in argon-saturated THF with several time delays between 0 and 7500 ps at room temperature. Lower left: Time absorption profiles of the spectra at 548 and 1183 nm. Upper Right: Differential absorption spectra with the depicted time delays. b) Deconvoluted species associated spectra (SAS) of CT (black), ^{1}CSS (red), ^{3}CSS (blue), and T_1 (green) in THF as obtained by global target analysis of time-resolved spectra on the sub-ps to ns timescale. c) Evolution of the population of the involved states in **3** in THF. d) Time absorption profiles at 813 and 1298 nm as well as the corresponding fits and residuals.

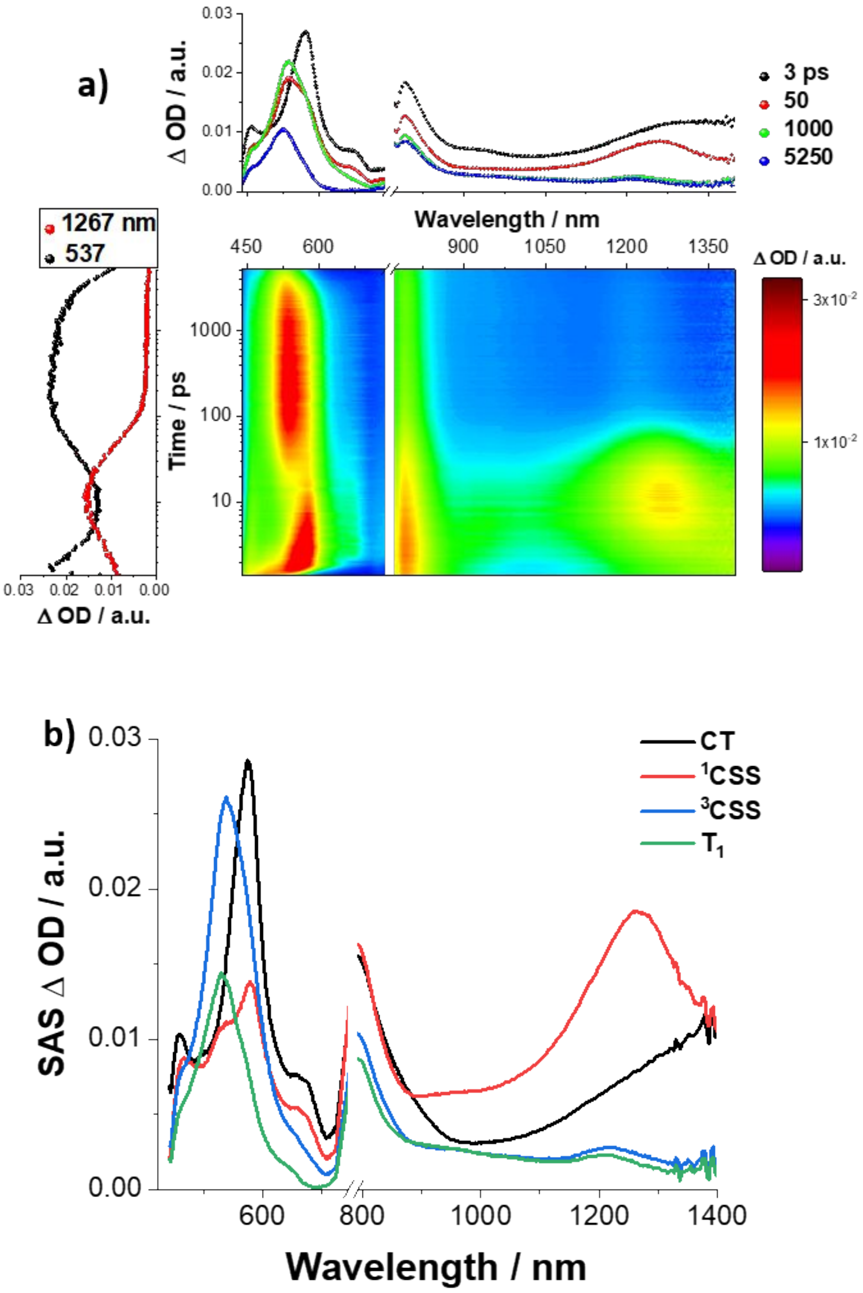
a)
Δ OD / a.u.
0.03
0.02
0.01
0.00
3 ps
50
1000
5250
Wavelength / nm
450
600
900
1050
1200
1350
1267 nm
537
Time / ps
1000
100
10
Δ OD / a.u.
3x10^-2
1x10^-2
0.03
0.02
0.01
0.00
Δ OD / a.u.
b)
SAS Δ OD / a.u.
0.03
0.02
0.01
0.00
600
800
1000
1200
1400
Wavelength / nm
CT
¹CSS
³CSS
T1

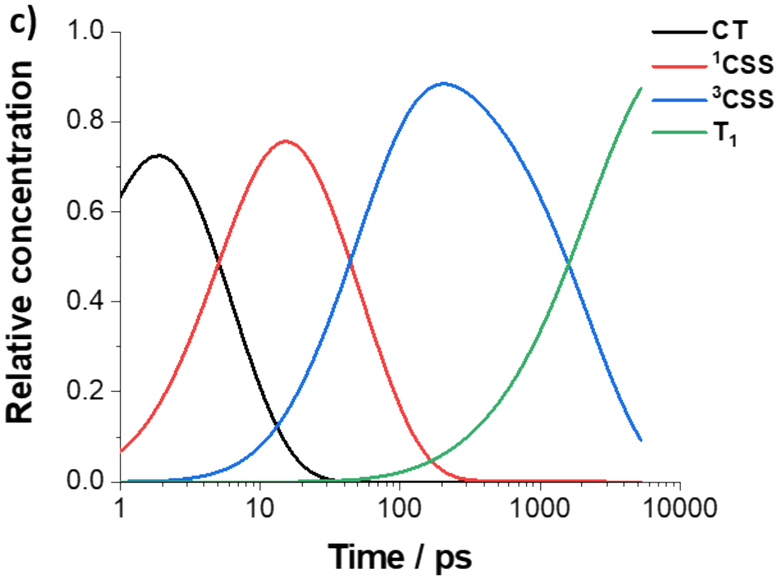

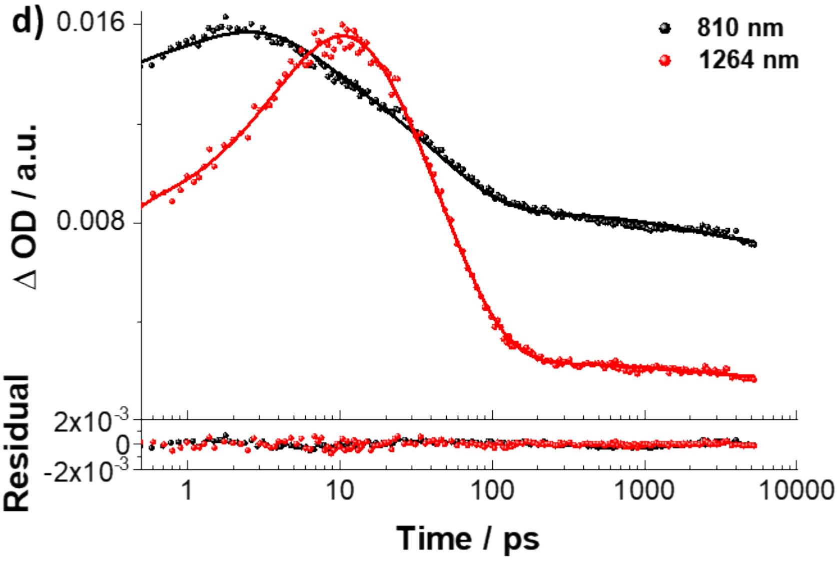

Figure S15. a) Differential absorption spectra (visible and near-infrared) obtained upon femtosecond flash photolysis (387 nm) of **4** in argon-saturated THF with several time delays between 0 and 5500 ps at room temperature. Lower left: Time absorption profiles of the spectra at 537 and 1267 nm. Upper Right: Differential absorption spectra with the depicted time delays. b) Deconvoluted species associated spectra (SAS) of CT (black), ^{1}CSS (red), ^{3}CSS (blue), and T_1 (green) in THF as obtained by global target analysis of time-resolved spectra on the sub-ps to ns timescale. c) Evolution of the population of the involved states in **4** in THF. d) Time absorption profiles at 810 and 1264 nm as well as the corresponding fits and residuals.

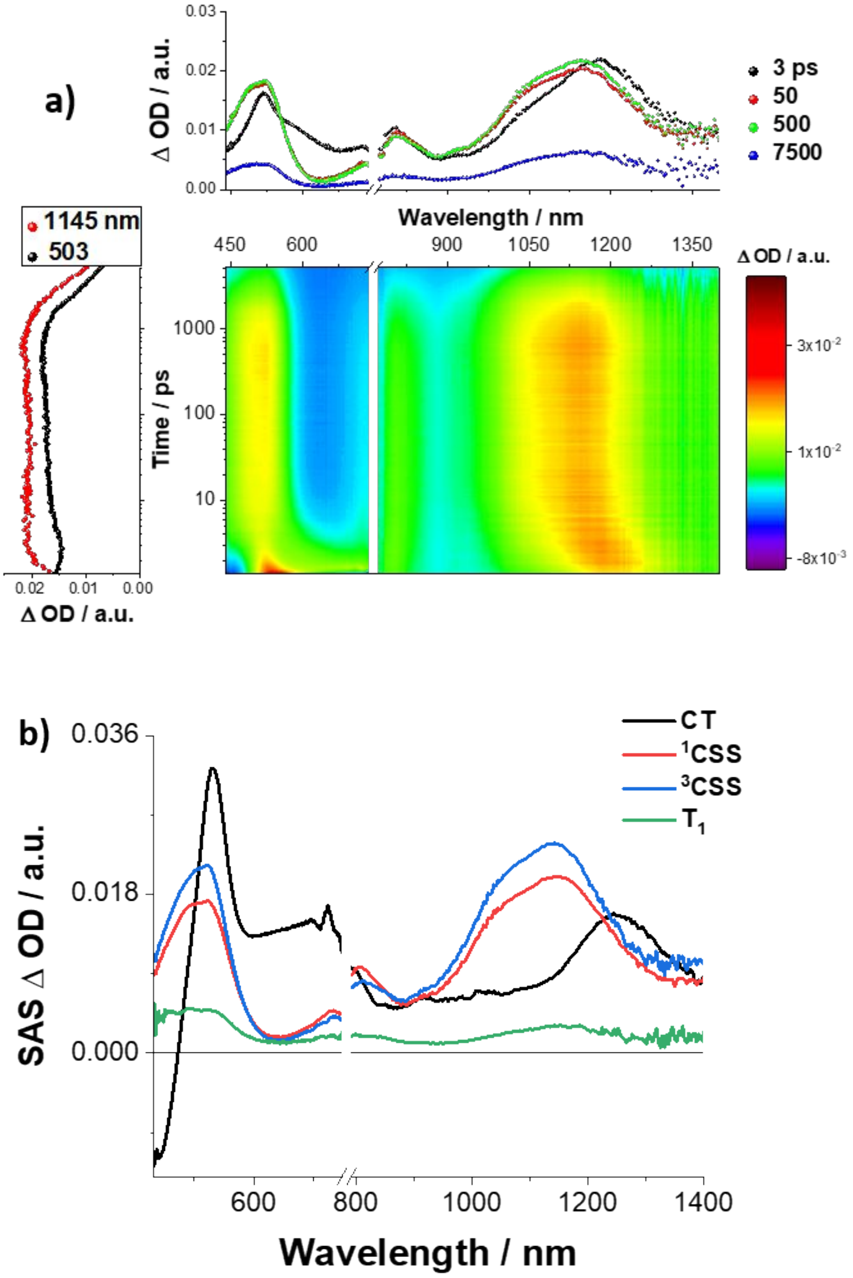
a)
Δ OD / a.u.
0.03
0.02
0.01
0.00
3 ps
50
500
7500
Wavelength / nm
450
600
900
1050
1200
1350
1145 nm
503
Time / ps
1000
100
10
0.02
0.01
0.00
Δ OD / a.u.
Δ OD / a.u.
3x10-2
1x10-2
-8x10-3
b)
0.036
0.018
0.000
SAS Δ OD / a.u.
CT
1CSS
3CSS
T1
600
800
1000
1200
1400
Wavelength / nm

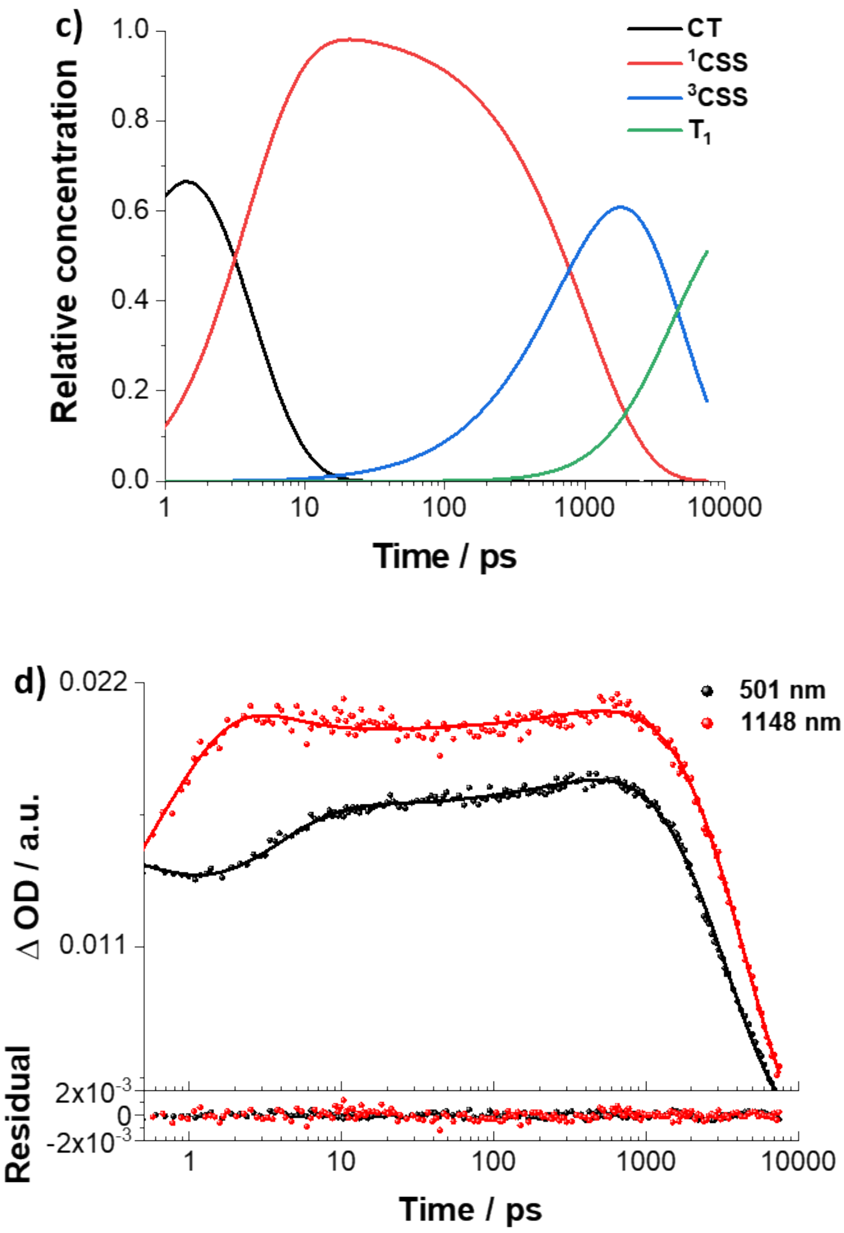

Figure S16. a) Differential absorption spectra (visible and near-infrared) obtained upon femtosecond flash photolysis (387 nm) of **1** in argon-saturated DMF with several time delays between 0 and 7500 ps at room temperature. Lower left: Time absorption profiles of the spectra at 503 and 1145 nm. Upper Right: Differential absorption spectra with the depicted time delays. b) Deconvoluted species associated spectra (SAS) of CT (black), ^{1}CSS (red), ^{3}CSS (blue), and T_1 (green) in DMF as obtained by global target analysis of time-resolved spectra on the sub-ps to ns timescale. c) Evolution of the population of the involved states in **1** in DMF. d) Time absorption profiles at 501 and 1148 nm as well as the corresponding fits and residuals.

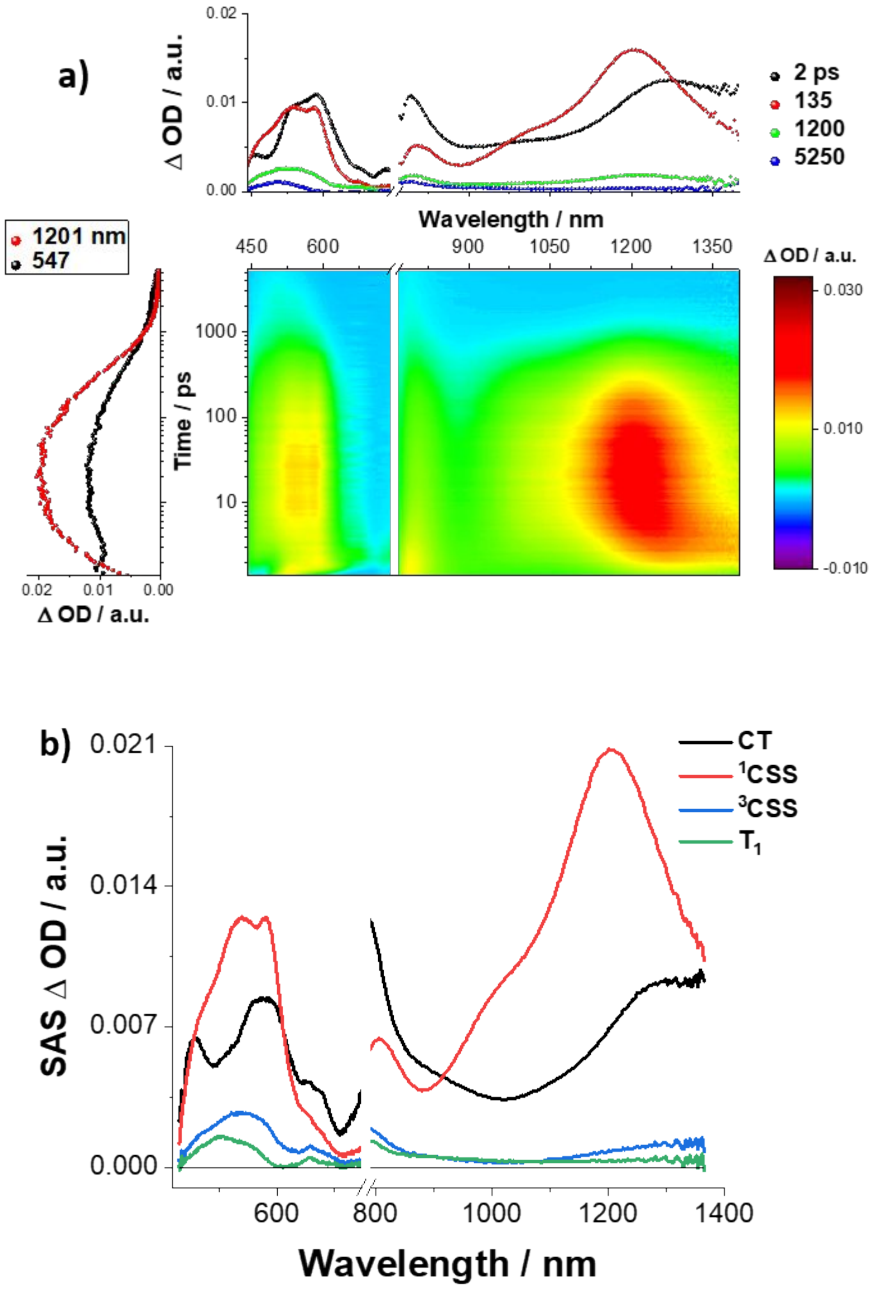
a)
Δ OD / a.u.
0.02
0.01
0.00
2 ps
135
1200
5250
Wavelength / nm
450
600
900
1050
1200
1350
1201 nm
547
Time / ps
1000
100
10
0.02
0.01
0.00
Δ OD / a.u.
Δ OD / a.u.
0.030
0.010
-0.010
b)
SAS Δ OD / a.u.
0.021
0.014
0.007
0.000
CT
^{1}CSS
^{3}CSS
T_1
600
800
1000
1200
1400
Wavelength / nm

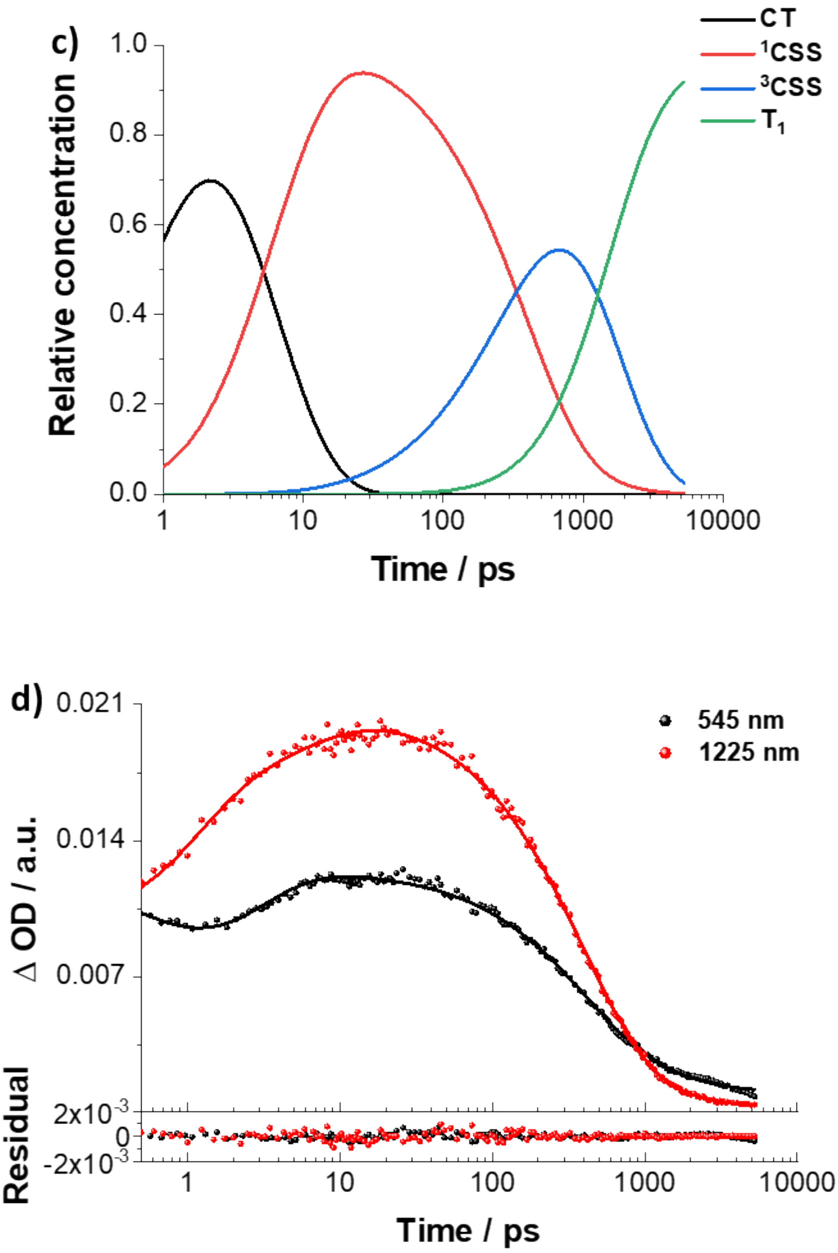

Figure S17. a) Differential absorption spectra (visible and near-infrared) obtained upon femtosecond flash photolysis (387 nm) of **3** in argon-saturated DMF with several time delays between 0 and 5500 ps at room temperature. Lower left: Time absorption profiles of the spectra at 547 and 1201 nm. Upper Right: Differential absorption spectra with the depicted time delays. b) Deconvoluted species associated spectra (SAS) of CT (black), ^{1}CSS (red), ^{3}CSS (blue), and T_1 (green) in DMF as obtained by global target analysis of time-resolved spectra on the sub-ps to ns timescale. c) Evolution of the population of the involved states in **3** in DMF. d) Time absorption profiles at 545 and 1225 nm as well as the corresponding fits and residuals.

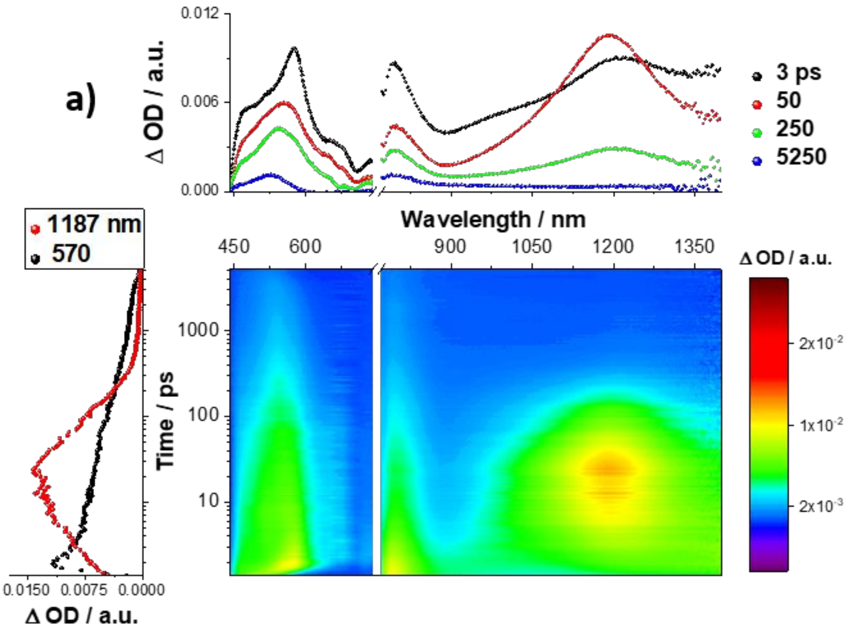
a)
0.012
0.006
0.000
Δ OD / a.u.
3 ps
50
250
5250
Wavelength / nm
450
600
900
1050
1200
1350
1187 nm
570
Time / ps
1000
100
10
0.0150
0.0075
0.0000
Δ OD / a.u.
Δ OD / a.u.
2x10-2
1x10-2
2x10-3

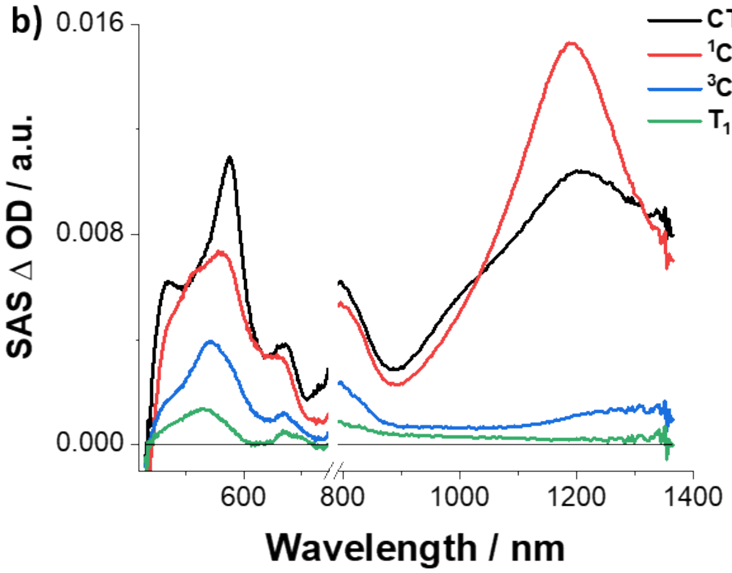
b)
0.016
0.008
0.000
SAS Δ OD / a.u.
CT
1CSS
3CSS
T1
600
800
1000
1200
1400
Wavelength / nm

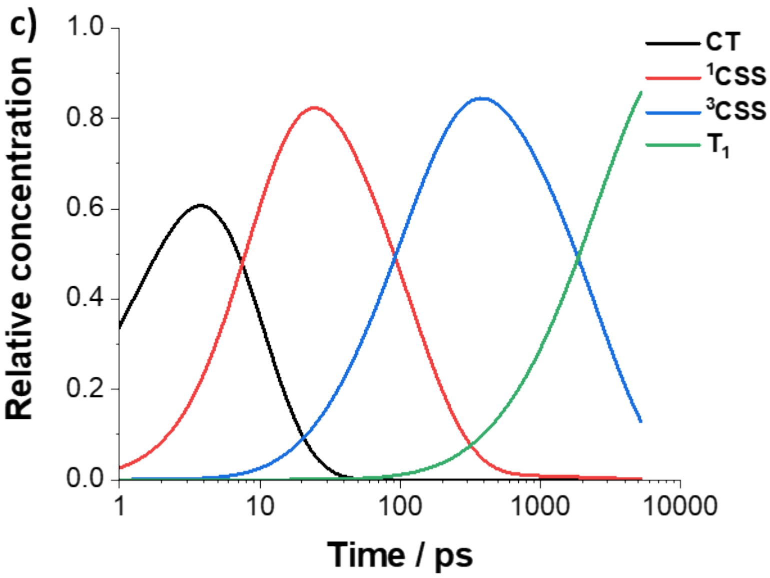

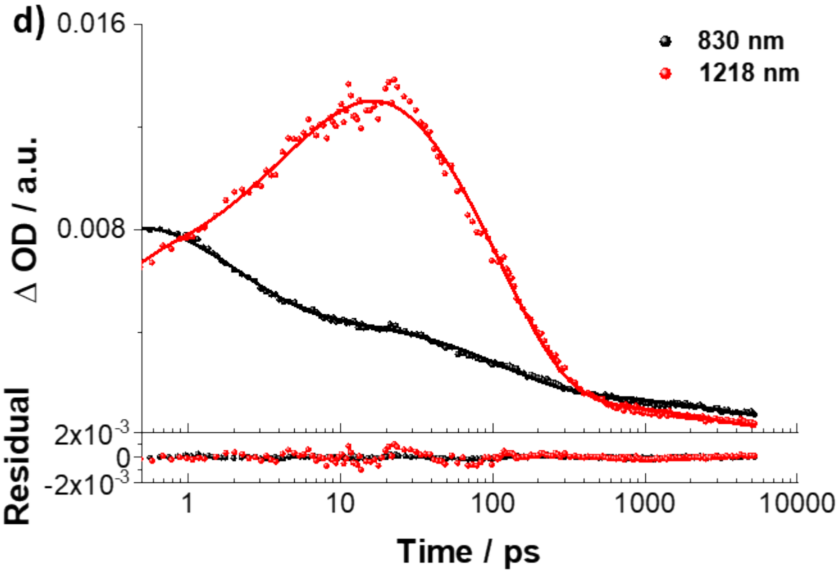

Figure S18. a) Differential absorption spectra (visible and near-infrared) obtained upon femtosecond flash photolysis (387 nm) of **4** in argon-saturated DMF with several time delays between 0 and 5500 ps at room temperature. Lower left: Time absorption profiles of the spectra at 570 and 1187 nm. Upper Right: Differential absorption spectra with the depicted time delays. b) Deconvoluted species associated spectra (SAS) of CT (black), ^{1}CSS (red), ^{3}CSS (blue), and T_1 (green) in DMF as obtained by global target analysis of time-resolved spectra on the sub-ps to ns timescale. c) Evolution of the population of the involved states in **4** in DMF. d) Time absorption profiles at 830 and 1218 nm as well as the corresponding fits and residuals.

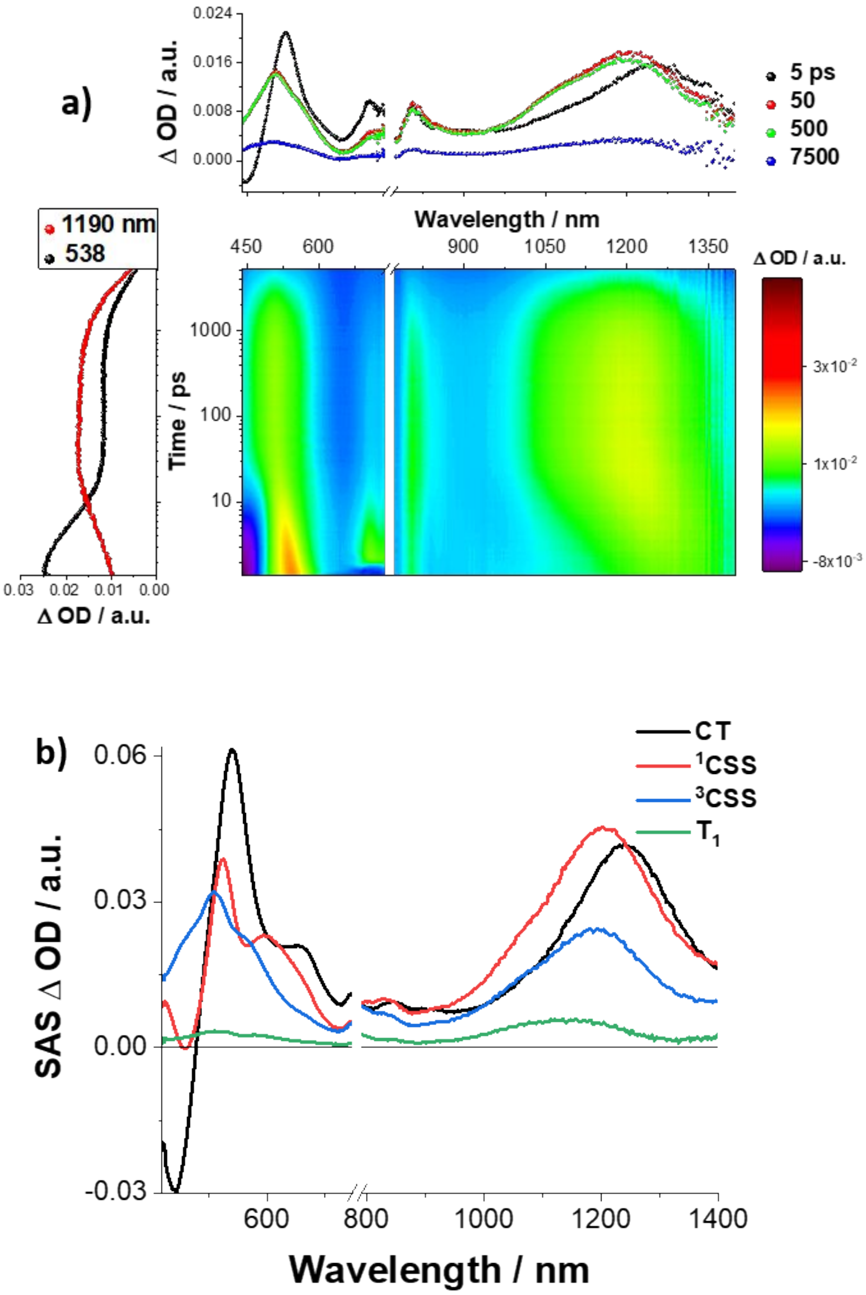
a)
Δ OD / a.u.
0.024
0.016
0.008
0.000
5 ps
50
500
7500
Wavelength / nm
1190 nm
538
450
600
900
1050
1200
1350
Δ OD / a.u.
Time / ps
1000
100
10
3x10-2
1x10-2
-8x10-3
0.03
0.02
0.01
0.00
Δ OD / a.u.
b)
0.06
0.03
0.00
-0.03
SAS Δ OD / a.u.
CT
1CSS
3CSS
T1
600
800
1000
1200
1400
Wavelength / nm

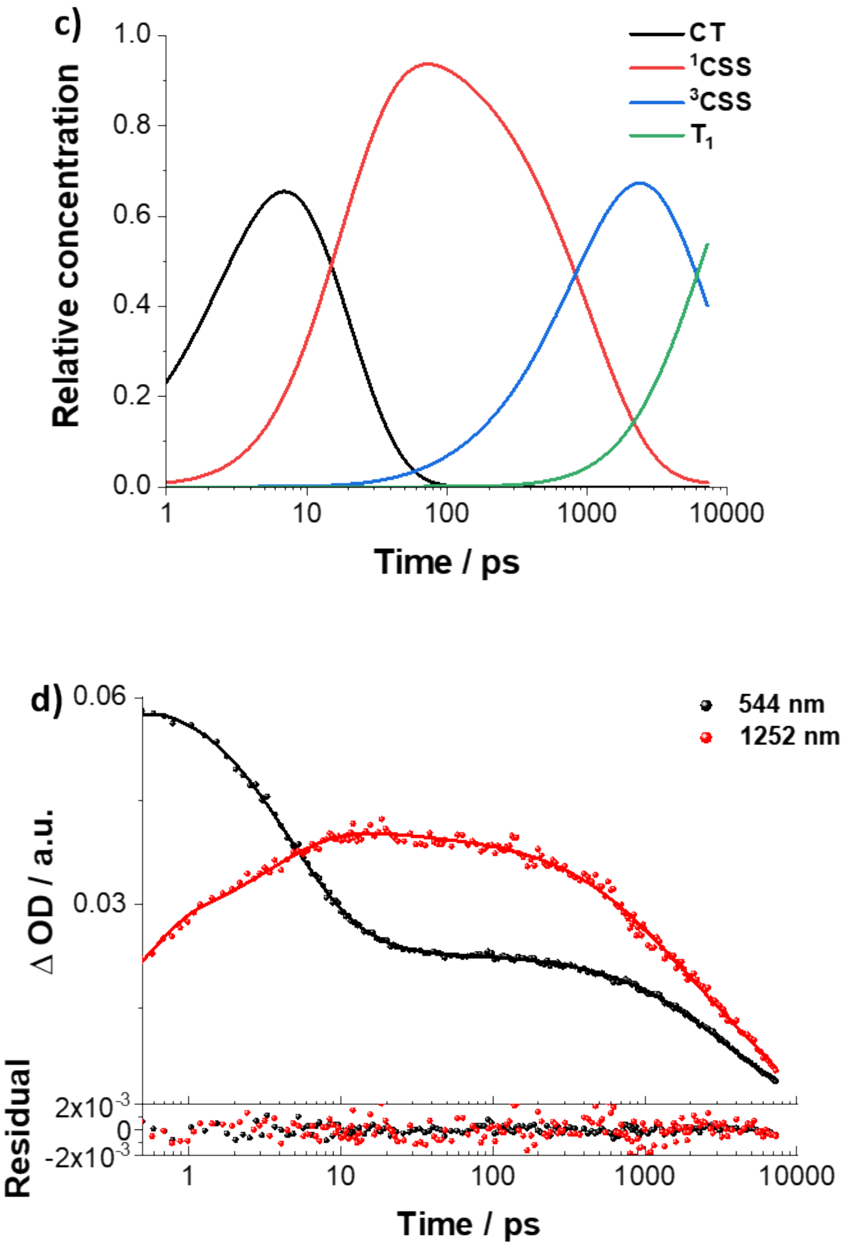

Figure S19. a) Differential absorption spectra (visible and near-infrared) obtained upon femtosecond flash photolysis (387 nm) of **1** in argon-saturated PhCN with several time delays between 0 and 7500 ps at room temperature. Lower left: Time absorption profiles of the spectra at 538 and 1190 nm. Upper Right: Differential absorption spectra with the depicted time delays. b) Deconvoluted species associated spectra (SAS) of CT (black), ^{1}CSS (red), ^{3}CSS (blue), and T_1 (green) in PhCN as obtained by global target analysis of time-resolved spectra on the sub-ps to ns timescale. c) Evolution of the population of the involved states in **1** in PhCN. d) Time absorption profiles at 544 and 1252 nm as well as the corresponding fits and residuals.

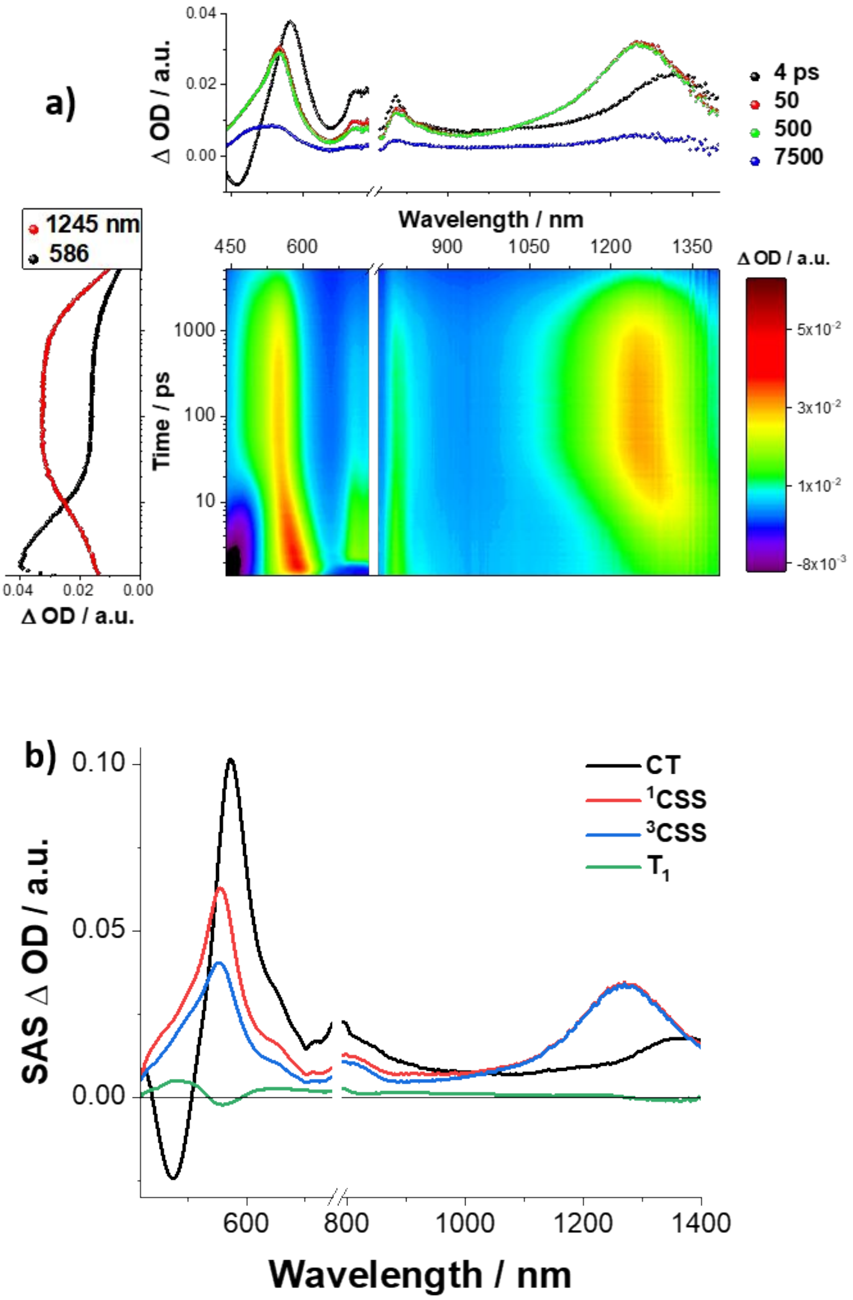
a)
Δ OD / a.u.
0.04
0.02
0.00
4 ps
50
500
7500
Wavelength / nm
450
600
900
1050
1200
1350
1245 nm
586
Time / ps
1000
100
10
Δ OD / a.u.
5x10-2
3x10-2
1x10-2
-8x10-3
0.04
0.02
0.00
Δ OD / a.u.
b)
0.10
0.05
0.00
SAS Δ OD / a.u.
CT
1CSS
3CSS
T1
600
800
1000
1200
1400
Wavelength / nm

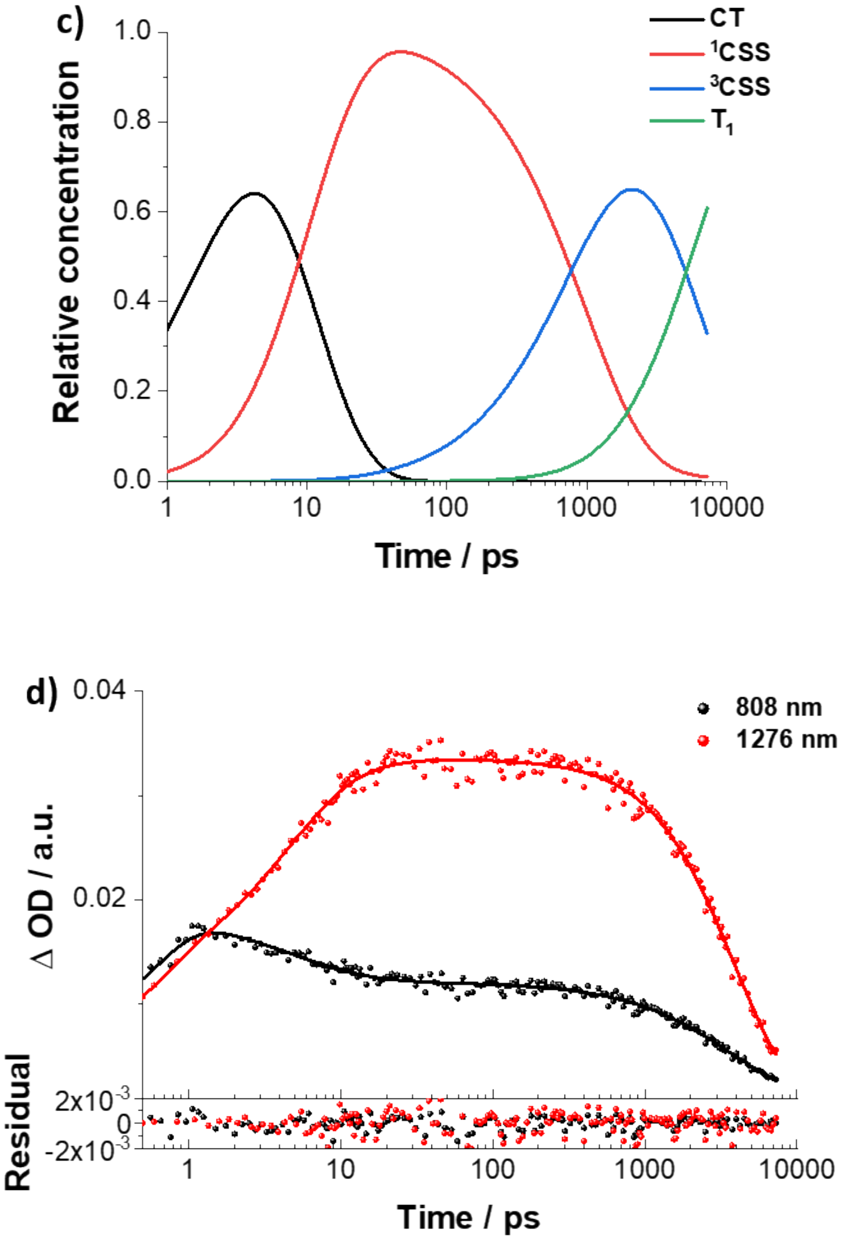

Figure S20. a) Differential absorption spectra (visible and near-infrared) obtained upon femtosecond flash photolysis (387 nm) of **2** in argon-saturated PhCN with several time delays between 0 and 7500 ps at room temperature. Lower left: Time absorption profiles of the spectra at 586 and 1245 nm. Upper Right: Differential absorption spectra with the depicted time delays. b) Deconvoluted species associated spectra (SAS) of CT (black), ^{1}CSS (red), ^{3}CSS (blue), and T_1 (green) in PhCN as obtained by global target analysis of time-resolved spectra on the sub-ps to ns timescale. c) Evolution of the population of the involved states in **2** in PhCN. d) Time absorption profiles at 808 and 1276 nm as well as the corresponding fits and residuals.

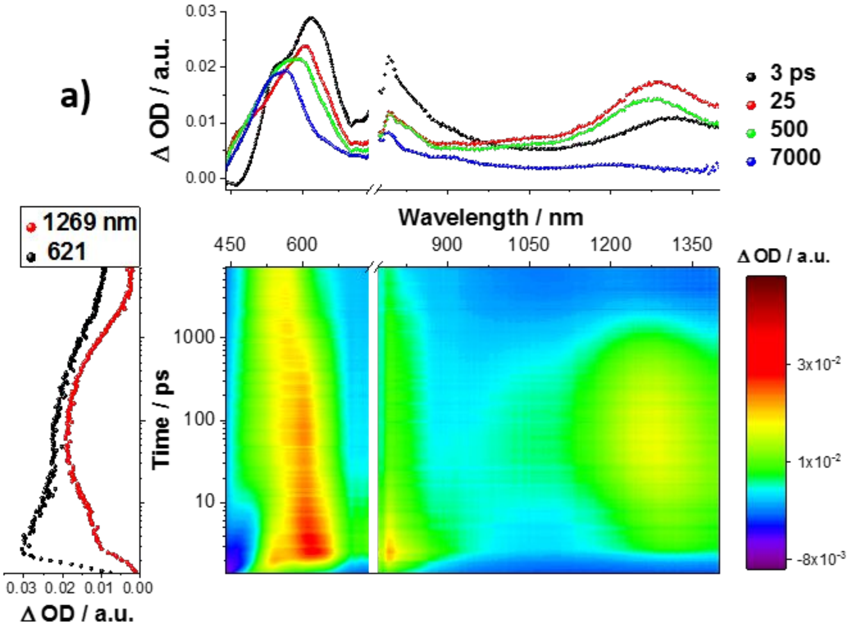
a)
Δ OD / a.u.
0.03
0.02
0.01
0.00
3 ps
25
500
7000
Wavelength / nm
450
600
900
1050
1200
1350
1269 nm
621
Time / ps
1000
100
10
0.03 0.02 0.01 0.00
Δ OD / a.u.
Δ OD / a.u.
3x10-2
1x10-2
-8x10-3

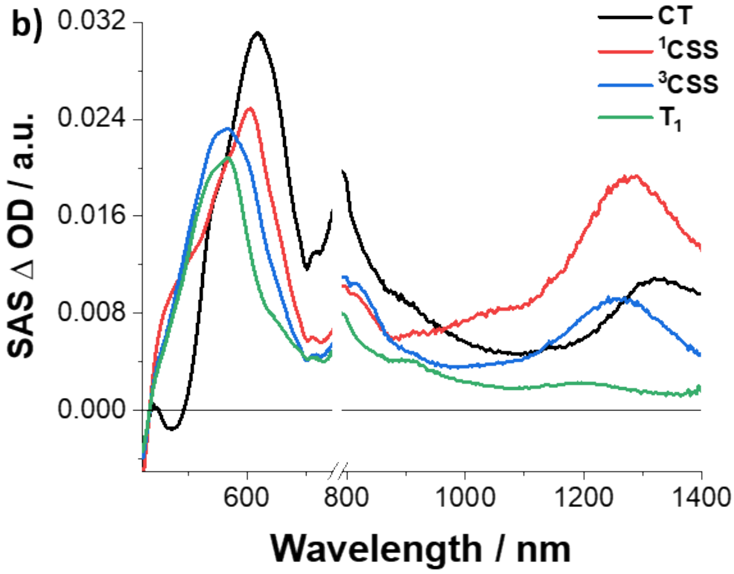
b)
SAS Δ OD / a.u.
0.032
0.024
0.016
0.008
0.000
CT
1CSS
3CSS
T1
600
800
1000
1200
1400
Wavelength / nm

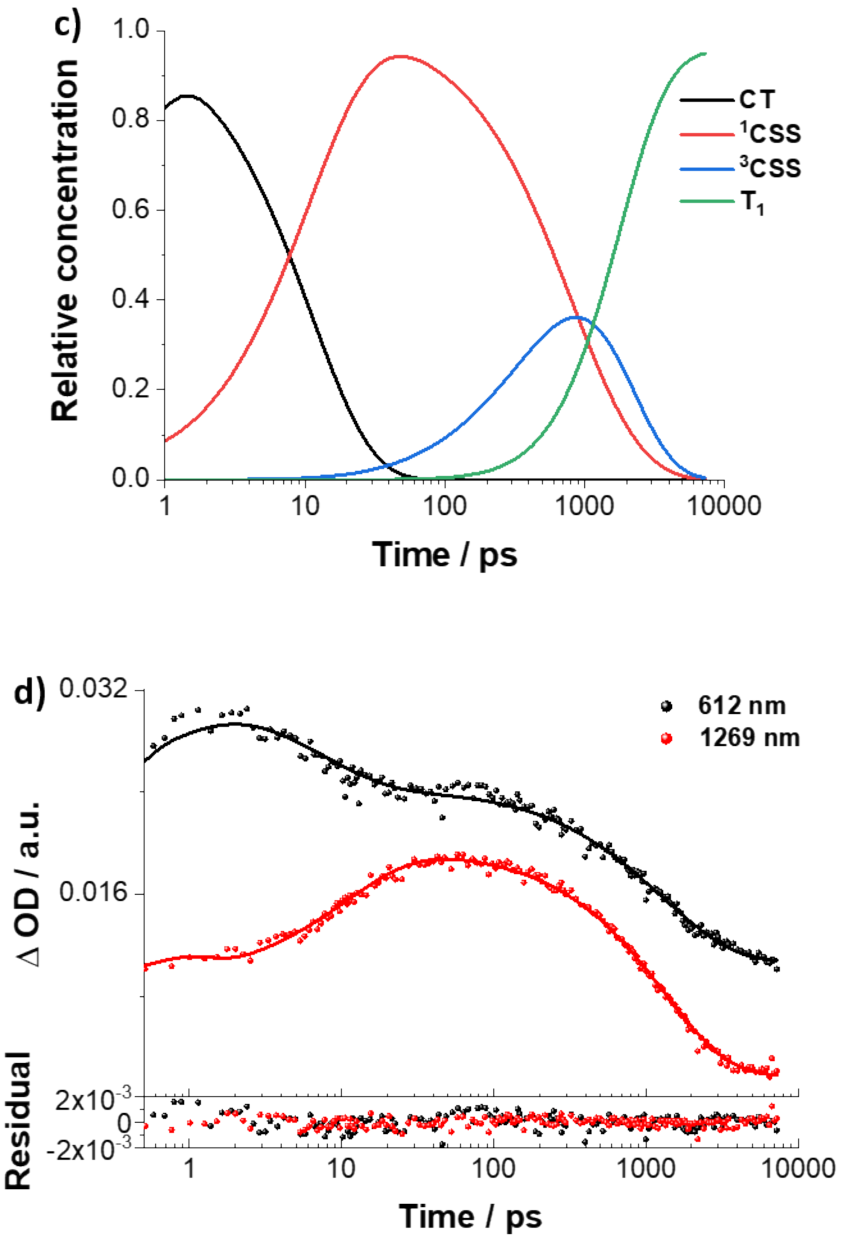

Figure S21. a) Differential absorption spectra (visible and near-infrared) obtained upon femtosecond flash photolysis (387 nm) of **3** in argon-saturated PhCN with several time delays between 0 and 7500 ps at room temperature. Lower left: Time absorption profiles of the spectra at 621 and 1269 nm. Upper Right: Differential absorption spectra with the depicted time delays. b) Deconvoluted species associated spectra (SAS) of CT (black), ^{1}CSS (red), ^{3}CSS (blue), and T_1 (green) in PhCN as obtained by global target analysis of time-resolved spectra on the sub-ps to ns timescale. c) Evolution of the population of the involved states in **3** in PhCN. d) Time absorption profiles at 612 and 1269 nm as well as the corresponding fits and residuals.

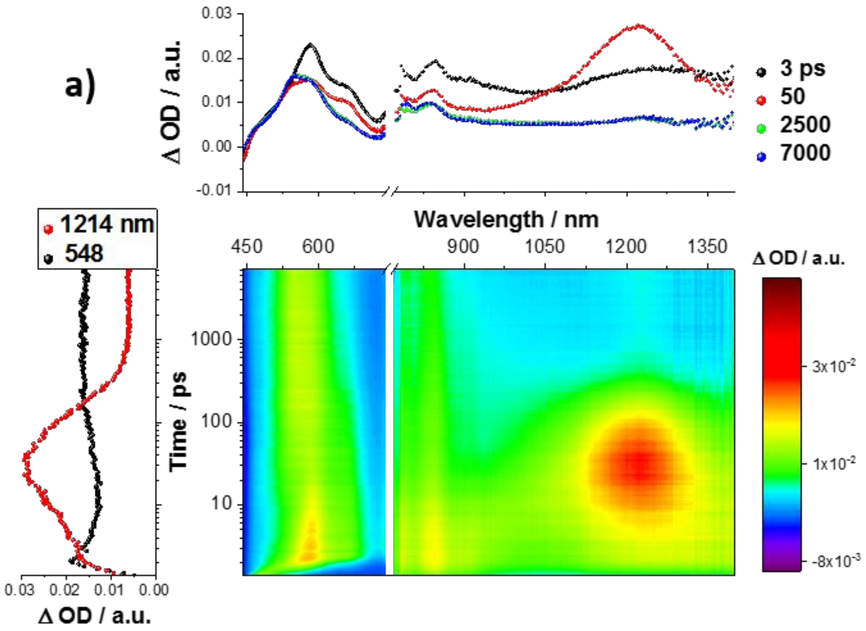
a)
Δ OD / a.u.
0.03
0.02
0.01
0.00
-0.01
3 ps
50
2500
7000
Wavelength / nm
450
600
900
1050
1200
1350
1214 nm
548
Time / ps
1000
100
10
Δ OD / a.u.
3x10^{-2}
1x10^{-2}
-8x10^{-3}
0.03
0.02
0.01
0.00
Δ OD / a.u.

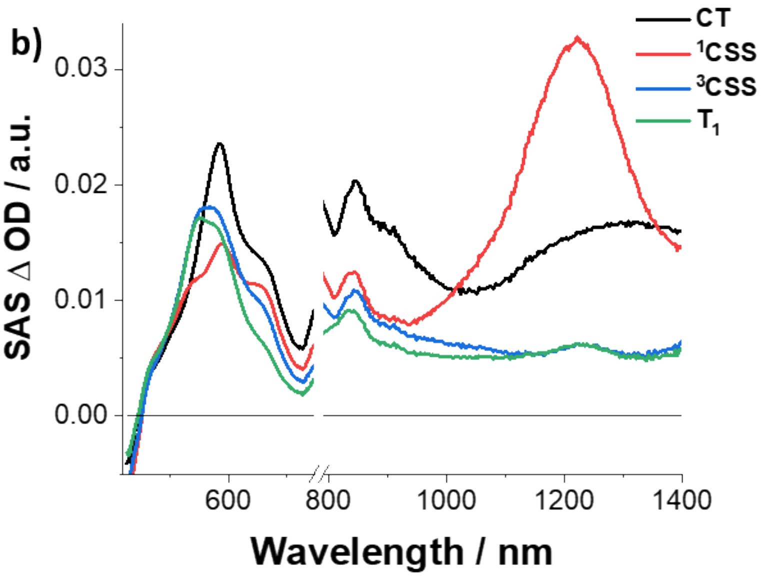
b)
CT
^{1}CSS
^{3}CSS
T$_1$
SAS Δ OD / a.u.
0.03
0.02
0.01
0.00
600
800
1000
1200
1400
Wavelength / nm

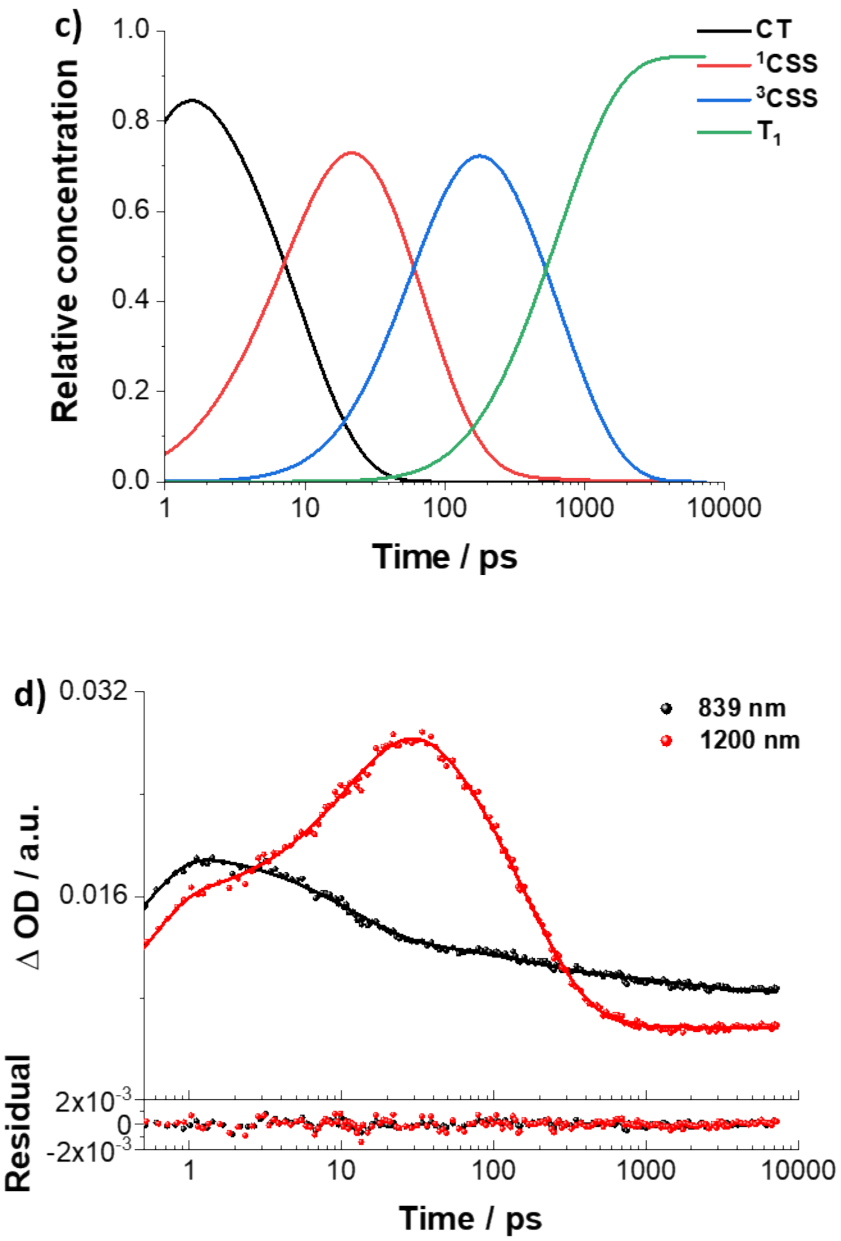

Figure S22. a) Differential absorption spectra (visible and near-infrared) obtained upon femtosecond flash photolysis (387 nm) of **4** in argon-saturated PhCN with several time delays between 0 and 7500 ps at room temperature. Lower left: Time absorption profiles of the spectra at 548 and 1214 nm. Upper Right: Differential absorption spectra with the depicted time delays. b) Deconvoluted species associated spectra (SAS) of CT (black), ^{1}CSS (red), ^{3}CSS (blue), and T_1 (green) in PhCN as obtained by global target analysis of time-resolved spectra on the sub-ps to ns timescale. c) Evolution of the population of the involved states in **4** in PhCN. d) Time absorption profiles at 839 and 1200 nm as well as the corresponding fits and residuals.

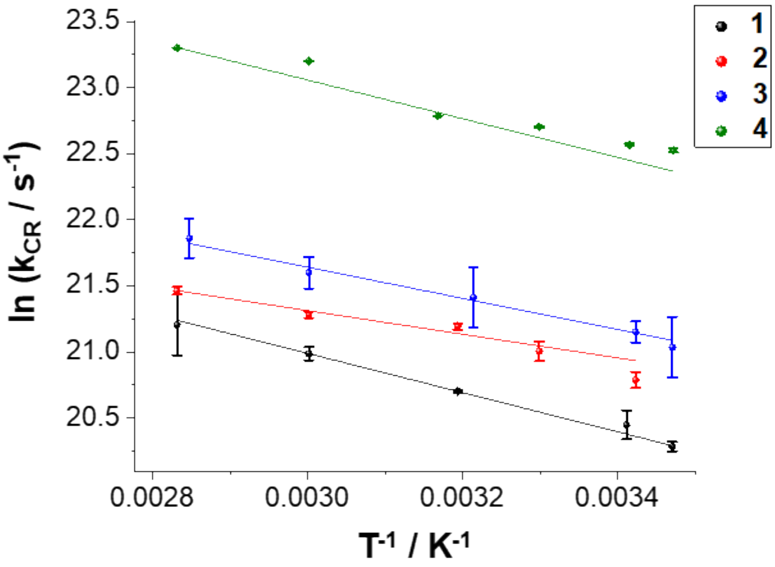

Figure S23. Temperature dependence of the charge recombination for **1**-**4** in the 288 to 353 K temperature regime based on the temperature-dependent femtosecond transient absorption experiments in benzonitrile.

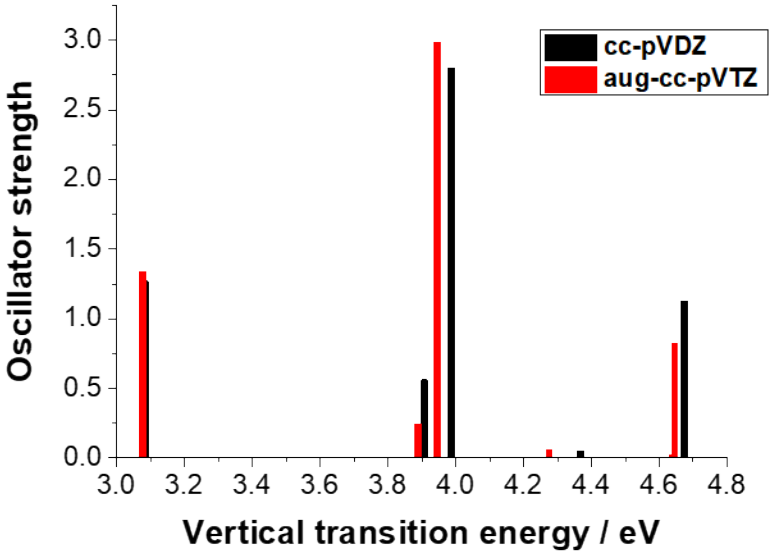

Figure S24. Vertical excitation energies for **4**, calculated with CAM-B3LYP and cc-pVDZ basis set (black) and augmented triple ζ auf-cc-pVTZ basis set (red).

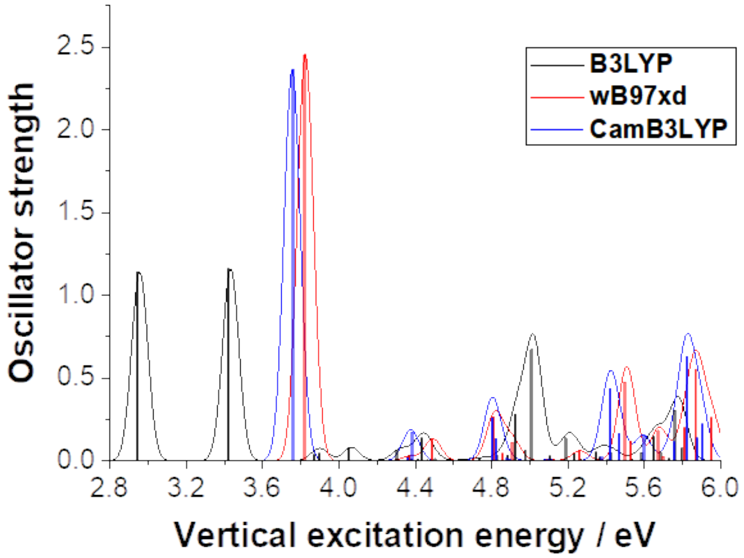

Figure S25. Vertical excitation energies of **1**, calculated with B3LYP (black), wB97xd (red) and CAM-B3LYP (blue). For all calculations the cc-pVDZ basis set was used.

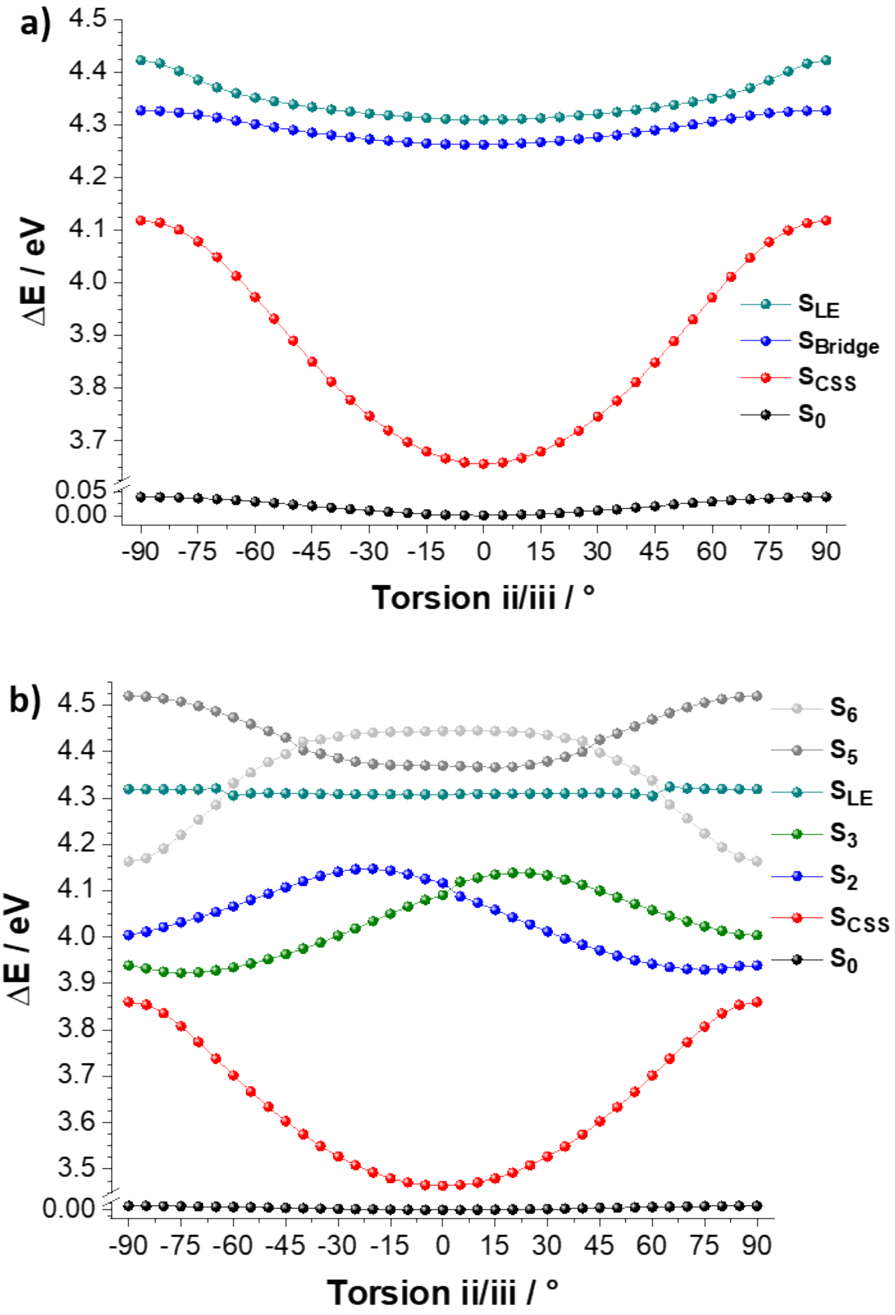

Figure S26. Torsion angle dependence of excited states energies of a) **1** and b) **2**.

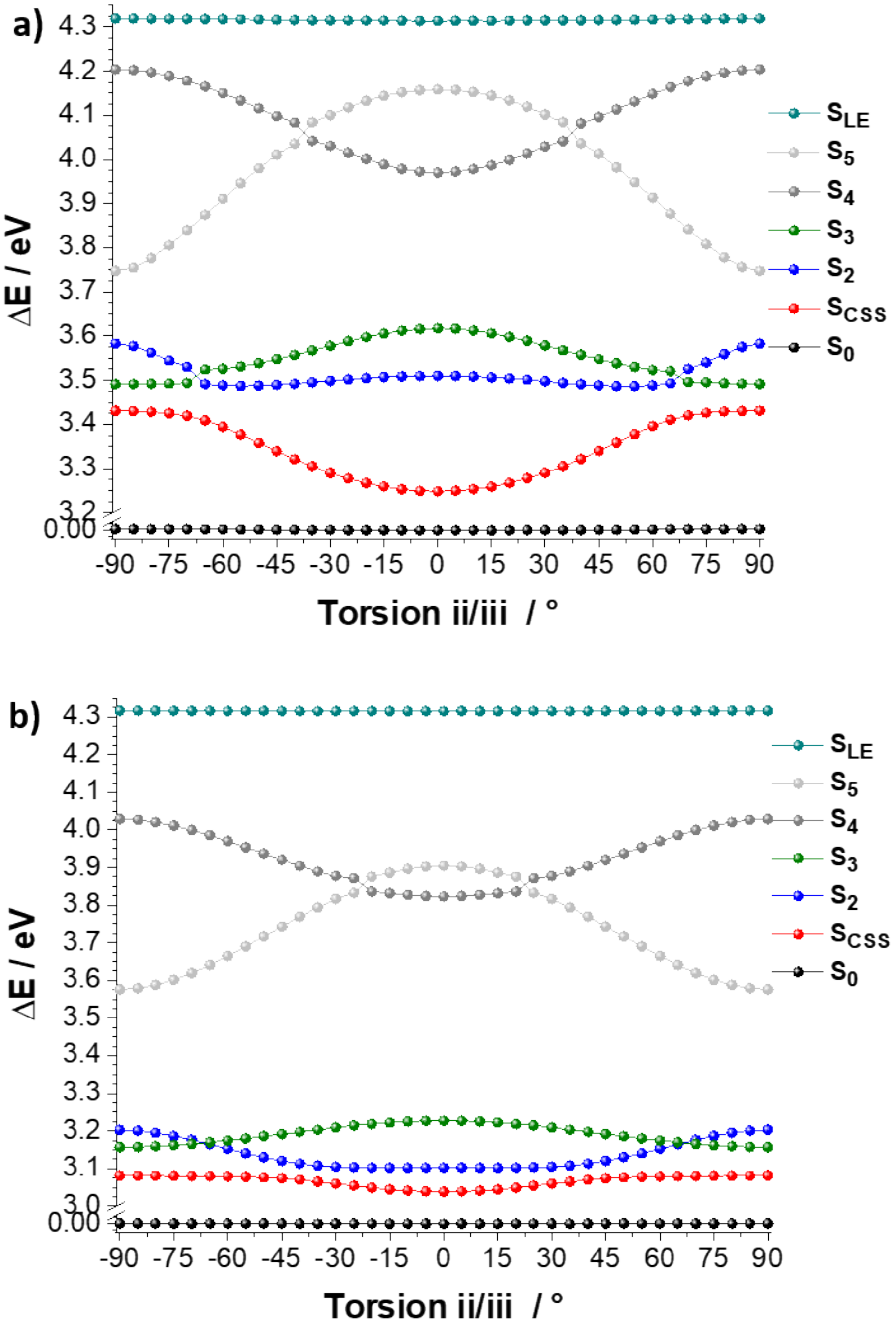

Figure S27. Torsion angle dependence of excited states energies of a) **3** and b) **4**.

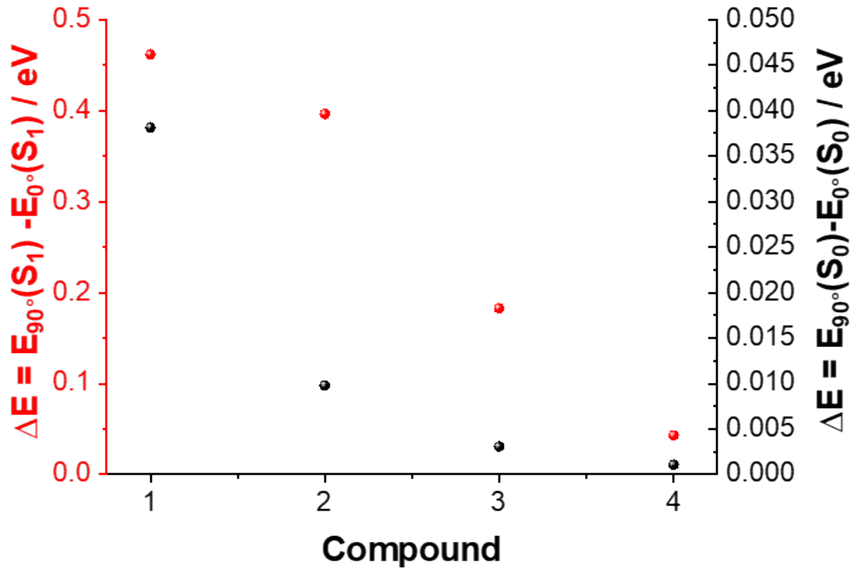

Figure S28. CAM-B3LYP/cc-pVDZ calculated energy difference between planar and perpendicular conformations regarding torsion angle *ii/iii* of the first excited singlet state (red, left scale) and the ground state singlet (black, right scale).

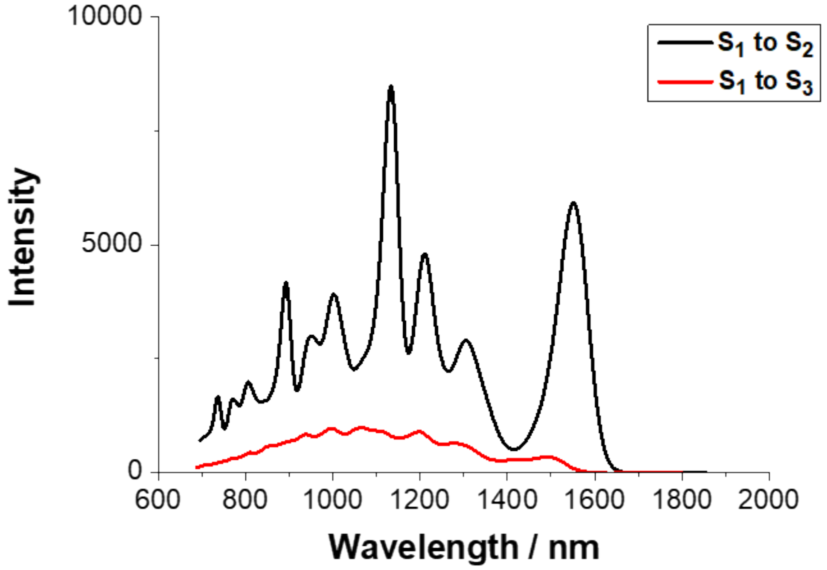

Figure S29. Predicted absorbance of the relaxed first excited singlet S_1 of **1** towards S_2 and S_3.

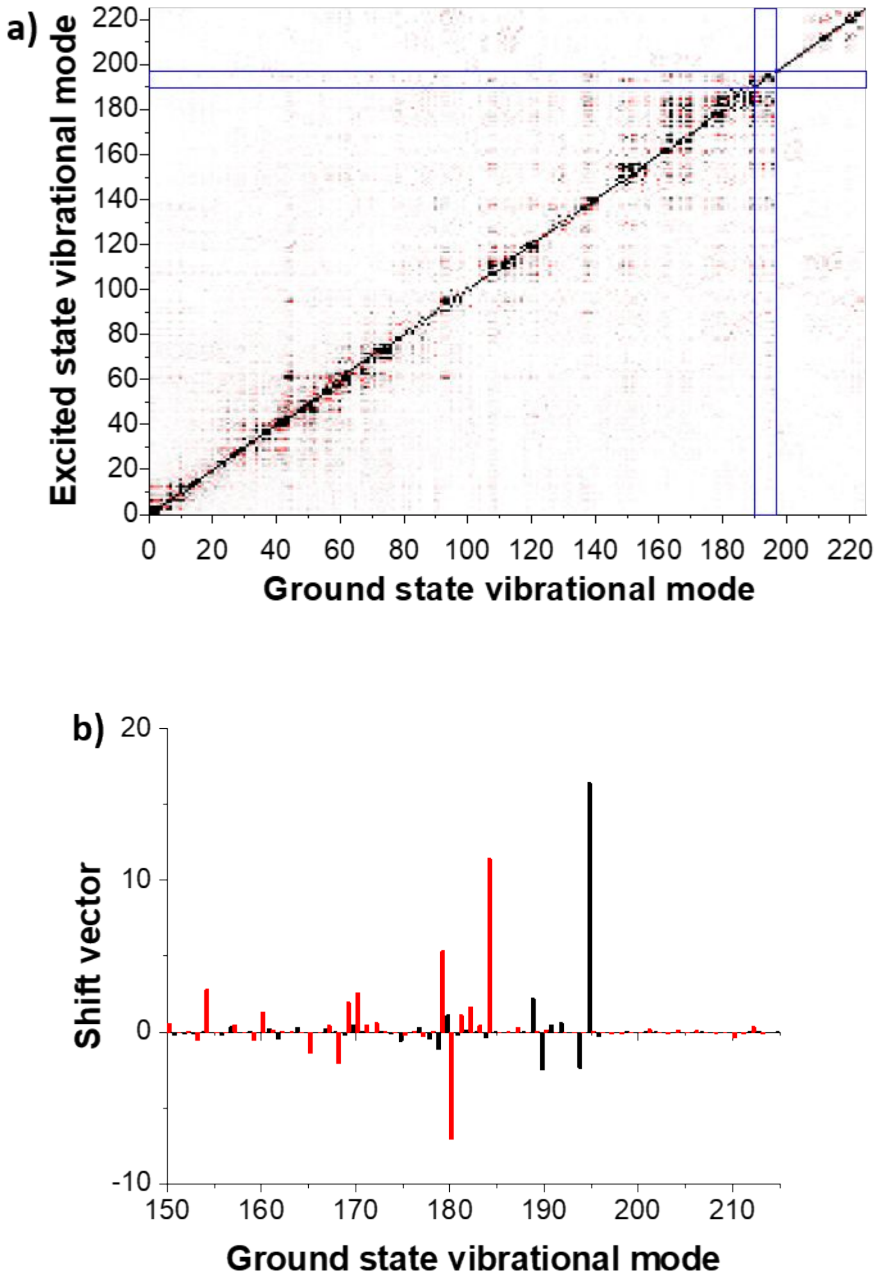
a)
Excited state vibrational mode
0
20
40
60
80
100
120
140
160
180
200
220
0
20
40
60
80
100
120
140
160
180
200
220
Ground state vibrational mode
b)
Shift vector
20
10
0
-10
150
160
170
180
190
200
210
Ground state vibrational mode

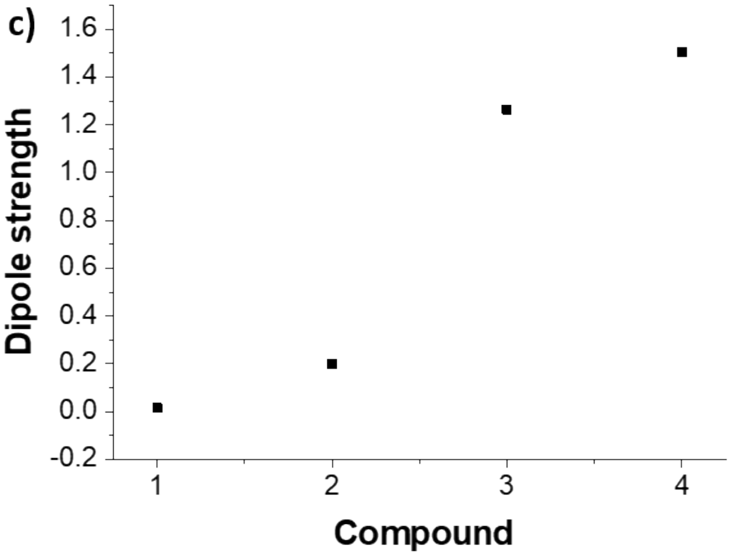

Figure S30. a) Duschinsky matrix for ground state to first excited state transition of **4**. B) Shift vector for ground state to first excited state transition of **4**. c) Dipole strength for ground state to first excited state transition. Values are based on the transition from the vibrational fundamental state of S_0 to the respective C-C and C≡C stretch vibrational mode of S_1 (^{1}CSS).

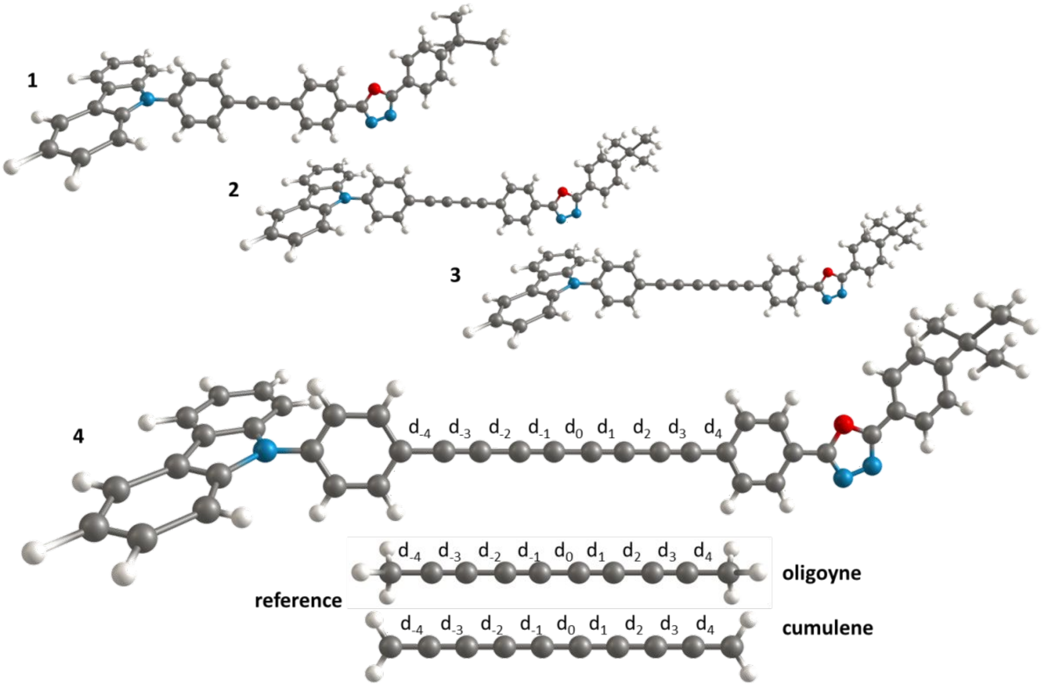
1
2
3
4
d_{-4} d_{-3} d_{-2} d_{-1} d_0 d_1 d_2 d_3 d_4
reference
oligoyne
cumulene

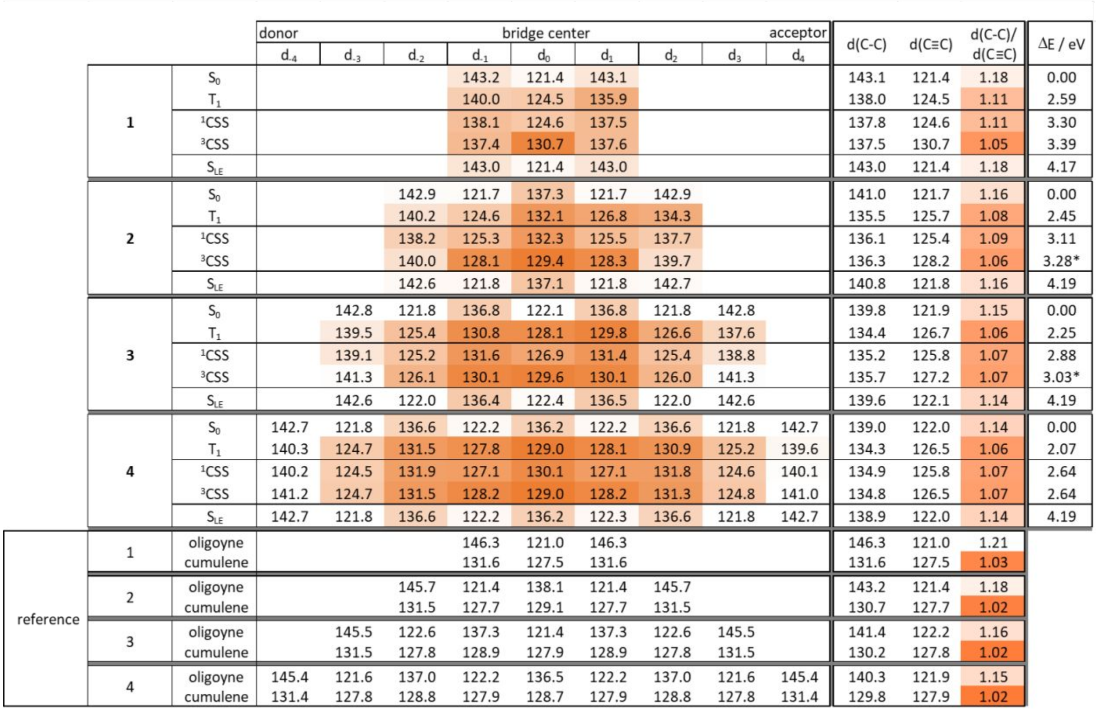

			donor				bridge center				acceptor	d(C-C)	d(C≡C)	d(C-C)/ d(C≡C)	ΔE / eV
			d_{-4}	d_{-3}	d_{-2}	d_{-1}	d_0	d_1	d_2	d_3	d_4				
	1	S_0				143.2	121.4	143.1				143.1	121.4	1.18	0.00
		T_1				140.0	124.5	135.9				138.0	124.5	1.11	2.59
		^{1}CSS				138.1	124.6	137.5				137.8	124.6	1.11	3.30
		^{3}CSS				137.4	130.7	137.6				137.5	130.7	1.05	3.39
		S_{LE}				143.0	121.4	143.0				143.0	121.4	1.18	4.17
	2	S_0			142.9	121.7	137.3	121.7	142.9			141.0	121.7	1.16	0.00
		T_1			140.2	124.6	132.1	126.8	134.3			135.5	125.7	1.08	2.45
		^{1}CSS			138.2	125.3	132.3	125.5	137.7			136.1	125.4	1.09	3.11
		^{3}CSS			140.0	128.1	129.4	128.3	139.7			136.3	128.2	1.06	3.28*
		S_{LE}			142.6	121.8	137.1	121.8	142.7			140.8	121.8	1.16	4.19
	3	S_0		142.8	121.8	136.8	122.1	136.8	121.8	142.8		139.8	121.9	1.15	0.00
		T_1		139.5	125.4	130.8	128.1	129.8	126.6	137.6		134.4	126.7	1.06	2.25
		^{1}CSS		139.1	125.2	131.6	126.9	131.4	125.4	138.8		135.2	125.8	1.07	2.88
		^{3}CSS		141.3	126.1	130.1	129.6	130.1	126.0	141.3		135.7	127.2	1.07	3.03*
		S_{LE}		142.6	122.0	136.4	122.4	136.5	122.0	142.6		139.6	122.1	1.14	4.19
	4	S_0	142.7	121.8	136.6	122.2	136.2	122.2	136.6	121.8	142.7	139.0	122.0	1.14	0.00
		T_1	140.3	124.7	131.5	127.8	129.0	128.1	130.9	125.2	139.6	134.3	126.5	1.06	2.07
		^{1}CSS	140.2	124.5	131.9	127.1	130.1	127.1	131.8	124.6	140.1	134.9	125.8	1.07	2.64
		^{3}CSS	141.2	124.7	131.5	128.2	129.0	128.2	131.3	124.8	141.0	134.8	126.5	1.07	2.64
		S_{LE}	142.7	121.8	136.6	122.2	136.2	122.3	136.6	121.8	142.7	138.9	122.0	1.14	4.19
reference	1	oligoyne				146.3	121.0	146.3				146.3	121.0	1.21	
		cumulene				131.6	127.5	131.6				131.6	127.5	1.03	
	2	oligoyne			145.7	121.4	138.1	121.4	145.7			143.2	121.4	1.18	
		cumulene			131.5	127.7	129.1	127.7	131.5			130.7	127.7	1.02	
	3	oligoyne		145.5	122.6	137.3	121.4	137.3	122.6	145.5		141.4	122.2	1.16	
		cumulene		131.5	127.8	128.9	127.9	128.9	127.8	131.5		130.2	127.8	1.02	
	4	oligoyne	145.4	121.6	137.0	122.2	136.5	122.2	137.0	121.6	145.4	140.3	121.9	1.15	
		cumulene	131.4	127.8	128.8	127.9	128.7	127.9	128.8	127.8	131.4	129.8	127.9	1.02	

Figure S31. *Top:* CAM-B3LYP/cc-pVDZ optimized ground state structures for **1-4** and reference **4** in oligoyne and cumulenic form. Label of the C-C and C≡C bonds start from d_0 (central bridge bond) towards d_{-4} (carbazole) and d_{+4} (oxadiazole), respectively. *Table:* Individual bond lengths in pm, averaged single and triple bond lengths and their ratio for the ground state singlet (S_0), lowest triplet excited state (T_1), the singlet charge separated state (^{1}CSS), the triplet charge separated state (^{3}CSS), and the local singlet excited state (S_{LE}) for **1-4**. *Please note: Complete optimization convergence of the charge separated triplet state (T_{CSS}) was hindered by multiple potential surface crossing for **2** and **3**.

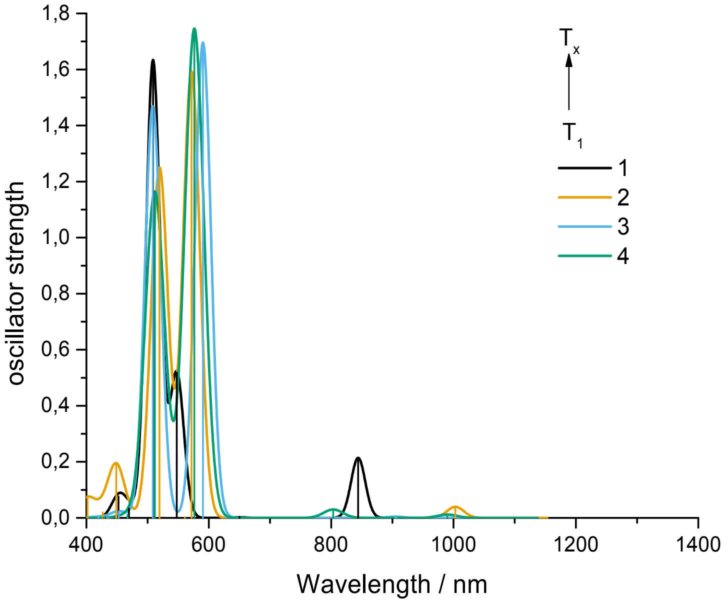

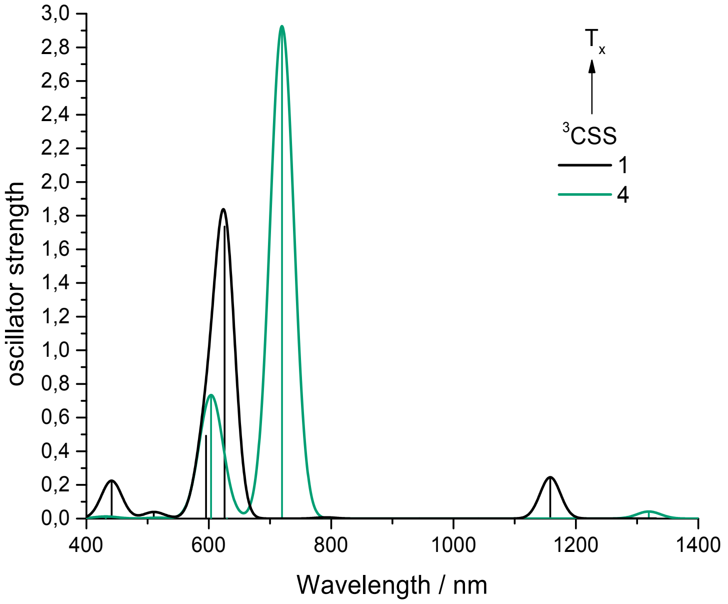

Figure S32. a) CAM-B3LYP/cc-pVDZ predicted vertical energies based on the optimized local triplet excited state (T_1) for **1-4**. b) CAM-B3LYP/cc-pVDZ predicted vertical energies based on the optimized triplet charge separated state (^{3}CSS) for compounds **1** and **4**.

Table S3. Rate constant (k_{ET}), reaction free energy ($-\Delta G_{\mathrm{ET}}^0$), activation free energy ($\Delta G_{\mathrm{ET}}^{\#}$), reorganization energy (λ), and electronic coupling (V_{DA}) associated with back electron transfer from ^{1}CSS to ground state in **1-4** in benzonitrile.

Compound	k_{ET} / s^{-1}	$-\Delta G_{\mathrm{ET}}^0$/ eV	$\Delta G_{\mathrm{ET}}^{\#}$/ eV	λ/ eV	V_{DA} / cm^{-1}
1	9.53×10^8	2.74	0.127	1.78	27
2	1.07×10^9	2.69	0.077	1.92	11
3	1.64×10^9	2.49	0.102	3.72	26
4	6.36×10^9	2.35	0.126	3.72	80

The quadratic relationship between $\Delta G_{ET}^{\#}$ and λ gives two mathematical solutions. Considering that λ is expected to increase with increasing distance, only one solution is physically meaningful.

References for SI

(1) Wang, C.; Batsanov, A. S.; West, K.; Bryce, M. R. *Org. Lett.* **2008**, *10*, 3069-3072.

(2) Wang, C.; Palsson, L.-O.; Batsanov, A. S.; Bryce, M. R. *J. Am. Chem. Soc.* **2006**, *128*, 3789-3799.

(3) Wu, X.; Wang, L.; Hua, Y.; Wang, C.; Batsanov, A. S.; Bryce, M. R. *Tetrahedron* **2014**, *70*, 2015-2019.

(4) Palsson, L. O.; Wang, C.; Batsanov, A. S.; King, S. M.; Beeby, A.; Monkman, A. P.; Bryce, M. R. *Chem. Eur. J.* **2010**, *16*, 1470-1479.

(5) Sheldrick, G. M. *Acta Crystallogr.* **2008**, *A64*, 112-122.

(6) Sheldrick, G. M. *Acta Crystallogr.* **2015**, *C71*, 3-8.

(7) Dolomanov, O. V.; Bourhis, L. J.; Gildea, R. J.; Howard J. A. K. and Puschmann, H. *J. Appl. Crystallogr.,* **2009**, *42*, 339-341

(8) van der Sluis, P.; Spek, A. L. *Acta Crystallogr.* **1990**, *A46*, 194-201.

(9) Rees, B.; Jenner L.; Yusupov, M. *Acta Crystallogr.* **2005**, *D61*, 1299-1301.

(10) Fielden, E. M., Chemical Dosimetry of Pulsed Electron and X-Ray Sources in the 1 - 20 MeV Range. In *The Study of Fast Processes and Transient Species by Electron Pulse Radiolysis: Proceedings of the NATO Advanced Study Institute held at Capri, Italy, 7 – 18 September, 1981*, Baxendale, J. H.; Busi, F., Eds. Springer Netherlands: Dordrecht, 1982; pp 49-62.

(11) Nakayama, T.; Ushida, K.; Hamanoue, K.; Washio, M.; Tagawa, S.; Tabata, Y. *J. Chem. Soc., Faraday Trans.* **1990**, *86*, 95-103.

(12) Guldi, D. M.; Hungerbuehler, H.; Asmus, K.-D. *J. Phys. Chem* **1995**, *99*, 9380-9385.

(13) Porter, G.; Dogra, S. K.; Loutfy, R. O.; Sugamori, S. E.; Yip, R. W. *J. Chem. Soc., Faraday Trans.1* **1973**, *69*, 1462-1474.

(14) Wardman, P. *J. Phys. Chem. Ref. Data* **1989**, *18*, 1637-1755.